Mon. Not. R. Astron. Soc. **395,** 28–63 (2009) doi:10.1111/j.1365-2966.2009.14519.x

Stellar population and kinematic profiles in spiral bulges and discs: population synthesis of integrated spectra

Lauren A. MacArthur,[1⋆] J. Jesús González[2⋆] and Stéphane Courteau[3⋆]

[1]*Department of Astrophysics, California Institute of Technology, MS 105-24, Pasadena, CA 91125, USA*
[2]*Instituto de Astronomia, Universidad Nacional Autónoma de México, Apdo Postal 70-264, Cd. Universitaria 04510, Mexico*
[3]*Department of Physics, Engineering Physics & Astronomy, Queen's University, Kingston, ON, Canada K7L 3N6*

Accepted 2009 January 16. Received 2009 January 7; in original form 2008 October 29

ABSTRACT

We present a detailed study of the stellar populations (SPs) and kinematics of the bulge and inner disc regions of eight nearby spiral galaxies (Sa–Sd) based on deep Gemini/GMOS data. The long-slit spectra extend to 1–2 disc scalelengths with S/N/Å $\geq$ 50. Several different model fitting techniques involving absorption-line indices and full spectrum fitting are explored, and found to weigh age, metallicity and abundance ratios differently. We find that the SPs of spiral galaxies are not well matched by single episodes of star formation; more representative SPs must involve average SP values integrated over the star formation history (SFH) of the galaxy. Our 'full population synthesis' method is an optimized linear combination of model templates to the full spectrum with masking of regions poorly represented by the models. Realistic determinations of the SP parameters and kinematics (rotation and velocity dispersion) also rely on careful attention to data/model matching (resolution and flux calibration). The population fits reveal a wide range of age and metallicity gradients (from negative to positive) in the bulge, allowing for diverse formation mechanisms. The observed positive age gradients within the effective radius of some late-type bulges helps reconcile the long-standing conundrum of the coexistence of secular-like kinematics, light profile shape and stellar bar with the 'classical'-like old and α-enhanced SPs in the Milky Way bulge. The discs, on the other hand, almost always show mildly decreasing to flat profiles in both age and metallicity, consistent with inside-out formation. Our spiral bulges follow the same correlations of increasing light-weighted age and metallicity with central velocity dispersion as those of elliptical galaxies and early-type bulges found in other studies, but when SFHs more complex and realistic than a single burst are invoked, the trend with age is shallower and the scatter much reduced. In a mass-weighted context, however, all bulges are predominantly composed of old and metal-rich SPs. While secular contributions to the evolution of many of our bulges are clearly evident, with young (0.001–1 Gyr) SPs contributing as much as 90 per cent of the optical (*V*-band) light, the bulge mass fraction from young stars is small ($\lesssim$25 per cent). The implies a bulge formation dominated by early processes that are common to all spheroids, whether they currently reside in discs or not. While monolithic collapse cannot be ruled out in some cases, merging must be invoked to explain the SP gradients in most bulges. Further bulge growth via secular processes or 'rejuvenated' star formation generally contributes minimally to the stellar mass budget, with the relative secular weight increasing with decreasing central velocity dispersion.

Key words: galaxies: bulges – galaxies: evolution – galaxies: formation – galaxies: spiral – galaxies: stellar content.

1 INTRODUCTION

In the context of the currently favoured cosmological Λ cold dark matter (ΛCDM) model of our Universe, the formation and evolution

⋆E-mail: lam@astro.caltech.edu (LAM); jesus@astroscu.unam.mx (JJG); courteau@astro.queensu.ca (SC)

of galaxies remains a major unsolved problem. In this model, structures form in a bottom-up, hierarchical, manner by which smaller fragments merge together to form more massive systems. While this model has been very successful at reproducing observations on large scales, a number of issues remain to be resolved at the galaxy-scale regime (Moore et al. 1999; Navarro & Steinmetz 2000; Primack 2007, and references therein). In particular, the formation of disc galaxies is not well represented in current implementations of simulations based on ΛCDM (e.g. Bell et al. 2003; Dutton et al. 2007; Kaufmann et al. 2007). The discrepancies do not necessarily indicate a failure in the ΛCDM model, but rather point to physical regimes and processes that are either not well understood or difficult to implement in large simulations. Given the theoretical difficulties and limitations faced by current models, a true understanding of disc galaxies must include information from an observational perspective.

All aspects of baryonic physics, from hydrodynamical processes involving gas, through star formation and feedback from supernovae and active galactic nuclei (AGN), can play a role in the formation and regulation processes that shape galaxies, particularly where dynamically violent processes such as major mergers and rapid collapse are not dominant. For spiral galaxies, the very presence of a disc component implies that no such major event has occurred since the formation of the dynamically fragile disc. Additionally, most disc galaxies harbour central bulge components whose prominence in terms of total mass or light-weight spans a wide range from truly bulgeless systems to the bulge-dominated early-type S0/Sa galaxies. A question that naturally arises is if the final step to the discless, i.e. pure elliptical, galaxies is a natural extension of bulge-to-total ratios in systems along the Hubble sequence. Such an extension would imply that the dominant bulges of early-type spirals have followed a similar evolutionary path to those of pure elliptical galaxies. However, coming from the opposite end, a connection between the tiny bulges of late-type spirals, through early-types, to pure ellipticals may not seem as obvious, and allowance must still be made for the pure disc galaxies in any scenario. The emerging observational picture of bulge formation currently implies similar evolutionary paths for early-type spirals and pure ellipticals, while the later type bulges exhibit much more diversity in their observed properties, consistent with having formed through a secular redistribution of material from the disc (e.g. Kormendy & Kennicutt 2004). The nomenclature predominant in the literature to distinguish between formation scenarios for bulges names those appearing very similar to pure elliptical systems (i.e. rapid and/or violent formation which includes both the monolithic collapse and major merging scenarios) as 'classical bulges' and those formed secularly from the disc as 'pseudo-bulges'. However, uncertainties in making a clear-cut distinction between these cases still remain, particularly in regards to the stellar populations (SPs) of spiral bulges.

A very useful probe in discerning between formation scenarios is a detailed breakdown of the age, metallicity (Z) and kinematic properties of the SPs comprising bulges of all types. Information about both light- and mass-weighted quantities is needed to form a comprehensive picture of the star formation history (SFH) of a given system. However, beyond our Local Group, we are limited to observations of the integrated light along a given line of sight. Of relevance is whether the integrated light at any location in a galaxy can be deconvolved into the relative fractions of stars of a given population that contribute to the total light. This question is especially acute for spiral galaxies that are known to harbour a mixture of young and old stars and can suffer from the extinction effects of dust.

Observations of colour gradients and absorption line indices in galaxies can both be interpreted as a single-burst, single-Z stellar population (SSP), from which light-weighted SSP-equivalent ages and metallicities can be drawn with the help of spectral synthesis models (e.g. Vazdekis 1999; Bruzual & Charlot 2003, hereafter BC03; Thomas, Maraston & Bender 2003; Le Borgne et al. 2004; Maraston 2005; Schiavon 2007). Elliptical galaxies (e.g. Trager, Faber & Dressler 2008) and globular clusters (e.g. Cohen, Blakeslee & Ryzhov 1998; Puzia et al. 2005; Hernandez & Valls-Gabaud 2008), are often assumed to result from the evolution of a single burst of star formation and thus can be represented by an SSP of a given age and Z. This assumption, however, breaks down for spiral galaxies that are believed to have been converting gas into stars at a relatively constant rate over most of their lifetime (e.g. Kennicutt 1983; James, Prescott & Baldry 2008). Since the presence of a young SP will dominate the optical light even when its contribution to the mass is minimal, the light-weighted ages will not be representative of the entire population. Even pure ellipticals show signs of 'frostings' of young SPs and may not be well represented by a single SSP (Serra & Trager 2007).

Greater potential for disentangling the SFH of spiral galaxies exists if they can be assumed to have proceeded smoothly with time. This approach was followed by MacArthur et al. (2004) using broad-band optical colours for 172 low-inclination disc galaxies. To the extent that the nearby spiral galaxies in this sample share a similar underlying SFH and that no burst involving more than $\sim$10 per cent of the galaxy mass has occurred within the past 1–2 Gyr, the method provides reliable relative results. Among others, it was found that the SFH of spiral galaxies depends strongly on the galaxy potential and halo spin parameter.

Conclusions based on colour gradients are, however, plagued by a degeneracy between the effects of age, Z and dust, all leading to redder colours. Spectroscopic techniques, such as those based on absorption-line equivalent widths (EWs) that are largely impervious to dust effects (MacArthur 2005), or fitting of the full spectral energy distribution (SED) which can incorporate a dust component, offer a more detailed and discriminating view, especially in light of the latest implementations of SP synthesis models (e.g. Vazdekis 1999; BC03; Le Borgne et al. 2004).

Early-type spirals with their large bulge-to-disc ratio offer a significant observational advantage over late-types since their bulges, which rise significantly above and below the disc, can be studied spectroscopically in the edge-on perspective free from disc contamination and extinction from dust. Late-type bulges, on the other hand, are small and often no thicker than the galaxy disc itself, thus requiring a face-on projection for their study. While dust and contamination from the inner disc will still thwart any pristine observation of the bulge, the face-on orientation minimizes line-of-sight integrations and keeps the light distribution of the bulge and disc free of inclination effects.

Spectroscopic studies of bulges spanning the full range of Hubble types are few, and the results are often conflicting. The absorption-line studies of the central regions of Sa–Sc spirals of Trager, Dalcanton & Weiner (1999) and Proctor & Sansom (2002, hereafter PS02) both find that late-type bulges cannot be reproduced using primordial collapse models and invoke extended gas infall on to the central bulge to explain the observations. In a similar study, Goudfrooij, Gorgas & Jablonka (1999) conclude the opposite, their findings being more compatible with predictions of the 'dissipative collapse' model than with those of the 'secular evolution' model for bulge formation. Their sample is, however, dominated by early-type spirals and these conclusions may not apply to the full range of

spiral types. Finally, the analysis of Moorthy & Holtzman (2006) of line strengths in the bulges and inner discs of 38 spirals also *favours* a scenario whereby merging is the dominant mechanism for bulge formation.

Thomas & Davies (2006) reanalysed the PS02 data and found no difference between the SPs of spiral bulges and Es at a given central velocity dispersion, σ_0, concluding that processes involving disc material cannot be responsible for the recent star formation implied by the young ages. In an analysis of stellar absorption line gradients in the bulges of 32 nearby edge-on spirals (S0–Sc), Jablonka, Gorgas & Goudfrooij (2007) also find that, when compared at a given velocity dispersion, galaxy bulges resemble elliptical galaxies. Recently, MacArthur et al. (2008) have extended these results to bulges at intermediate redshifts ($0.1 < z < 1$) finding that the mass assembly history of bulges, inferred via the Fundamental Plane, is indistinguishable from that of pure spheroidal galaxies (E/S0s) at a given mass.

A significant outlier from this trend, however, is the bulge of our own Milky Way (MW). Detailed photometric (Zoccali et al. 2003) and spectroscopic (Rich & Origlia 2005; Zoccali et al. 2006) studies of abundance ratios of individual MW bulge stars reveal old and α-enhanced SPs that must have formed long ago and on short time-scales, and no evidence is found for the presence of a younger SP. This observation is difficult to reconcile with the MWs small σ_0 and the presence of a stellar bar (e.g. López-Corredoira et al. 2007). As Thomas & Davies point out, the MW studies sample a larger physical radius than those of external galaxies so this conundrum could be resolved if there is a positive age gradient in the bulge.

Adding further complexity to the picture, in a study of absorption-line maps of 24 early-type spirals, Peletier et al. (2007) find that while inclined samples, which sample the disc-free outer bulge regions, reveal uniformly old SPs, randomly oriented samples, spanning the same range in Hubble type, show a wide range in SP parameters. This discrepancy, along with their observation of central dips in the velocity dispersion profiles of half of their bulges, indicative of the presence of a colder central component, can be reconciled in a picture whereby the centres of most early-type spirals contain multiple kinematic components: an old and slowly rotating elliptical-like component, and one or more disc-like, rotationally supported, components which are typically young, but can be old. The sum of all central components make up the photometrically defined bulge, and the different components contribute differently to the integrated light depending on the viewing angle. Their conclusion of a rejuvenation of the central region through dynamical disc-like processes, however, is difficult to understand in the context of the above results in that the 'rejuvenated' low-σ ellipticals do not have disc components.

At the heart of these conflicts is the fact that extant studies of local bulges are limited in one way or another (sample size, range in Hubble type, data of insufficient depth and/or spatial resolution for studies of gradients and assessment of disc contamination, etc.). Our aim is to remedy this situation with a systematic and homogeneous study of the SPs and kinematics of bulges for the full range of Hubble types. A first, and important, step is to establish a reliable procedure for extracting a proper representation of the SP content that does not suffer from the degeneracies and limitations discussed above. In this paper, we present a pilot sample of long-slit optical spectroscopy of eight nearby, low-inclination, spiral galaxies observed with Gemini/GMOS with which we develop such a technique and attempt to address the formation of spiral bulges through a study of their radial profiles in SPs and kinematics.

The organization of the paper is as follows. In Section 2 we detail the sample selection, observational strategy and reduction procedures. Section 3 outlines our technique for extracting SP parameters from integrated spectra including details of the fitting algorithm, providing specifics about the weighting of individual pixels and our so-called 'σ-clipping' procedure for masking deviant pixels, as well as a description of the model SP templates used in the fits. Our results are presented in Section 4 which includes the derived SP parameters and their radial profiles, kinematic profiles (rotation velocity and velocity dispersion), an investigation of correlations of central parameters, and a comparison with previous studies. We discuss in Section 5 results for each individual galaxy in the context of bulge formation scenarios, and Section 6 summarizes the salient points from the entire analysis. Finally, we provide the appendixes. Appendix A presents the observed radially resolved spectra for our galaxies. Appendix B discusses derivations of SP parameters for our spiral galaxies based on the Lick index system and of full spectrum fitting of single SSPs. All techniques are compared and contrasted in Appendix C.

2 DATA

The long-slit spectroscopic data for this paper were collected using the Gemini Multi-Object Spectrograph (GMOS; Hook et al. 2004) on the 8-m Gemini-North telescope at Mauna Kea in Hawaii. The GMOS detector consists of three 2048 × 4608 CCDs with 13.5-μm pixels providing a spatial resolution of 0.072 arcsec pix^{-1} and a dispersion of 0.45 Å pix^{-1} with the B600_G5303 grating. The internal stability of the slit mask requires two equally spaced bridges between the slit edges which lie along the spatial direction. The spacings between the three CCD detectors manifest as small (∼17 Å) gaps in wavelength.

The high sensitivity of the B600_G5303 grating in the blue matches well our simultaneous spectral coverage of ∼4050–6750 Å. This range includes most of the major atomic and molecular features to disentangle age and metallicity effects in integrated galaxy spectra (Worthey 1994). The slit field of view (FOV) was 5 arcmin (length) × 2 arcsec (width) for all of our observations. The choice of slit width was prescribed by the need to maximize signal-to-noise ratio (S/N) in the outer disc while maintaining adequate spectral resolution throughout. The 2-arcsec slit and B600 grating give a top-hat 10.81 Å full width at half-maximum (FWHM) resolution and a Gaussian instrumental resolution of 0.8 ± 0.02 Å (as measured from the width of the narrowest sky emission lines).

2.1 Galaxy sample

Ideally, we desire a large and homogeneous sample of nearby spiral galaxies spanning the full Hubble sequence to study spectroscopically the SPs of spiral bulges and discs. The sample should also include barred and non-barred spirals in order to test for the expected mixing effects by a bar. The size of the current sample was a compromise between a reasonable telescope time request for a pilot study and the need to measure systematic variations within that sample. We have thus narrowed in on the following criteria:

(i) Hubble type Sa–Sd (with emphasis on later types);
(ii) mix of barred/unbarred systems and SB profile types;
(iii) face-on (inclination $\lesssim 35^\circ$);
(iv) Galactic extinction $A_B = 4E(B-V) \leq 0.5$ mag (Schlegel, Finkbeiner & Davis 1998);

Table 1. Galaxy sample: catalogue information.

Names		Hubble	Diam	RA	Dec.	$V_{\rm helio}$	M_B	A_B
NGC/IC	UGC	type	a (arcmin) × b (arcmin)	(J2000)		(km s^{-1})	(mag)	(mag)
(1)	(2)	(3)	(4) (5)	(6)	(7)	(8)	(9)	(10)
N0173	U369	SA(rs)c	3.2 × 2.6	$00^{\rm h}37^{\rm m}12\overset{\rm s}{.}47$	$+01°56'32\overset{''}{.}1$	4366	13.70	0.110
N0628	U1149	SA(s)c	10.5 × 9.5	$01^{\rm h}36^{\rm m}41\overset{\rm s}{.}77$	$+15°47'00\overset{''}{.}5$	657	9.95	0.301
N1015	**U2124**	SB(r)a	2.6 × 2.6	$02^{\rm h}38^{\rm m}11\overset{\rm s}{.}56$	$-01°19'07\overset{''}{.}3$	2629	12.98	0.139
N7490	U12379	Sbc	2.8 × 2.6	$23^{\rm h}07^{\rm m}25\overset{\rm s}{.}17$	$+32°22'30\overset{''}{.}2$	6213	13.05	0.362
N7495	U12391	SAB(s)c	1.8 × 1.7	$23^{\rm h}08^{\rm m}57\overset{\rm s}{.}18$	$+12°02'52\overset{''}{.}9$	4887	13.73	0.371
N7610	U12511	Scd	2.5 × 1.9	$23^{\rm h}19^{\rm m}41\overset{\rm s}{.}37$	$+10°11'06\overset{''}{.}0$	3554	13.44	0.171
N7741	U12754	SB(s)cd	4.4 × 3.0	$23^{\rm h}43^{\rm m}54\overset{\rm s}{.}37$	$+26°04'32\overset{''}{.}2$	751	11.84	0.323
I0239	U2080	SAB(rs)cd	4.6 × 4.2	$02^{\rm h}36^{\rm m}27\overset{\rm s}{.}88$	$+38°58'11\overset{''}{.}7$	903	11.80	0.307

Notes: Columns (1) and (2): NGC/IC and UGC Galaxy IDs. Names highlighted in bold are those used subsequently to refer to the particular galaxy. Column (3): Hubble type (from NED). Columns (4) and (5): major (a) and minor (b) axis diameters (in arcmin). Columns (6) and (7): galaxy RA and Dec. (J2000). Column (8): heliocentric radial velocity. Column (9): total B-band magnitude (Vega) from NED. Column (10): B-band Galactic extinction from Schlegel et al. (1998).

Table 2. Bulge and disc photometric scale parameters.

Name NGC (1)	$r_{\rm e}$ (arcsec) (2)	Sérsic n (3)	$r_{\rm d}$ (arcsec) (4)
N0173	3.8	1.5	21.9
N0628	10.5	1.1	68.2
U2124	5.7	1.5	12.2
N7490	4.5	1.6	21.4
N7495	3.6	2.3	17.2
N7610	1.7	0.8	17.6
N7741	6.7	1.0	42.3
I0239	8.2	0.9	43.8

Notes: Photometric bulge and disc scale parameters based on optical imaging (either R or I band, but V for N0173) from the Palomar 200-inch telescope. Errors on the disc scalelengths are $\lesssim$10 and 20 per cent for bulge parameters. See Mac03 for details of our B/D decomposition scheme. Column (1): galaxy ID. Columns (2)–(4): B/D decomposition values for bulge effective radius ($r_{\rm e}$), Sérsic n and disc scalelength ($r_{\rm d}$).

(v) blue major axis $\lesssim$2× slit length ($\lesssim$10.5 arcmin), but large enough to resolve bulge and inner disc ($\gtrsim$2 arcsec).

The galaxy sample and catalogue information from the NASA Extragalactic Database (NED)[1] are shown in Table 1. Optical imaging for all eight galaxies was collected using the Large Format Camera on the 200-inch Hale telescope at the Palomar Observatory in 2006 December. Observations were obtained in the BVRI Bessel filters for all galaxies except N0173, for which only B&V were obtained (due to bad weather). Surface brightness profiles were extracted from these images and bulge and disc photometric parameters were derived from bulge-to-disc (B/D) decompositions into an exponential disc plus a generalized power-law (Sérsic) profile for the bulge, as listed in Table 2. We refer the reader to MacArthur, Courteau & Holtzman (2003, hereafter Mac03) for details about profile extraction and B/D decompositions. Note that here we refer to the disc scalelength as $r_{\rm d}$ and the bulge effective (half-light) radius as $r_{\rm e}$ for a profile characterized by the Sérsic n shape parameter.

[1] http://nedwww.ipac.caltech.edu/.

As is typical for late-type bulges (e.g. de Jong 1996; Courteau, de Jong & Broeils 1996; Graham 2001; Mac03), most of our decompositions reveal bulge profile shapes close to exponential, which translates to a Sérsic index $n = 1$. Most notably, the bulge of N7495 was best fitted with $n = 2.3$. Bulges with $n \gtrsim 2$ are typically found in earlier type bulges thought to be more akin to elliptical galaxies (e.g. Fisher & Drory 2008). This suggests perhaps that the Hubble type of this galaxy is earlier than Sc. In fact, as noted in NED, the original UGC catalogue does refer to this as an 'early spiral' (Nilson 1973). On the other hand, our only Sa bulge, U2124, is best fitted with $n = 1.5$ which is low for an early-type bulge. However, the strong bar in this galaxy renders the decomposition less certain.

2.2 Standard star sample

We observed seven Lick/IDS standard stars (Worthey et al. 1994) with the same observational set-up as the main targets for flux calibration of the galaxy spectra. These included dwarfs and giants with a range of physical parameters relevant for star-forming galaxies (spectral type: A1–F5; effective temperature: $T_{\rm eff} \sim$ 4700–9000 K, surface gravity: log(g) = 2.4–4.3; and metallicity: [Fe/H] = −0.45 to 0.07). Flux calibration was achieved by comparison of our standard star observations with flux calibrated spectra of stars in common with the ELODIE archive (Moultaka et al. 2004; see http://atlas.obs-hp.fr/elodie).

2.3 Integration times and observing strategy

The on-target integrations were divided into separate exposures to filter out cosmic rays and confirm weak features. On-target integration times were 3 × 15 min for $M_B <$ 10.5, 3 × 18 min for 10.5 < M_B < 12 and 4 × 18 min for $M_B >$ 12, for total integrations of 45–72 min per galaxy. An estimate of the sky background was measured from the slit edges for galaxies with major axis diameters <4 arcmin. For galaxies wider than the slit, we divided our exposures into sky/galaxy/sky sequences with integration times for sky (off-target) pointings of ∼1/5 of the on-target integrations.[2] See Fig. 1 for the observational set-up for each galaxy. Sky positions, when necessary, are shown by the yellow

[2] In hindsight, sky integration times of 1/3–1/2 of the on-target times would have been preferred. The short sky exposures prevented a deeper exploration of the low-SB disc regions.

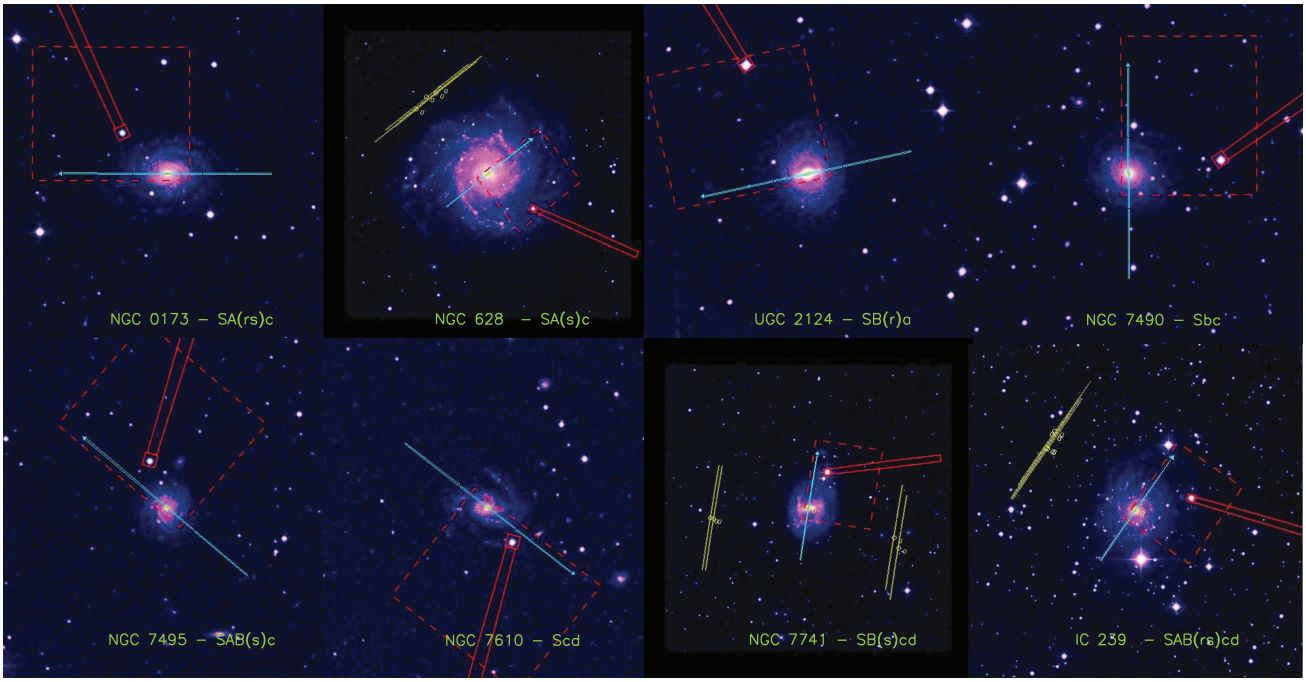

Figure 1. Observational set-up for the eight galaxies in our sample. The background images are from the Canadian Astronomy Data Centre's Digitized Sky Server (CADC; http://cadcwww.dao.nrc.ca/). The blue line represents the slit, the red (dashed) box and long arm represent the FOV of the GMOS wavefront sensor camera, with the box at the end of the arm centred on the guide star. The panels for large galaxies (NGC 628, 7741 and IC 239) also show, as yellow lines, the sky offset positions. The FOV for the CADC pictures differ in all the panels but the slit length is everywhere the same (5 arcmin).

slits. Sky exposures were binned to achieve the same S/N as the galaxy.

2.4 Data reduction

The relevant measurements for this paper do not require absolute spectrophotometric calibration of the data. However, they do require extreme care in removing instrumental effects in order to achieve accurate relative calibration along both the dispersion and spatial directions. Proper subtraction of the sky and instrumental and far-field scattered light is also crucial. Finally, accurate flux calibration is required for the galaxy observations, particularly for long-baseline measurements such as those of molecular indices and full spectrum fitting. We went to great lengths to assure the highest possible quality in our final data products. In the interest of space, the detailed data reduction procedures will be described in a forthcoming paper.

3 EXTRACTING STELLAR POPULATION PARAMETERS FROM SPECTRA

Many different techniques can be used to characterize the stellar population parameters of an integrated (optical) spectrum. We have explored several of these in detail. Appendix B presents our analyses based on the Lick system of absorption-line indices and that of full spectrum single SSP fits. Both methods produce SP parameters based on SSPs and are thus extremely sensitive to the most recent episode of SF, even when its contribution to the SP in terms of mass is insignificant. The line index technique is also very sensitive to any ongoing SF as the emission lines from H II regions fill in the underlying absorption features, thus thwarting reliable age estimates. We conclude in Appendix C that the SPs of our spiral galaxies are not well represented by SSPs and an accurate representation must represent true average values of the SP parameters, i.e. integrated over the SFH of the galaxy. In the following sections we describe our devised method for achieving this goal, which is referred to as 'full population synthesis'.

3.1 Full population synthesis

Population synthesis is a technique applied to the integrated light of composite systems to determine the fraction of light (or mass) contributed by each of the main stellar groups comprising the system. Using a linear combination of stellar or model templates that cover the optical spectral range, the temperature mix of a galaxian (composite) system can be determined and used to explore its evolutionary history and to predict the flux of the system at other wavelengths as a test of the synthesis (Jacoby, Hunter & Christian 1984; Pickles 1985; Heavens, Jimenez & Lahav 2000; Cid Fernandes 2006; Tojeiro et al. 2007).

The 'full population synthesis' technique developed here consists of deconvolving an observed galaxy spectrum into basic components representing the relative contributions of a basis set of template spectra. It is important for the method of decomposition to allow for constraints to be placed on the computed parameters for which we turn to the method of *bound constrained optimization* (Zhu et al. 1994; Byrd et al. 1995; Zhu, Byrd & Nocedal 1997). The problem can be summarized as solving for

$$\begin{aligned} &\min f(x) \\ &\text{subject to } l \leq x \leq u \text{'} \end{aligned} \tag{1}$$

where $f(x)$ is the merit function which depends non-linearly, in general, on the fit parameters x_j, and l_j and u_j are lower and upper bounds, respectively, on each parameter x_j. Additionally, the gradient g of the merit function f with respect to the fit parameters must

be available. The algorithm performs the minimization iteratively where, at each iteration, the current fit parameters are varied by amounts determined by the current partial derivatives of the merit function. To start the iteration an initial configuration must be supplied.

Ideally, the locus of the merit function's minimum will be a single point in the vector space defined by the basis library of template spectra. The necessary conditions for this ideal case are: (1) the basis set is complete and non-redundant and (2) there is no noise in the data. In this situation the solution will be independent of the initial configuration. However, in any real synthesis we are limited by observational uncertainties, resolution, physical differences between the observed spectrum and model templates (e.g. abundance ratios, dust, emission lines from H II regions, any non-stellar contribution from AGN, etc.) and possible degeneracies in the library itself. Hence, the locus of the minimum merit function will be a finite volume in the basis space. The ultimate success of a population synthesis is therefore limited by the observational accuracy of the spectra and the match between data and template library.

3.2 The program

The problem of bound constrained optimization arises in numerous scientific and technical applications and has been an active area of research in the field of numerical analysis. As a result, there are now a number of robust optimization routines available; OPTIMA (Bartholomew-Biggs 1989) and LANCELOT (Conn, Gould & Toint 1992), to name a few. The program of choice for the present problem is that of Zhu et al. (1994, 1997) called L-BFGS-B.[3] This is a FORTRAN 77 code that solves large non-linear optimization problems with simple bounds. It has been well tested and is ideal for the current problem. A full description of the L-BFGS-B algorithm is beyond the scope of this paper, but the interested reader is referred to Byrd et al. (1995) and Zhu et al. (1994, 1997).

A driver program POPSYNTH was written which calls the L-BFGS-B routine. POPSYNTH performs the following steps.

(i) Set up input values for call to SETULB, the calling statement of L-BFGS-B.

(ii) Set up initial values for fit parameters x_j.

(iii) Read in the galaxy spectra and associated variance vectors, and the template library.

(iv) Compute the merit function and its gradient for the given set of fit parameters.

(v) Call the SETULB subroutine with the new merit function and gradient values.

(vi) Test for convergence, if not repeat (iv)–(vi).

(vii) Output stellar fractions to data files.

Zhu et al. (1997) provide a complete description of the input parameters, but a brief introduction is relevant here in order to understand the convergence criteria of the algorithm.

The input variable factr is a double precision number which defines a tolerance level in a termination test for the algorithm. The iteration will stop when

$$\frac{f_k - f_{k+1}}{\max(|f_k|, |f_{k+1}|, 1)} \leq \text{factr} * \text{epsmch},$$

where epsmch is the machine precision which is automatically generated by the L-BFGS-B code (equal to 2.22×10^{-16} on the Linux machine used for this project.) A value of factr $= 10^7$ was chosen for 'moderate' accuracy. Similarly, pgtol is a tolerance level for termination of an iteration if

$$\max(|\text{proj } g_i|, i = 1, \ldots, n) \leq \text{pgtol},$$

where proj g_i is the ith component of the projected gradient. For the current application pgtol was set to 10^{-5}. The iteration terminated according to the latter criterion for all tests and runs of the program.

The merit function to be minimized is defined as

$$\text{merit} = \left(\frac{1}{N - M} \sum_{i=1}^{N} R_i^2 \right)^{1/2}, \quad (2)$$

where

$$R_i = w_i(G_i - S_i). \quad (3)$$

In the above expressions, N is the number of data points included in the fit, M is the number of templates in the library, G_i is the observed galaxy flux at wavelength λ_i, w_i is the weight of the i th pixel (see Section 3.3) and S_i is the modelled galaxy flux at λ_i given by

$$S_i = \sum_{j=1}^{M} x_j F_{ji}, \quad (4)$$

where F_{ji} denotes the flux at the ith wavelength of the jth template, and x_j is the relative contribution of the jth template to the synthesized spectrum.

In order to prevent negative stellar contributions, as a non-physical artefact of the decomposition, the spectral coefficients are subject to a lower bound on the fit parameters such that

$$x_j \geq 0.$$

3.3 Weighting

The nature of our fitting algorithm is particularly useful for masking out undesirable regions in the spectrum. The following pathologies, which differ for each galaxy due, in most part, to velocity differences, are examples of regions that one may want to omit: (i) gaps in wavelength coverage due to the spacing between the three GMOS CCDs, (ii) strong and variable night sky line regions and (iii) emission line regions (due to H II regions and/or planetary nebulae). As a first guess, all of (i), (ii) and (iii) are masked for the initial fit of each spectrum. Subsequently, we allow for all points to enter back into the fit (subject to the constraints defined below) except for the gap regions, in which no real data exist, thus are always fixed to zero weight.

3.3.1 σ-clipping

We define a mask value, m_i, for each datum such that

$$m_i = \begin{cases} 1, & \text{include in current fit} \\ 0, & \text{remove from current fit} \end{cases}$$

and the weight, w_i, as

$$w_i = m_i \frac{1}{\sigma_i^2}, \quad (5)$$

where σ_i is the error on G_i.

In a general weighted fit, very dissimilar weights can be distributed among the data points. As a result, the number of datum, N, does not always relate directly to the actual information feeding

[3] Can be downloaded from http://www.ece.northwestern.edu/~nocedal/lbfgsb.html as of writing.

the fit. Instead, an effective number of points, $N_{\rm eff}$, can be estimated by the sum of the weights divided by the mean weight (González 1993) (note that in the following, all sums run from $i = 1, \ldots, N$, where N is the total number of data points):

$$N_{\rm eff} = \frac{\sum w_i}{\langle w_i \rangle} = \frac{\sum w_i}{(\sum w_i * w_i)/\sum w_i} = \frac{(\sum w_i)^2}{\sum w_i^2}. \quad (6)$$

Next we define the effective number of templates entering each fit, $M_{\rm eff}$. This is required as it is possible for a significant fraction of the total number of templates considered to end up with zero contribution to the fit. $M_{\rm eff}$ is defined as follows (here sums run from $j = 1, \ldots, M$, where M is the total number of templates considered):

$$M_{\rm eff} = \frac{\sum F_j}{\sum F_j^2/\sum F_j} = \frac{(\sum F_j)^2}{\sum F_j^2} = \frac{1}{\sum F_j^2}, \quad (7)$$

where F_j is the fractional contribution of SSP model M_j (thus $\sum F_j = 1$ by definition).

The expected variance (of the mean) based on the measurement errors is

$$\sigma^2_{\rm exp} = \frac{N_{\rm eff}}{\sum w_i}, \quad (8)$$

and the typical variance from the fit is

$$\sigma^2_{\rm fit} == \frac{N_{\rm eff}}{N_{\rm eff} - M_{\rm eff}} \left[\frac{\sum (w_i\, \Delta_i^2)}{\sum w_i} \right], \quad (9)$$

where $\Delta_i \equiv |G_i - S_i|$.

Finally, the fit χ^2 is the ratio of the mean typical and expected variances,

$$\chi^2 = \sigma^2_{\rm fit}/\sigma^2_{\rm exp}. \quad (10)$$

At each iteration, the quantities in equations (4)–(9) are computed and the individual masks, m_i, are assigned according to the criterion,

$$m_i = \begin{cases} 1, & \text{if } \Delta_i < N_\sigma\, \sigma_{\rm fit}, \\ 0, & \text{otherwise.} \end{cases}$$

On the first iteration we set $N_\sigma = 5$, the second has $N_\sigma = 3.2$, and two final iterations have $N_\sigma = 2.8$. We refer to this iterative masking scheme as 'σ-clipping'.

For our data, the typical number of data points for each spectrum is in the range $N = 1280$–1340; after the 'σ-clipping' iterations described above, the typical effective number of points in the final fit spans the range $N_{\rm eff} = 850$–1250. In this analysis we use $M = 70$ model templates (see Section 3.4) and typical values for $M_{\rm eff}$ are in the range 2–6.

3.4 Stellar population templates

The SP templates used throughout this analysis are from the models of BC03 which provide spectra of simple stellar populations (SSPs), single *Z*/single bursts of star formation. These cover the wavelength range 3200–9500 Å, a large range of ages (0.0001–20 Gyr), and metallicities ($Z = 0.0001$–0.05) at a reported resolution of $\sim$3 Å FWHM. We use here the models with the Chabrier (2003) initial mass function (IMF).

3.4.1 Template characterization

Given the importance of knowing the precise resolution of the templates for comparison with galaxy data and for measuring the small velocity dispersions of spiral galaxies (see Section 4.4), we undertook a deep investigation into the true resolution of the BC03 models, which use the spectral library STELIB of Le Borgne et al. (2003), for a range of model SSPs and allowing for a wavelength dependent (velocity-like, i.e. constant with $\Delta\lambda/\lambda$) term in addition to a term that is constant with wavelength. Our analysis is carried out using an upgraded version of the Movel algorithm described in González (1993). In brief, Movel derives velocity shift, velocity dispersion and γ (a measure of the relative line strengths, with $\gamma = 1$ indicating a perfect match) through a Fourier transform procedure. In velocity space, the observed galaxy spectrum can be characterized by the spectrum of its population convolved with the instrumental response function and a broadening function which characterizes the distribution of stellar radial velocities along the line of sight (LOSVD). The 'population' is represented by a template (observed or model) of higher resolution than the galaxy spectrum. Movel derives the broadening function that best matches the template to the galaxy spectrum. To then infer the absolute rotation and velocity dispersion parameters of the observed spectrum, one must know very accurately the characterization of the template used.

For the purpose of characterizing the BC03 resolution (both globally and as a function of wavelength), we use as a template spectrum the very high-resolution (effectively infinite for this application) solar spectrum of Wallace, Hinkle & Livingston (1998) along with the BC03 model SSPs, which are each effectively different co-additions (in relative weight and stars used) of stars in STELIB. The solar template and model SSPs are processed through Movel in 200 Å wavelength intervals centred around 26 spectral features, from 3575 up to 7400 Å defined by 21 Lick-like indices plus the Hα and Ca II H&K lines, and three more somewhat ad hoc regions shortward of Ca II H&K and longward of Hα to cover the full optical range. Spectral features in any given SSP that are not well characterized by the solar template are weighted out accordingly. We then fit the trend of resolution versus λ for a large range of SSP templates using three different constraints: (i) fitting for constant terms with both λ and velocity with both terms as free parameters, (ii) fixing FWHM = 3 Å and fitting for a velocity term and (iii) forcing only a linear FWHM component. This procedure revealed that *the resolution trend of the BC03 models is much better represented by a FWHM constant with λ plus a velocity term* (constant with $\Delta\lambda/\lambda$).

To investigate the cause of this discrepancy, we downloaded the STELIB library[4] and examined the individual spectra. First, we noted that the starting λ and dispersion are not all 3200 and 1 Å as stated in the documentation on their web site. The reason is that the 2003 v3.2 library stars had their radial velocities removed, but the spectra were not rebinned to the $\lambda_0 = 3200$ and disp = 1 Å. A look into the headers revealed a spread in the starting wavelength of $\rm rms_{\lambda_0} = 1.09$ Å and in dispersion of $\rm rms_{disp} = 0.000\,33$ Å. As these two differences in the relative wavelength calibration are correlated and, if fixed values are assumed when co-adding the individual stars, the combined effect will degrade the effective resolution of the model SSPs. In measuring the resolution as a function of wavelength for 12 individual solar type stars in the STELIB library we found, not surprisingly, that the individual stars are consistent with a pure constant resolution (no velocity-like broadening at all) and we measured the best constant FWHM to be 3.08 Å ($\pm$0.03). We thus concluded that the above-mentioned λ_0 and dispersion mismatch was not taken into account when the stars were co-added to create the BC03 model SSPs, thus resulting in a velocity-like broadening in addition to the constant resolution term. We also found a spread

[4] http://www.ast.obs-mip.fr/users/leborgne/stelib/index.html.

in the velocities of the 12 stars (whose measured relative velocities were removed in STELIB) with an rms = 11.4 km s^{-1}, which will also contribute to the velocity-like broadening of the SSPs.

The above procedure leads to the following conclusions about the true effective resolution of the BC03 SSPs. (i) The actual spectral resolution of the models is worse than 3.0 Å (significantly larger than for individual stars in STELIB). (ii) The best constant (no velocity broadening) FWHM is 3.40 Å (±0.04). (iii) If the 3.08 Å resolution derived for individual stars is assumed, the SSP models (co-added STELIB stars) need a significant additional velocity broadening (35.8 ± 3.6 km s^{-1}), but the fit is not as good as when assuming a constant ∼3.4 Å resolution. After exploring the fit results under all the above assumptions, the adopted (best) values for the FWHM resolution and velocity broadening for the BC03 models are found to be

$$\mathrm{FWHM_{BC03}} = 3.375\,\text{Å} \;\text{ and }\; \sigma_{\mathrm{BC03}} = 11.40\,\mathrm{km\,s^{-1}}.$$

These results can be understood as the combination (convolution) of: (i) the 3.08 Å FWHM resolution of each individual star, plus (ii) the 11.40 km s^{-1} radial velocity rms error in STELIB and (iii) an additional 1.38 Å residual FWHM degradation in the models due to the errors in the assumed initial wavelength and dispersions in STELIB in the co-addition of BC03.

Finally, we used the same solar template to map the wavelength scale of STELIB. The systematic deviations are no larger than $\Delta\lambda = -0.5$ to $+0.5$ Å across the observed wavelength range, yet are relevant enough for a fair comparison with high-quality modern data. These true systematic trends in resolution and wavelength scale of the BC03/STELIB spectra are in excellent agreement with those found in the similar analysis by Koleva et al. (2008).

In our full population synthesis fitting, all of the above is accounted for. In particular, we first distort our observed galaxy wavelength scale to match that of STELIB. We then account for resolution effects by convolving all model and galaxy spectra (at all radii) to the same resolution: top-hat = 10.81 Å, σ = 168 km s^{-1}. These account for the slit width and approximately highest velocity dispersion in our galaxy sample (measured on the first iteration and limited to the central, high-S/N regions), respectively. This dispersion is sufficiently greater than that of the native BC03 models such that any residual variations, e.g. due to different combinations of stars in different SSPs, will be smoothed out. We discuss in Section 4.4 our accounting for the BC03 effective resolution for kinematic measurements, which are iteratively derived from the full spatial and spectral resolution data.

3.4.2 SSP template library

We are limited here to a template library that comprises a discrete sampling of SSP ages and metallicities. Ultimately, we would like our library to be a complete and non-redundant basis set, but this would require an exact match between models and data that is not realized in practice. Through a series of tests and careful examination of the individual SSP spectra, we converged on a selection of SSPs at 14 ages, roughly logarithmically spaced,[5] and five metallicities (excluding only the lowest metallicity provided in the BC03 models which is the least well modelled and exhibits anomalous SSP spectra). This provides a total basis set of 70 SSP spectra, all shown in Fig. 2.[6]

We are interested in both the light- and mass-weighted contributions of each SSP to the integrated galaxian light. All SSPs in our library have been normalized to their *V*-band flux, so the *V*-band light-weight for SSP$_j$ is computed as (here sums run from $j = 1, \ldots, M$, where $M = 70$ is the total number of SSP templates considered):

$$l_j = x_j / \sum_j x_j, \tag{11}$$

and the mass-weight as

$$m_j = x_j * (M/L_V)_j / \sum_j [x_j * (M/L_V)_j], \tag{12}$$

where $(M/L_V)_j$ is the *V*-band mass-to-light ratio of the *j*th SSP. Thus the average light-weighted quantities are computed as

$$\langle \mathrm{A} \rangle_\mathrm{l} = \sum_j l_j * \mathrm{A}_j \qquad \text{and} \qquad \langle Z \rangle_\mathrm{l} = \sum_j l_j * Z_j, \tag{13}$$

and the mass-weighted as

$$\langle \mathrm{A} \rangle_\mathrm{m} = \sum_j m_j * \mathrm{A}_j \quad \text{and} \quad \langle Z \rangle_\mathrm{m} = \sum_j m_j * Z_j. \tag{14}$$

Finally, we also compute the stellar *V*-band *M*/*L* ratio of the composite system as $M/L_V = \sum_j [l_j * (M/L_V)_j]$.

A number of caveats exist when applying model SSPs to the integrated light of a star-forming galaxy. First, the models are based on empirical libraries of stars which are necessarily limited to the range of T_eff, [Fe/H], log(g) and [α/Fe] of stars within the solar neighbourhood. SPs in other regions in our Galaxy and in external galaxies will not be confined to this parameter space and thus not be faithfully represented. However, extrapolations in the (T_eff, [Fe/H], log(g)) space within the models do provide extensive coverage, with the extremes (low T_eff, small [Fe/H]) being the least well modelled. Additionally, the BC03 models do not include the effects of non-solar abundance ratios and a full assessment of potential biases awaits the upcoming implementations of SP models which include abundance pattern variations. Secondly, the models do not account for emission from planetary nebulae and H II regions which can be dominant in actively star-forming galaxies such as the late-type spirals in our sample. Indeed, many of our galaxy spectra show strong emission lines (e.g. Hβ, [O III] λλ5007, 4959, Hα, [N II], [S II], etc.; see Fig. A1). We successfully circumvent this issue with our iterative masking procedure described in Section 3.3.1. Thirdly, and again particularly important in star-forming systems, the optical stellar light will likely suffer from the extinction and reddening effects of dust. While there is no straightforward way to account for dust effects on integrated spectra, we attempt to determine if a particular spectrum is affected by extinction by comparing dust-free fits with those incorporating a model for dust extinction. We adopt the two-component dust model of Charlot & Fall (2000, hereafter CF00). The CF00 model accounts for the finite lifetime (∼10^7 yr) of stellar birth clouds through the parameter μ, which represents the fraction of total dust absorption contributed by diffuse interstellar medium (cirrus) dust. The wavelength dependence of the effective

[5] The spacing in not exactly logarithmic, particularly at ages of about 0.004 Gyr at the lowest *Z* values, where we noted anomalous SSP spectra in the BC03 models. The spectra around this age were inspected individually to find the 'best behaved' age (i.e. bluer for younger ages). The 0.006-Gyr SSPs had the most reasonable spectra.

[6] Note that we are not concerned here with model age predictions that are older than the age of the Universe. Model ages are not precisely calibrated and, as such, we are concerned primarily with relative trends.

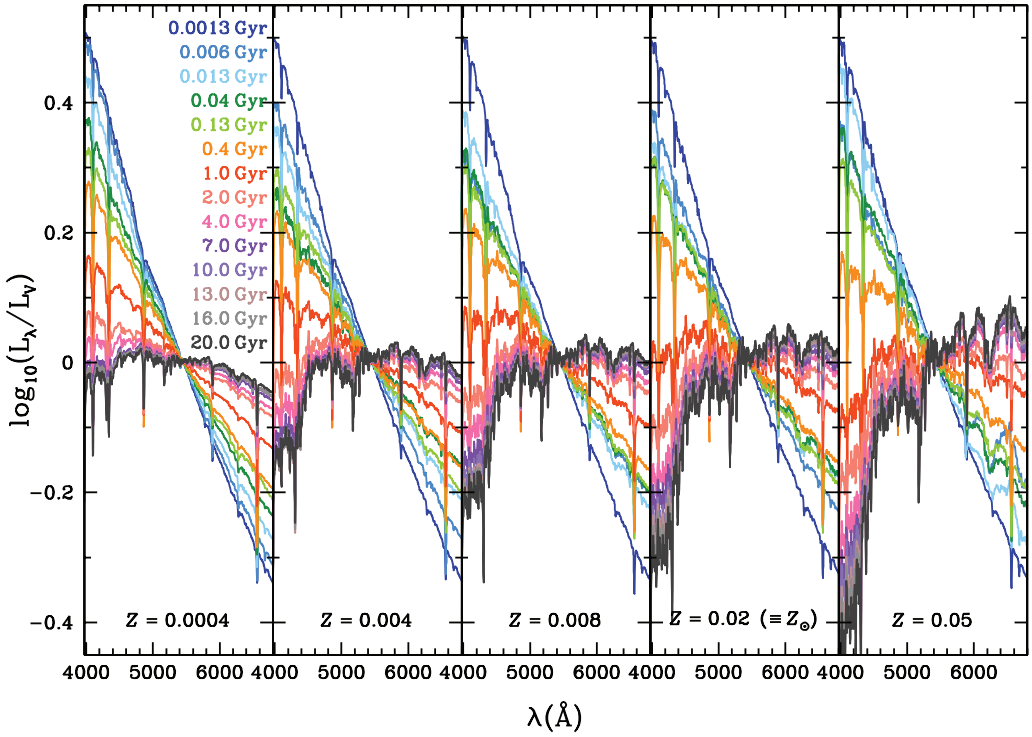

Figure 2. Spectra of the 70 SSP templates used in the population synthesis fits. Metallicity increases from left- to right-hand side. Different ages have different colours and are labelled in leftmost panel. All spectra are normalized to their *V*-band flux.

absorption curve is $\propto \lambda^{-0.7}$, so the 'effective' extinction in a given band, $\hat{\tau}_\lambda$, is given by

$$\hat{\tau}_\lambda = \begin{cases} \hat{\tau}_V(\lambda/5500\ \text{Å})^{-0.7} & \text{for} \quad t \leq 10^7\ \text{yr}, \\ \mu\,\hat{\tau}_V(\lambda/5500\ \text{Å})^{-0.7} & \text{for} \quad t > 10^7\ \text{yr}, \end{cases} \tag{15}$$

where t is the age of any single stellar generation.

For each SSP spectrum in our library, we create extincted versions with a fixed $\mu = 0.3$ (the average value for star-forming galaxies) and varying $\hat{\tau}_V$ in steps of 0.5. For reference, in this model, $\hat{\tau}_V = 2$ is equivalent to a colour excess $E(B-V) \sim 0.1$ for a solar metallicity template (see fig. 1 in MacArthur 2005). We perform the full synthesis first on the dust-free SSPs. The results are recorded and the merit function (equation 2) tabulated. The fits are then performed on the extincted SSPs, starting with $\hat{\tau}_V = 0.5$. If the merit function has decreased from the previous fit, the next extinction level is fitted, until a minimum in the merit function is reached. While the reddening effects of dust add an extra degeneracy to the fits, we always reach a convergence (minimum merit in the age/Z/dust space).

4 RESULTS

4.1 Full population synthesis fits

We here present example fits from the code and procedure described in Section 3.1. Fig. 3 shows the central, $r = 0$ arcsec, spectrum fit for all eight galaxies. In each plot, black and red lines are, respectively, the data and synthesis fits. The grey shading indicates regions masked in the fits as determined by our 'σ-clipping' procedure described in Section 3.3.1. Shown at lower right-hand side on each panel are the average light-weighted age, $\langle A \rangle_l$, and metallicity, $\langle Z \rangle_l$, effective $\hat{\tau}_V$ and χ^2 of the fit. The bottom panels show the per cent data–model residuals. In all cases, the full synthesis fits represent the galaxy spectra remarkably well. Our σ-clipping procedure clearly does a good job at masking out regions where emission lines are present.

Closer examination of the data–model residuals for all of the spectra that show little or no evidence for current SF reveal the same overall rolling shape, with the most significant feature occurring around $\lambda \sim 5150$–5450, a region rich with Fe and Mg absorption lines. While this may be due to a flux calibration problem, it could also be an indication of non-solar abundance ratios that are not taken into account in the BC03 models. A similar pattern was observed in the fit residuals of Sloan Digital Sky Survey (SDSS) galaxy spectra in the studies of Panter et al. (2007) and Cid Fernandes (2006). The fact that these independent data sets show the same features effectively rules out a flux calibration problem. Panter et al. (2007) suggest that these features may be due to an error in the balance of K–M giants in the BC03 models, whereas Cid Fernandes (2006) attributes them to non-solar α-element abundance ratios. We may be able to test this in future work with new SSP models that include non-solar α/Fe.

For now, however, the best diagnostic we have of α/Fe abundance comes from the Lick index measurements. In particular, in a plot of an index primarily sensitive to Fe versus one sensitive to an α-element, an enhancement in the latter can be identified if the data extend beyond the solar α/Fe model grids. We examine possible α-enhancement in our data in Fig. 4 where we plot $\langle$Fe$\rangle$ versus Mg b. For clarity, only the central, $r = 0$ arcsec, data point is plotted for each galaxy (for direct comparison with central spectra shown in Fig. 3). The black squares are measured directly from the galaxy spectra, whereas the pink squares are measured from the full synthesis model fits (red spectra in Fig. 3). By definition, the pink squares must lie within the model grids, thus a difference between

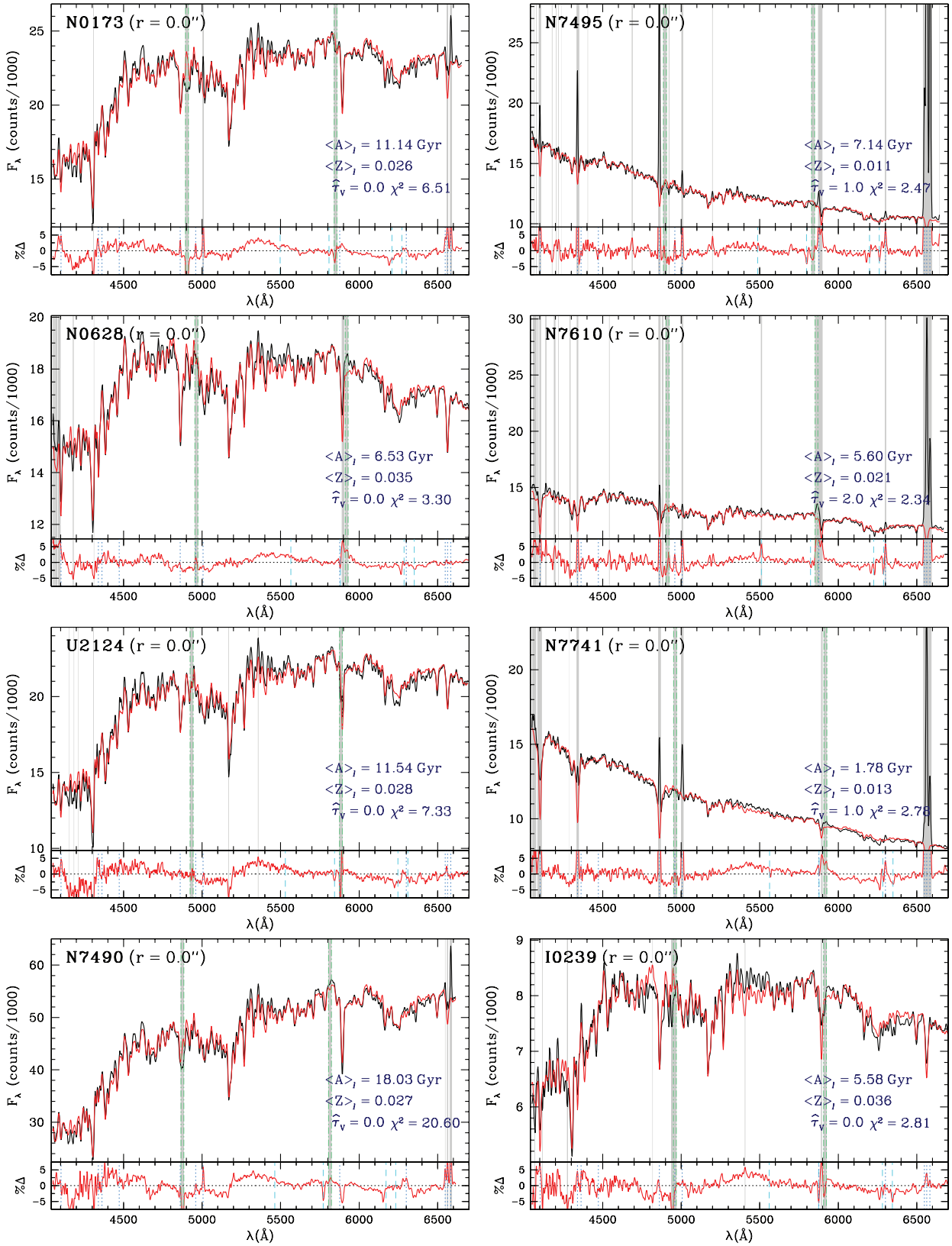

Figure 3. Central observed spectra (black) and full population synthesis fit (red) for all eight galaxies. Grey shading indicates regions masked in the fit as determined by our iterative 'σ-clipping' procedure (see Section 3.3.1) as well as the CCD gap regions (green vertical dash–dotted lines) which are always masked. Shown at lower right-hand side on each panel are the average light-weighted age, $\langle A \rangle_l$, and metallicity, $\langle Z \rangle_l$, effective $\hat{\tau}_V$ and χ^2 of the fit. The bottom panels show the per cent data–model residuals. In the bottom panels, dashed vertical lines indicate variable sky lines (which can be difficult to account for during sky subtraction), and dotted vertical lines indicate emission lines prevalent in star-forming (H II) regions.

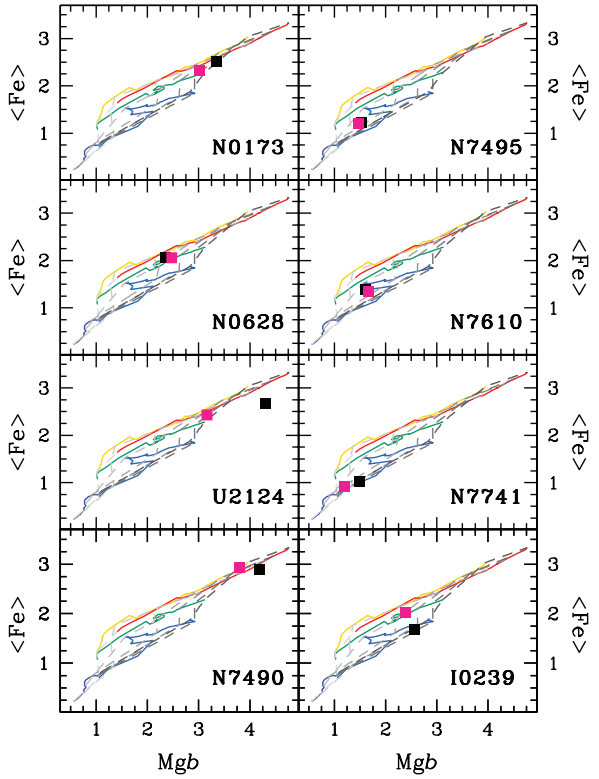

Figure 4. ⟨Fe⟩ versus Mg *b* as an indication of non-solar abundance ratios. Solid lines are iso-*Z* tracks with colour scheme: $Z = 0.05$ (red), 0.02 ($Z_\odot$) (yellow), 0.008 (green), 0.004 (light blue), 0.0004 (blue) and 0.0001 (purple). Grey-shaded dashed lines are iso-age tracks at ages of 1, 2, 5, 10, 13 and 20 Gyr (from light to dark shades; roughly left- to right-hand side). The black squares are measured from the data. The pink squares are measured on the model fit spectra.

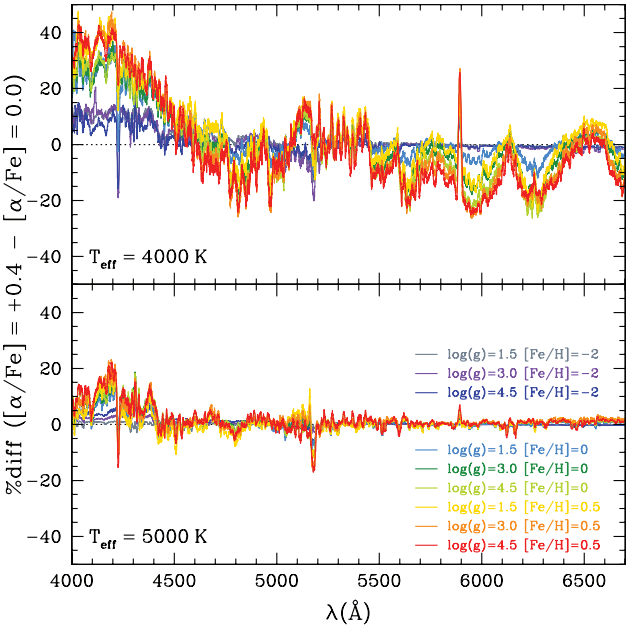

Figure 5. Comparison of solar versus $[\alpha/\mathrm{Fe}] = +0.4$ from models of Coelho et al. (2005), plotted as the per cent difference of enhanced minus solar scaled models, for effective temperatures of 4000 K (top) and 5000 K (bottom), and for a range of surface gravity and metallicity (as labelled in bottom panel).

the black and pink squares indicates that the models failed to reproduce the data simultaneously in this combination of narrow index regions. Indeed a few galaxies show signs of supersolar α/Fe ratios in their centres, with the most significant enhancement in U2124, which also shows the most prominent features in its full synthesis fit residuals (Fig. 3). This lends credence to the non-solar abundance ratio interpretation for the cause of the most prominent residuals that are not attributable to non-stellar radiation sources.

Another possibility to examine the conjecture that the dominant features of the fit residuals in Fig. 3 are due to non-solar [α/Fe] uses the synthetic spectral library of Coelho et al. (2005) who present models for a range of $T_{\rm eff}$, log(g) and metallicity, here expressed as [Fe/H], with varying abundance ratios. The effects of supersolar α/Fe are shown in Fig. 5 as the difference between the solar and enhanced α/Fe models of Coelho et al. (2005) for $T_{\rm eff} = 4000$ K (top) and 5000 K (bottom), for a range of log(g) and [Fe/H]. The effects depend strongly on $T_{\rm eff}$ and log(g), but some of the features and wiggles are similar to those seen in our galaxy–model fit residuals, thus strengthening the conclusion that the wiggles are due, at least in part, to abundance ratio effects. Individual features such as those seen in Fig. 5 at $\lambda \sim 4150$–4400, 4600, 5150–5450 (with a prominent feature at ∼5180 Å), and 6200–6300 Å, are most evident in the residuals for the central spectrum of U2124 in Fig. 3. The issue of abundance ratio variations will be examined in more detail in a future work.

Cid Fernandes (2006) also noted another striking feature in the data–model residuals of their mean spectrum for star-forming galaxies in the SDSS, selected on the basis of emission line diagnostic diagrams. This feature takes the form of a shallow but broad 'absorption' band around Hβ, that appears whenever stars of ∼100 Myr contribute significantly to the spectrum. While Cid Fernandes points out that no straightforward physical explanation nor element identification for this trough exists, he also speculates that it is a side effect of flux calibrations issues in the STELIB spectral library. We do not see such absorption troughs around Hβ for our star-forming galaxies (see e.g. N7495 in Fig. 3). We thus speculate that the trough seen by Cid Fernandes could be a residual trend from the resolution issues of the BC03 models described in Section 3.4.

4.1.1 Relative contribution of individual templates

It is interesting to investigate which of the 70 SSP templates are most represented in the fits. We have no reason a priori to think that the SSPs at any given age and Z will be more likely to represent the SPs of our spiral galaxy data, but it is possible that certain model SSPs suffer some systematic anomaly rendering them poor representations of real SPs (we certainly observed some such pathologies when selecting our 70 template SSPs, see Section 3.4). Table 3 shows the cumulative statistics of the contribution of each individual SSP template to the fits. Clearly, certain SSPs are favoured, with many never entering any fit. This is partly the reason for the stability in the fits. With 70 templates to choose from, one might expect the fits to be very sensitive to initial conditions, for example. We have tested the fits using various initial conditions and the results are extremely consistent. Given that typically fewer than 10 templates have non-zero weight in the fit, the stability is not as surprising. Interestingly, the solar $Z = 0.02$ SSP rarely makes it into any of the fits and only at the oldest three age bins, whereas all other Z values

Table 3. Statistics of individual SSP templates included in full population synthesis fits of integrated galaxy spectra.

Age (Gyr)	0.001	0.006	0.013	0.04	0.128	0.404	1.02	2.0	4.0	7.0	10.0	13.0	16.0	20.0
Z	Number of times each SSP template appears in any fit													
0.0004	282	20	1	0	0	10	6	27	108	2	26	0	0	2
0.004	0	11	0	7	5	194	1	0	26	0	10	129	99	66
0.008	70	0	0	1	0	6	6	0	0	9	33	3	0	0
0.02	0	0	0	0	0	0	0	0	0	0	0	2	6	109
0.05	0	65	5	0	1	17	233	28	37	48	10	23	187	97
Z	Cumulative *light* fraction for each SSP in all fits													
0.0004	2979.9	260.0	4.7	0.0	0.0	56.2	62.4	426.5	1898.3	9.4	601.5	0.0	0.0	15.7
0.004	0.0	110.4	0.0	99.4	81.4	2745.8	40.1	0.0	476.1	0.0	240.5	4593.8	1759.1	1834.2
0.008	911.3	0.0	0.0	12.5	0.0	31.0	123.3	0.0	0.0	77.6	662.2	56.1	0.0	0.0
0.02	0.0	0.0	0.0	0.0	0.0	0.0	0.0	0.0	0.0	0.0	0.0	22.0	65.9	2255.3
0.05	0.0	847.6	39.9	0.0	2.4	47.5	8483.2	257.7	357.9	532.0	116.4	242.0	2100.8	1159.9
Z	Cumulative *mass* fraction for each SSP in all fits													
0.0004	353.2	2.9	0.1	0.0	0.0	8.3	11.0	95.0	927.1	14.8	471.6	0.0	0.0	30.5
0.004	0.0	3.9	0.0	4.1	12.0	414.4	33.1	0.0	487.8	0.0	290.9	5053.0	2820.2	2928.9
0.008	41.3	0.0	0.0	0.1	0.0	4.1	126.7	0.0	0.0	82.3	869.8	128.4	0.0	0.0
0.02	0.0	0.0	0.0	0.0	0.0	0.0	0.0	0.0	0.0	0.0	0.0	35.7	128.0	3983.9
0.05	0.0	37.3	1.3	0.0	0.3	8.0	2910.5	136.9	735.7	1271.2	229.1	669.2	6979.5	4357.8

have some contribution at a range of ages. While it is difficult to identify the exact reason for this (e.g. perhaps the real parameter space is not fully represented in the models, or some systematic in the data forces it to certain areas of the model parameter space), an investigation based on fits to other SPS models may provide some insight, and will be the subject of a future investigation.

4.1.2 *Reliability of the fits*

To test the robustness of our method and results, and to associate reliable error estimates to the derived individual age, Z and $\hat{\tau}_V$ estimates, we perform a Monte Carlo (MC) analysis on a subset of radial bins for each galaxy. A full-blown MC analysis for every spectrum in our sample is computationally prohibitive, so the subset analysed was selected to be representative of the entire data set spanning the full range of S/N/Å, SED shape, emission strength and radial coverage of each galaxy. 20 realizations for each selected spectrum, after adding random noise, were then processed through our fitting algorithm in an identical fashion as the original galaxy data. Characteristic errors for the derived parameters are then taken as half the interval containing 68 per cent of the MC realization results (i.e. the 1σ confidence interval). Fig. 6 summarizes the results from this exercise, showing the difference between the parameters derived from each MC realization relative to the best-fitting value. There is evidence for a mild age/Z error correlation, and where not present, it turns up as an error degeneracy with $\hat{\tau}_V$. The errors are typically $\ll$10 per cent and, as expected, tend to increase with decreasing age, Z and S/N/Å. Error bars from these simulations are plotted in all subsequent figures. In particular, Fig. 8 reveals the radial sampling of the MC analysis.

Beyond the small errors of the mean SP parameters, the MC analysis also shows that the relative contribution of the individual SSPs, as well as the inferred SFHs (see Section 4.2), are preserved providing further confidence on the robustness of our results and method.

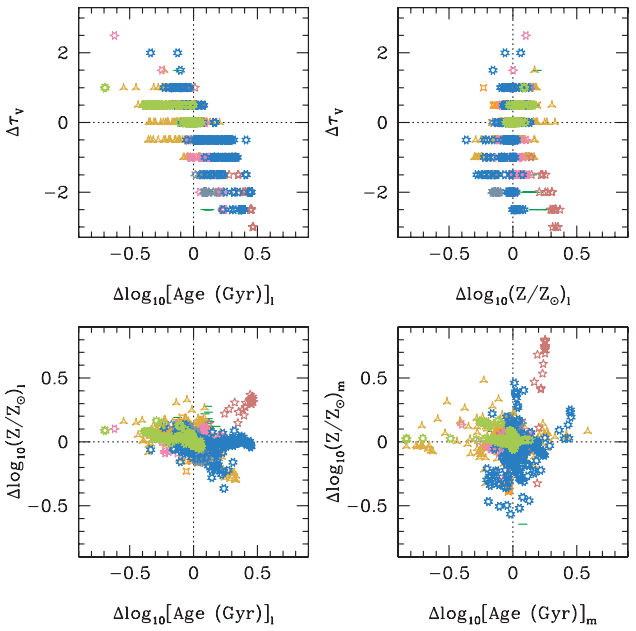

Figure 6. Results from MC simulations. Plotted are the logarithmic differences between the parameters measured in each MC realization and the best-fitting value. Point types and colours distinguish the different galaxies (see legend of Fig. C1).

4.2 Inferred star formation histories

Using full spectral synthesis, we are determining the best-fitting combination of SSPs at different ages and Z values that make up a given spectrum. As such, the SSPs included and their relative contributions to the spectrum can be regarded as a stochastically sampled SFH. We can thus examine the radial variation in SFH for each galaxy and look for signatures of star formation episodes that have occurred at specific locations within the galaxy. Fig. 7 displays a graphical representation of the radial variation in SFHs for all eight galaxies in our sample. In each panel, the vertical axis

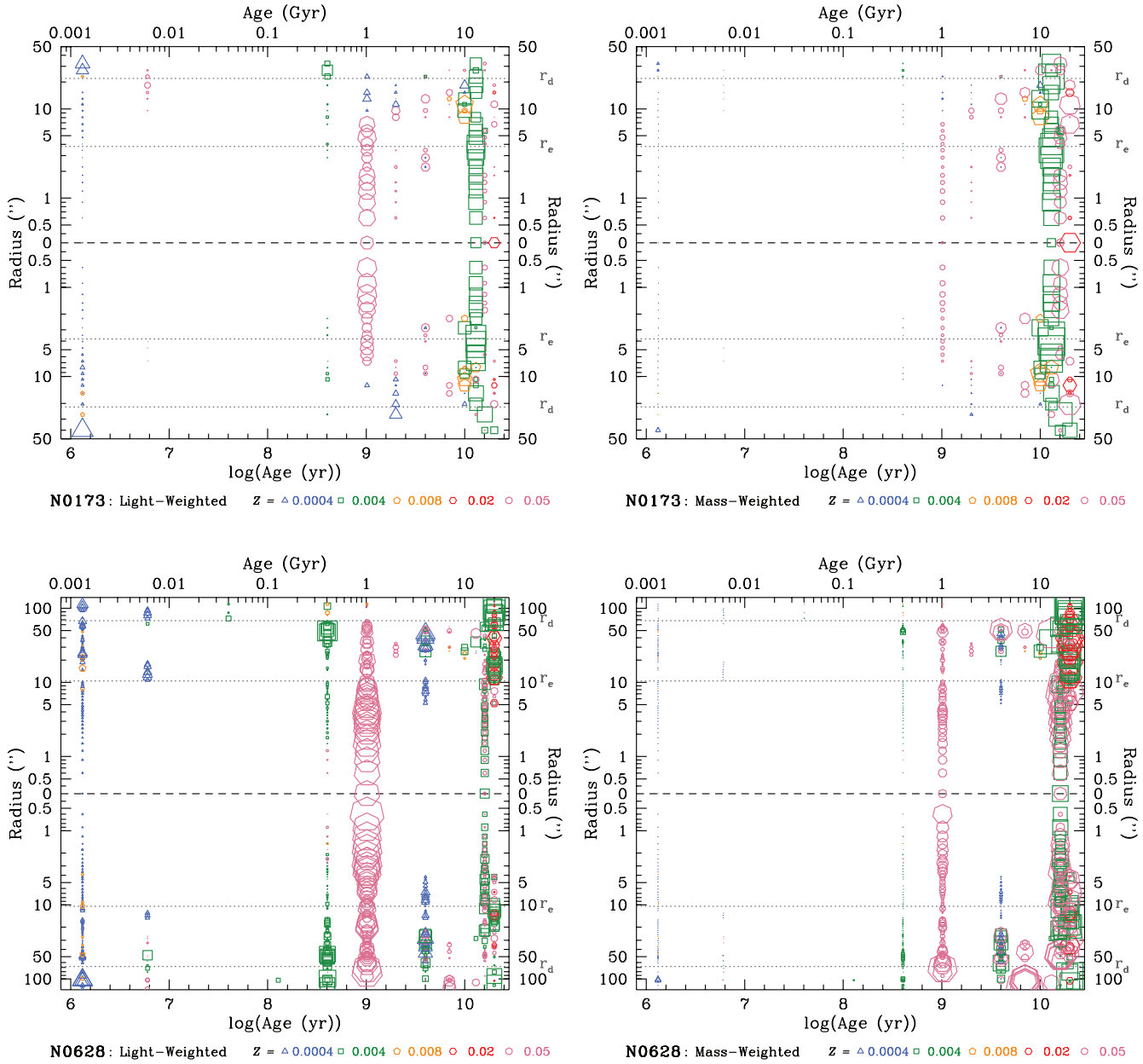

Figure 7. Light (left-hand panels) and mass (right-hand panels) weighted SFHs for all eight galaxies. In each panel, the vertical axis represents galaxy radius with the dotted line at $r = 0$ arcsec, and the horizontal axis represents SSP age. Point size is proportional to the relative weight in the fit and the colours and point types code the SSP metallicity. Left-hand panels show the light-weighted contributions and right-hand panels show their associated mass-weighted contributions. In terms of mass, the integrated spectrum at most radii is generally dominated by old and metal-rich population. The contribution of very recent star formation, while it can dominate the light (cf. N7495), is typically only a minor contribution to the stellar mass.

represents galaxy radius with the dotted line at $r = 0$ arcsec, and the horizontal axis represents SSP age. The point size is proportional to the relative weight in the fit and the colours and point types code the SSP metallicity. Left-hand panels show the light-weighted contributions and right-hand panels show their associated mass-weighted contributions.

Looking at a specific example, examination of the SFH for N7490 reveals that the bulge region is dominated in light and mass by an old population with solar metallicity. Further out into the disc, the light and mass become more dominated by a somewhat younger and more metal-poor population. It appears that there was an episode of high-metallicity SF 1 Gyr ago whose biggest contribution was at about the bulge/disc transition region ($r_e = 5.3$ arcsec for N7490), i.e. in a ring at that radius. While the contribution of this recent SF episode to the light is quite significant at some radii, it does not contribute significantly in terms of mass. Alternatively, looking at N7495, which has significant emission in its spectra at most radial bins (see Fig. A1), we see that the light is dominated by a very young (∼1 Myr), metal-poor population, likely due to a recent accretion of pristine gas, but the mass is still dominated at all radii by an old and metal-rich population.

In Table 4 we list for each galaxy the per cent light and mass contributions of 'young' (0.001–1 Gyr), 'intermediate' (2–7 Gyr) and 'old' (10–20 Gyr) age SSPs to the fits at three representative

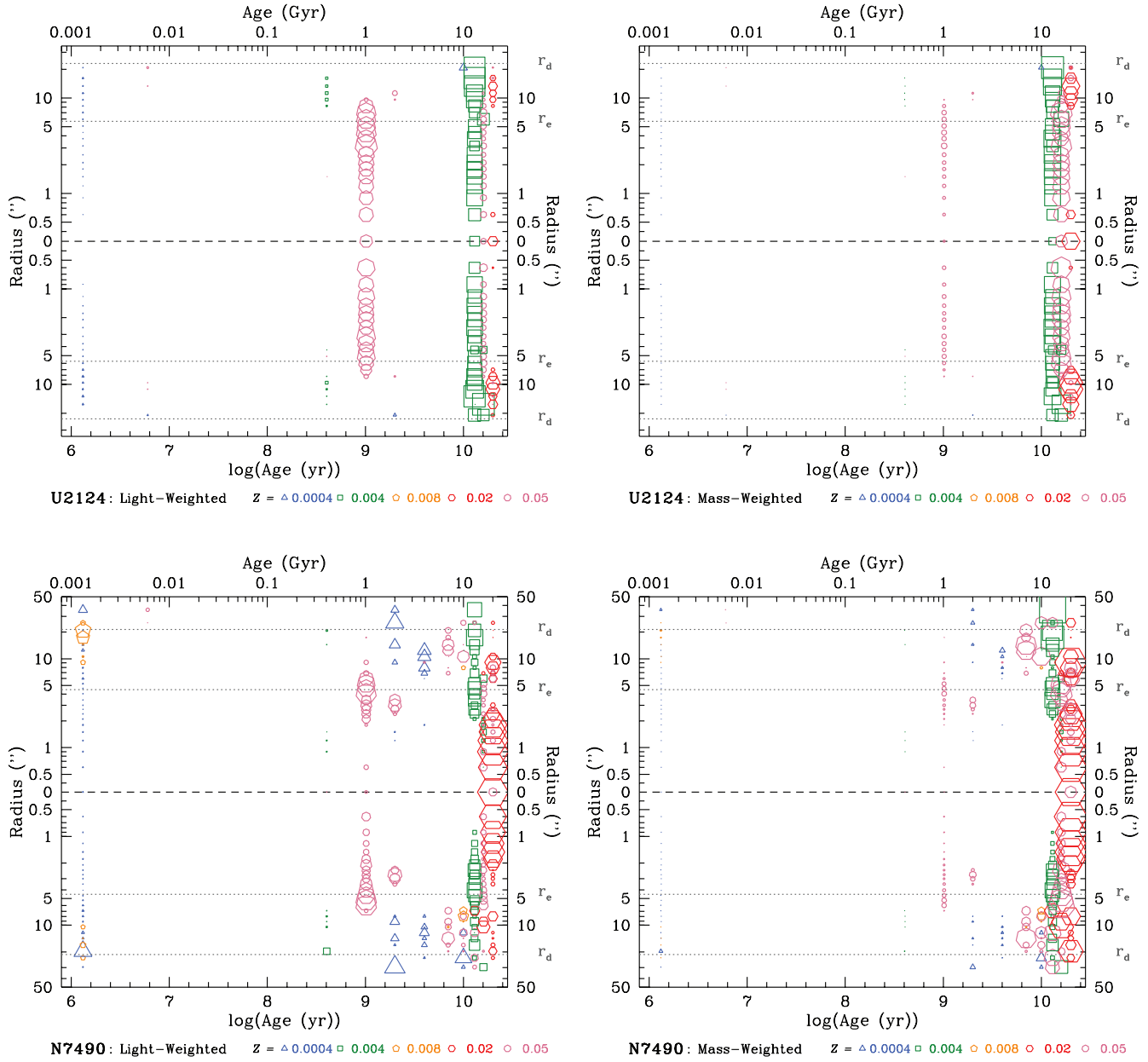

Figure 7 – *continued*

radii: $r = 0$, r_e and r_e. With only a few exceptions (r_d for N0628 and N7741 and r_e for I0239), the contribution to the stellar mass by the 'old' population is $\gtrsim$65 per cent at all radii, while its corresponding contribution to the light ranges from $\sim$10 to 90 per cent. Again with those exceptions, the contribution to the mass by the 'young' SPs is $\lesssim$25 per cent, while its light contribution is in the range $\sim$10–90 per cent.

Such observations are important for galaxy evolution studies in terms of the quantities that most strongly affect the SP content and predictions of a particular model. If one is more interested in the dominant component in terms of mass, the current SED can be very misleading, especially when interpreted in terms of SSP values. As we demonstrate in Section B3, many of these integrated late-type galaxy spectra are simply not well represented by single SSPs, particularly when there is current or recent SF (see Fig. B3, right-hand panel). While the concept of an integrated spectrum of a galaxy being dominated in mass by an old populations, but in light by a minor 'frosting' of recent SF is not new (e.g. Trager et al. 2000), the practice of using 'SSP-equivalent' ages is still in widespread use and could lead to misleading interpretations in their comparison with different types of galaxy evolution models.

Fig. 7 also demonstrates the relatively few SSP templates that enter each fit (see Table 3), as noted above. We return to a discussion of these SFHs in Section 5.1.

4.3 Stellar population gradients

Having refined our population synthesis procedure, we can now investigate the measured age, metallicity and dust extinction gradients in our sample galaxies. Fig. 8 presents the radial profiles of the

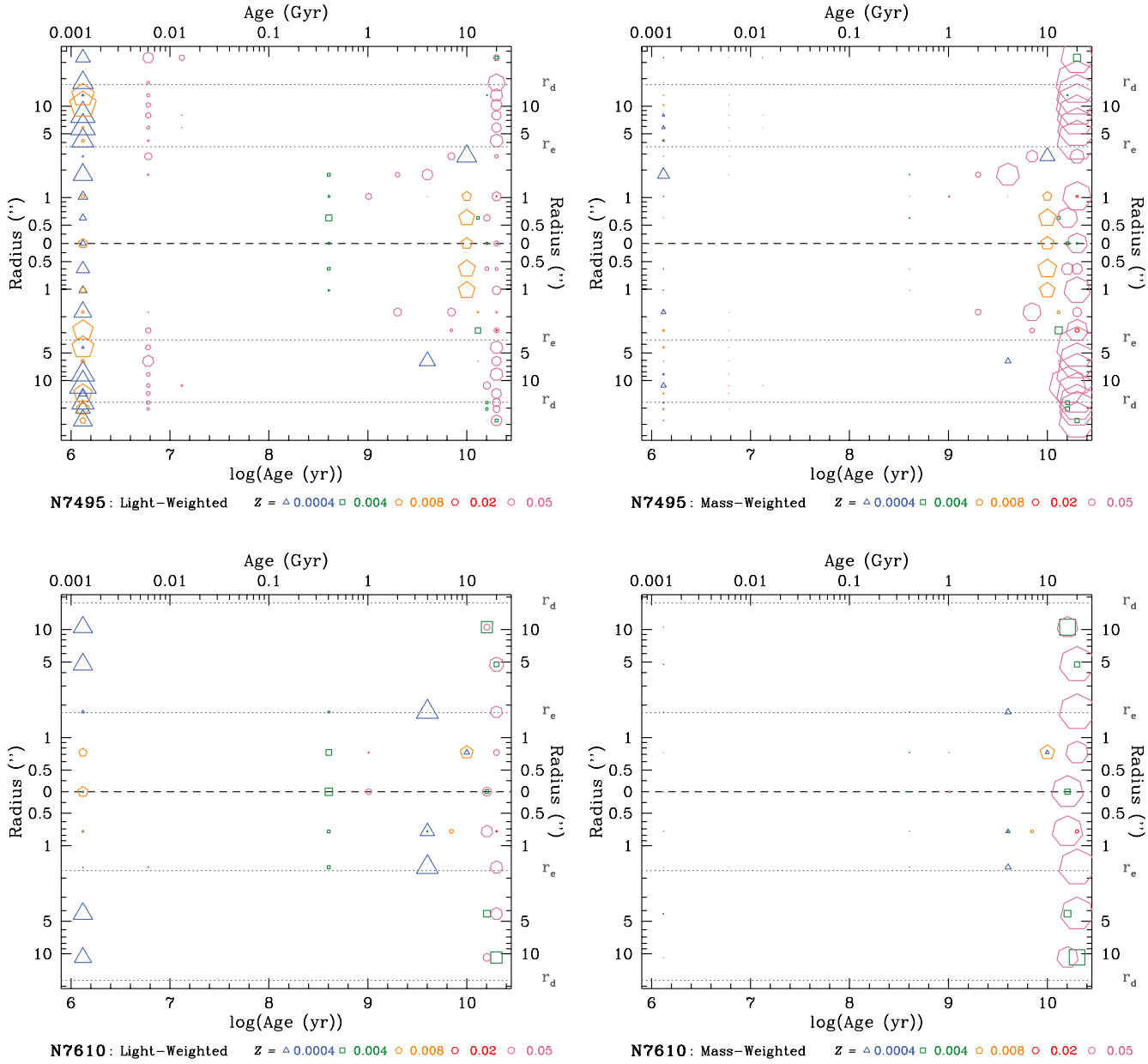

Figure 7 – *continued*

average age (top panels), average Z (middle) and $\hat{\tau}_V$ (bottom), for all our galaxies. The solid lines connect the radial bins for light-weighted quantities, while the dashed lines are for the corresponding mass-weighted quantities. The vertical dotted lines indicate the position of the bulge effective radius and disc scalelength (when reached). The profiles for both sides of the slit about $r = 0$ are shown, with one side distinguished by solid circles at each bin.

A first glance of these gradients reveals the remarkable consistency of the profiles on either side of the galaxy. A perfect match would not be expected given that spiral galaxies are not axisymmetric systems, but the similarities again provide confidence in the stability of our fitting technique for assessing relative trends (as all radial bins are modelled independently).

Any difference between the light- and mass-weighted quantities indicates recent SF activity on top of an underlying older SP. Indeed, most of the galaxies in our sample show evidence of recent SF all the way to the centre (the only exception being N7490 which, as we will see below, also has the largest central velocity dispersion in our sample). Additionally, to the extent that we measure them, all discs show evidence for some contribution from an underlying old ($\gtrsim$10 Gyr) population (see Table 4 for percentage contributions at r_d).

The dust content is generally small ($\hat{\tau}_V \lesssim 3$) and is always associated with very young SSPs ($\sim$1 Myr), as would be expected since star-forming regions are the sites of dust formation. The small implied dust extinction may seem at odds with the results of Driver et al. (2007) who, based on inclination-dependent bulge and disc luminosity functions for a sample of 10 095 galaxies, infer face-on B-band extinctions of up to 2.6 mag for bulges and 1.1 mag for discs. However, if the dust is largely concentrated in the plane of the galaxy, as is the case for the models they use with the scaleheight of the thickest dust component equal to $\sim$20 per cent of the bulge

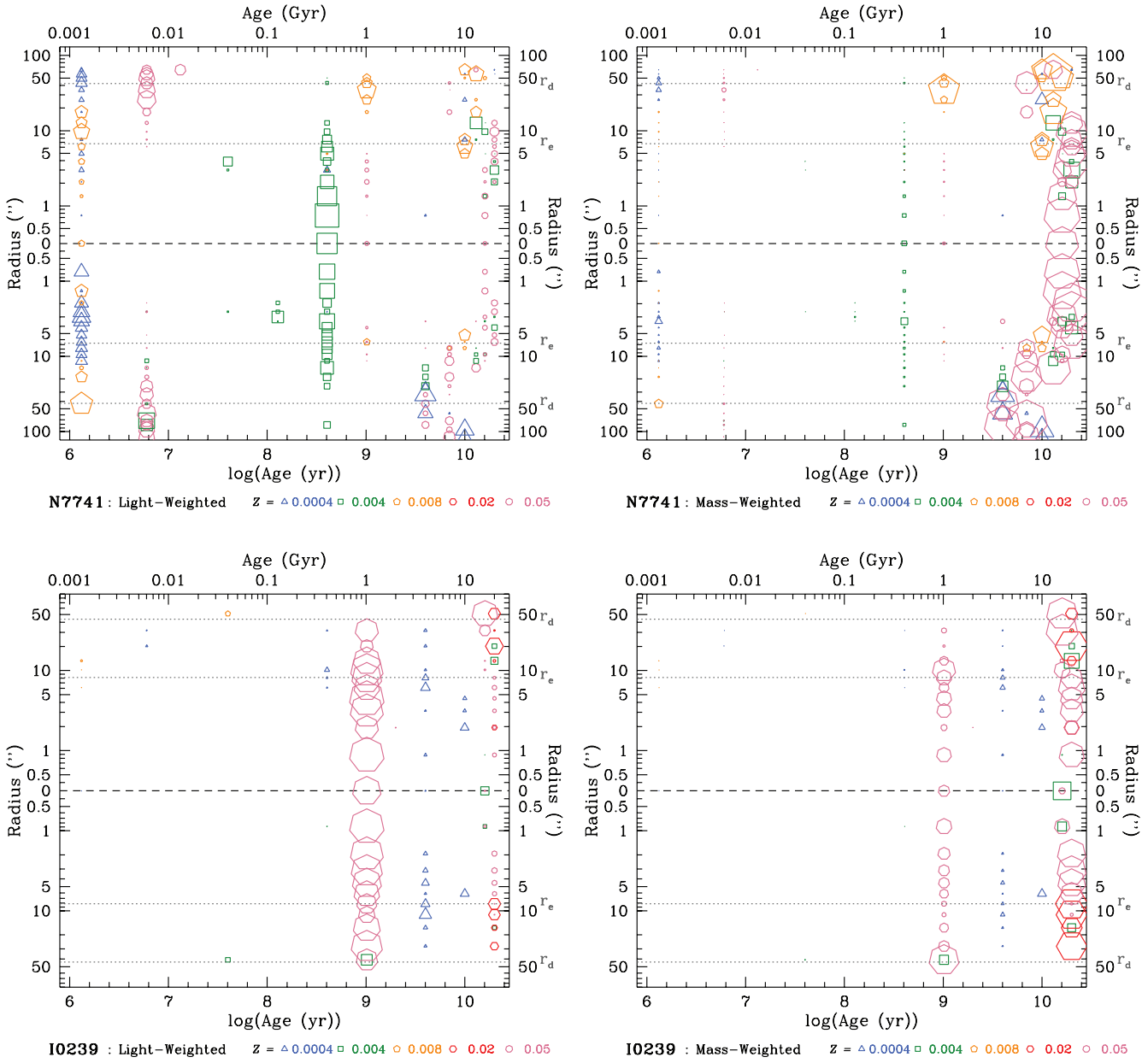

Figure 7 – *continued*

effective radius, the overall effect for a face-on bulge is that of near-complete attenuation of the stellar light behind the dust lane, rather than a reddening from light passing through the dust. Thus, even if such large attenuations exist in our bulges, because of the face-on orientations, we are observing non-extincted light from above the dust lane and thus would not expect our spectra to exhibit strong signatures of dust reddening.

The gradients themselves show a wide variety of behaviours. Within the bulge-dominated region, the light-weighted age profiles decrease in age with radius for N0173 and N7490, increase for N0628 and N7741, and approximately flat for U2124, N7495, N7610 and I0239, while the light-weighted Z profiles within the bulge decrease with radius for N0173, N0628 and I0239, increase for N7495 and N7741, and are approximately flat for U2124, N7490 and N7610. The discs, on the other hand, almost always show mildly decreasing to flat profiles in both age and metallicity. This diversity in SP gradients, and the fact that a trend in one is not necessarily associated with a trend in the other, allow for a variety of formation scenarios. This variety in observed gradients is also in qualitative agreement with those based on Lick indices of Moorthy & Holtzman (2006) for a sample of 38 spirals. We further discuss the gradients for individual galaxies in Section 5.1, also in the context of their kinematic profiles which are presented in the following section.

4.4 Stellar kinematics

We now turn to an analysis of the kinematics of our spiral galaxies. Given the intricacies involved in accurate measurement of absolute

Table 4. Per cent Contributions of all SSPs in given age ranges (young = 0.001–1 Gyr; intermediate = 2–7 Gyr; old = 10–20 Gyr) to fit for spectra at $r = 0$, r_e and r_d (when reached) weighted by light (V-band normalized) and mass.

		Light-weight			Mass-weight		
Name	Rad	0.001–1 (Gyr)	2–7 (Gyr)	10–20 (Gyr)	0.001–1 (Gyr)	2–7 (Gyr)	10–20 (Gyr)
(1)	(2)	(3)	(4)	(5)	(6)	(7)	(8)
N0173	0	32.75	0.00	67.24	5.66	0.00	94.34
	r_e	27.98	7.85	64.18	7.10	8.34	84.56
	r_d	7.82	21.44	70.73	0.14	3.54	96.32
N0628	0	62.98	0.00	37.02	19.41	0.00	80.59
	r_e	45.43	6.78	47.80	7.54	2.26	90.20
	r_d	79.53	16.56	3.90	50.20	27.44	22.35
U2124	0	30.00	0.00	70.00	5.03	0.00	94.97
	r_e	45.32	0.00	54.68	10.94	0.00	89.06
	r_d						
N7490	0	10.20	0.00	89.80	0.73	0.00	99.27
	r_e	42.29	0.00	57.71	9.73	0.00	90.27
	r_d	45.31	14.27	40.41	5.56	29.82	64.62
N7495	0	47.02	2.61	50.37	2.17	0.64	97.19
	r_e	61.18	6.46	32.36	5.40	11.27	83.33
	r_d	68.45	0.00	31.55	1.81	0.00	98.19
N7610	0	66.59	0.00	33.41	8.08	0.00	91.92
	r_e	14.48	56.96	28.55	0.70	16.12	83.18
	r_d						
N7741	0	91.16	0.00	8.84	23.51	0.00	76.49
	r_e	53.22	0.00	46.78	4.23	0.00	95.77
	r_d	99.88	0.12	0.00	98.20	1.80	0.00
I0239	0	66.75	3.42	29.83	26.50	1.92	71.58
	r_e	74.87	18.27	6.86	36.37	13.09	50.55
	r_d	60.10	8.83	31.07	12.57	2.83	84.59

velocity dispersion and rotation profiles with long-slit observations, we provide below a fairly detailed description of our procedure.

4.4.1 Measurement of stellar velocity dispersion and rotation profiles

For velocity dispersion, σ, and radial velocity, V_{rot}, estimates we used the Movel algorithm (updated from González 1993), first introduced in Section 3.4.1. The population templates are now the composite SP fits obtained in Section 4.1.

In addition to a careful characterization of the resolution and wavelength calibration of our GMOS data (Section 2), in Section 3.4.1 we also explored in detail the absolute spectral resolution, as a function of wavelength, as well as the wavelength scale of the BC03 models. For the derivation of absolute σ values and rotation curves, the templates were first corrected by the systematic error in their wavelength calibration derived in Section 3.4.1 (note that for the SP fitting, it was the galaxy data that were distorted to the STELIB wavelength scale).

The GMOS resolution is very well characterized by the convolution of a top-hat slit resolution of 10.81 ± 0.01 Å and a Gaussian instrumental resolution of 0.8 ± 0.02 Å. Strictly speaking, however, this resolution only applies to regions where the galaxy effectively fills the 2 arcsec slit. Towards the centre of each galaxy, where the galaxy structures become significantly smaller than the slit width, an object can no longer be considered extended, and the actual resolution is given by the convolution of the galaxy surface brightness profile, the seeing FWHM, and the spectrograph internal (after the slit) resolution (0.8 Å). Using the observed spectroscopic brightness profile of each galaxy and taking into account the measured anamorphic amplification, we created 2D effective resolution maps. In the Movel procedure, each galaxy is first convolved with the residual resolution of the templates (FWHM $= \sqrt{3.4^2 - 0.8^2}$ Å and $\sigma = 11\,\mathrm{km\,s^{-1}}$) while the template for each galaxy radial bin is convolved by its corresponding row in the 2D effective resolution map of the galaxy. In this fashion, Movel can then extract absolute velocity dispersions, since both galaxy and templates are now well matched at all points along the slit.

The templates are generated for bins along the slit that have been co-added to accumulate S/N/Å ≥ 50. To avoid artificially broadening each radial bin, the bins must be co-added after removing the rotation shape. This is achieved by iteration, where we first interpolate the template fits for each co-added bin and use them in the unbinned data (continuous 0.07 arcsec pixel^{-1} sampling along the slit) to derive and remove the rotation curve. We then reconstruct the minimal S/N bins and derive the absolute σ values and the small residual correction of the radial velocity at each co-added bin.

In Fig. 9 we present the results from our Movel determination of the galaxy kinematic profiles. For each galaxy, we plot the velocity dispersion profile (top panel), rotation curve (middle panel), and γ profile (bottom panel). Note the different scales for each galaxy. Recall that γ is a measure of the relative absorption strengths between galaxy and template, with $\gamma = 1$ representing a perfect match. In addition to obvious potential culprits inherent to the data reduction process (sky line subtraction, relative flux calibration, etc.), strong deviations from $\gamma = 1$ could indicate a region in parameter space that is not represented in the models. For example, a mismatch of abundance ratios between the models (which only include solar neighbourhood abundance patterns) and galaxies as described in Section 3.4.1 (see e.g. U2124), or at low age/Z where the stellar libraries are sparse (see e.g. N7741). It could also indicate a spectrum whose emission-line fill-in did not get fully masked out in our 'σ-clipping' procedure described in Section 3.3.1. For the most part, however, γ is quite close to 1 indicating a good match between galaxy and model fits.

The kinematic profiles generally show a rapid decrease in velocity dispersion outside the bulge effective radius and fairly well-defined rotation curves. However, given the face-on nature of this sample, the correction to absolute rotation speed [i.e. sin (i)] is quite large and uncertain. For N0628 and U2124, the odd rotation profiles reveal a poor alignment of the slit on the nucleus of the galaxy. Regardless, our σ profile for N0628 is very well matched to that of Ganda et al. (2007; hereafter Ganda07), indicated by the red lines, which was derived from 2D SAURON data.

The dominance of rotational versus random motion support of the bulges of our spiral galaxies can be isolated and compared with pure elliptical systems in the $(V_{\mathrm{max},r_e}/\sigma_0, \epsilon)$ plane. Here, V_{max,r_e} is the maximum rotational velocity measured within the effective radius of the bulge, σ_0 is the central velocity dispersion, measured within an effective aperture of $r_e/10$ (and labelled as $\sigma_{r_e/10}$, see below). The bulge ellipticity, ϵ, also measured at r_e, is derived from the isophotal SB fitting (see Mac03 for details). The location of our bulges in this plane is shown in Fig. 10. The solid curve represents the location of oblate spheroidal systems with isotropic velocity dispersions that are flattened only by rotation (Binney & Tremaine

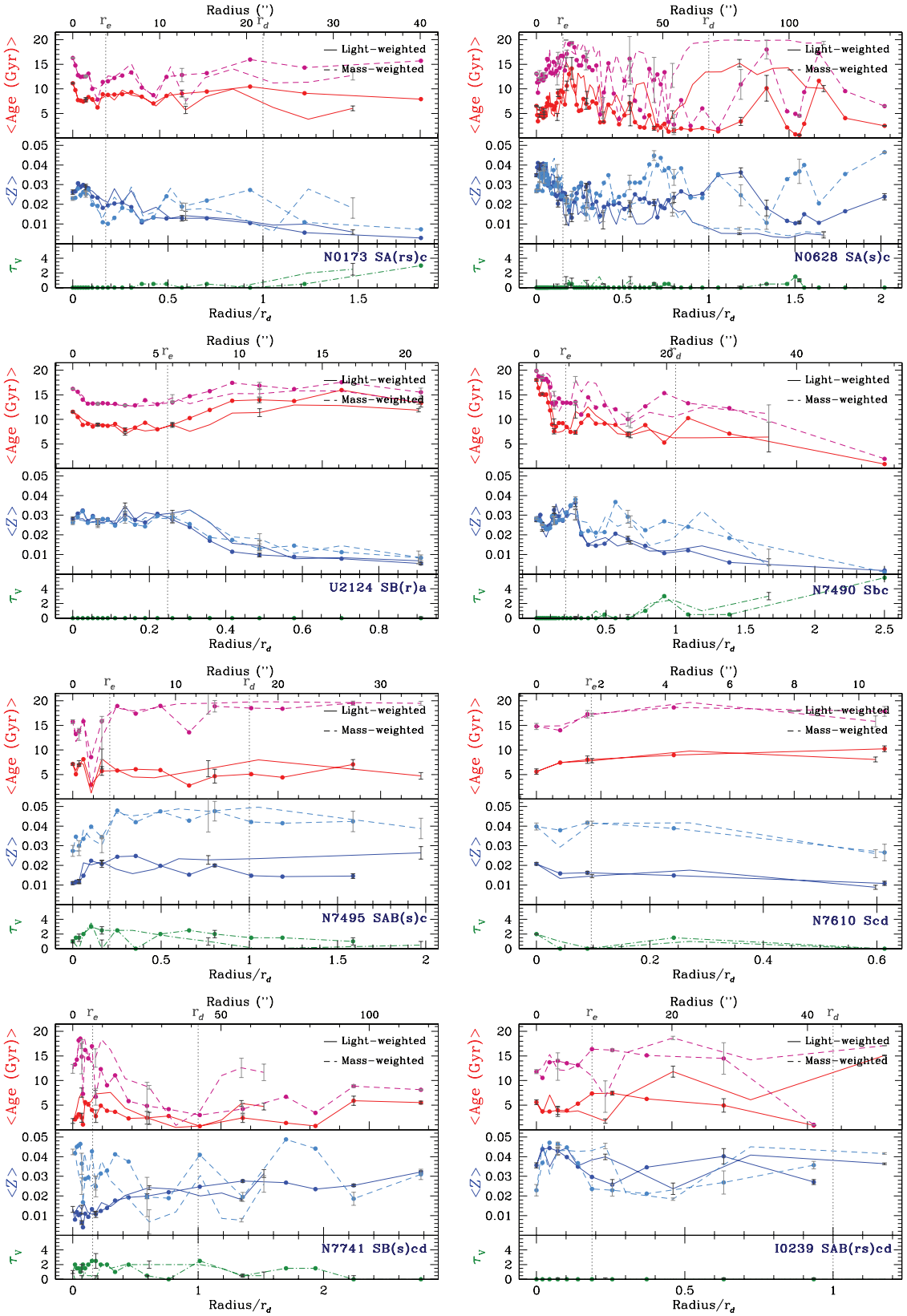

Figure 8. Light and mass-weighted average age and metallicity gradients from our full population synthesis fits. Plotted in each panel are the average age (top), average metallicity (middle) and $\hat{\tau}_V$ (bottom) as a function of radius. The solid lines indicate light-weighted quantities, while dashed lines are the corresponding mass-weighted values. The variations for both sides of the slit are shown, distinguished with one side showing solid circles at each radial bin. Perfect symmetry in the gradients is not expected due to the non-axisymmetric nature of spiral galaxies, but the consistency is quite remarkable. Error bars are displayed (dark grey for light-weighted and light grey for mass-weighted quantities) at all radii for which MC simulations were done (see Section 4.1.2). Vertical dashed lines indicate the position of the effective radius and disc scalelength (when reached).

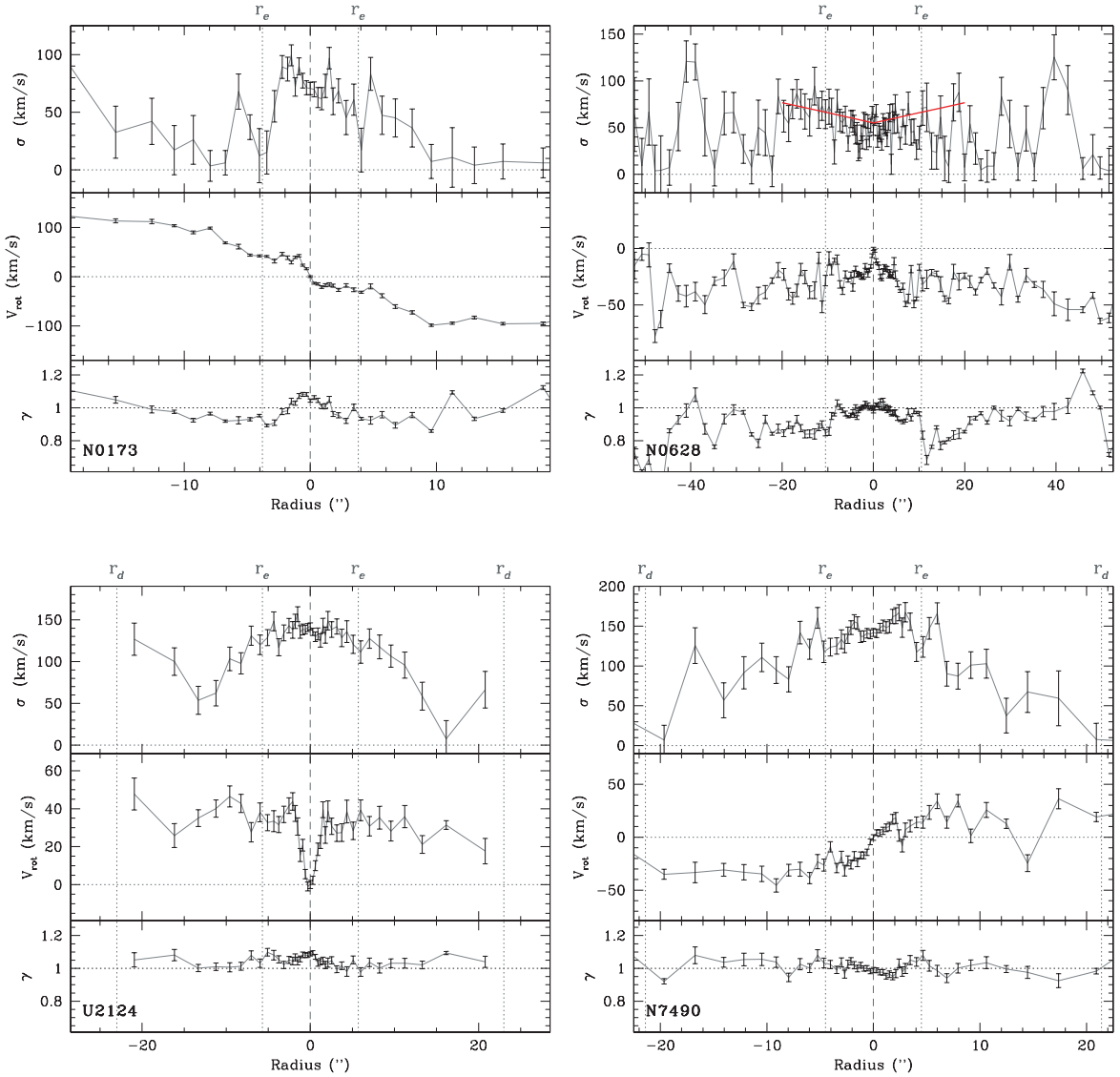

Figure 9. Kinematic profiles for our eight galaxies. Plotted in each panel are the velocity dispersion, σ, in km s^{-1} (top), rotational velocity, $V_{\rm rot}$, in km s^{-1} (middle) and the γ parameter (mean relative line intensity) of the kinematic fits (bottom) as a function of radius. The radial scale extends to 5 $r_{\rm e}$ and note the different vertical scales for each galaxy. The galaxy centre is marked by the dashed line, while the bulge effective radius, $r_{\rm e}$, and disc scalelength, $r_{\rm d}$, when reached, are marked by dotted lines. For N0628, the red lines in the top panel indicate the velocity dispersion profile fit derived by Ganda07, showing good agreement.

1987). Three of our bulges lie above the oblate line, indicative of the discy behaviour expected of bulges that have undergone secular evolution, whereas a distinction between 'pseudo' and 'classical' for the other four bulges, which lie close to, but below the oblate line, is not as clear-cut. Note that the large uncertainties in N7741 result largely from the very low velocity dispersion of this galaxy and its large ellipticity is due to its dominant stellar bar.

The main kinematic parameter of interest for this paper is the central velocity dispersion. This was measured as a light-weighted average within a effective aperture of $r_{\rm e}/10$ for direct comparison with the elliptical galaxy sample of Thomas et al. (2005). The average ages and metallicities within this central $r_{\rm e}/10$ aperture were also computed and the values are listed in Table 5.

4.5 Age and metallicity versus central velocity dispersion

We can now assess any trends in the age and metallicity of our spiral bulges as a function of velocity dispersion. In Fig. 11 we plot light- (solid black squares) and mass- (red open squares) weighted average age (top panel) and Z (bottom panel) for our eight bulges. Simple linear least-squares fits to both trends are shown in the legends. The light-weighted values follow the expected trend of increasing average age and metallicity with larger $\sigma_{r_{\rm e}/10}$. However, when regarded from a mass-weighted point of view, both trends essentially disappear, indicating that the mass of all spiral bulges is dominated by a population of very old and metal-rich stars.

4.6 Comparison with other studies

Most studies of the SPs of spiral bulges and ellipticals to date have focused on Lick index measurements. As outlined in the appendixes, such measurements are subject to a number of limitations, particularly in the case of star-forming systems. The biggest limitation is due to emission-line fill-in of the strongest age discriminators, the Balmer absorption lines. With high-quality spectra, however,

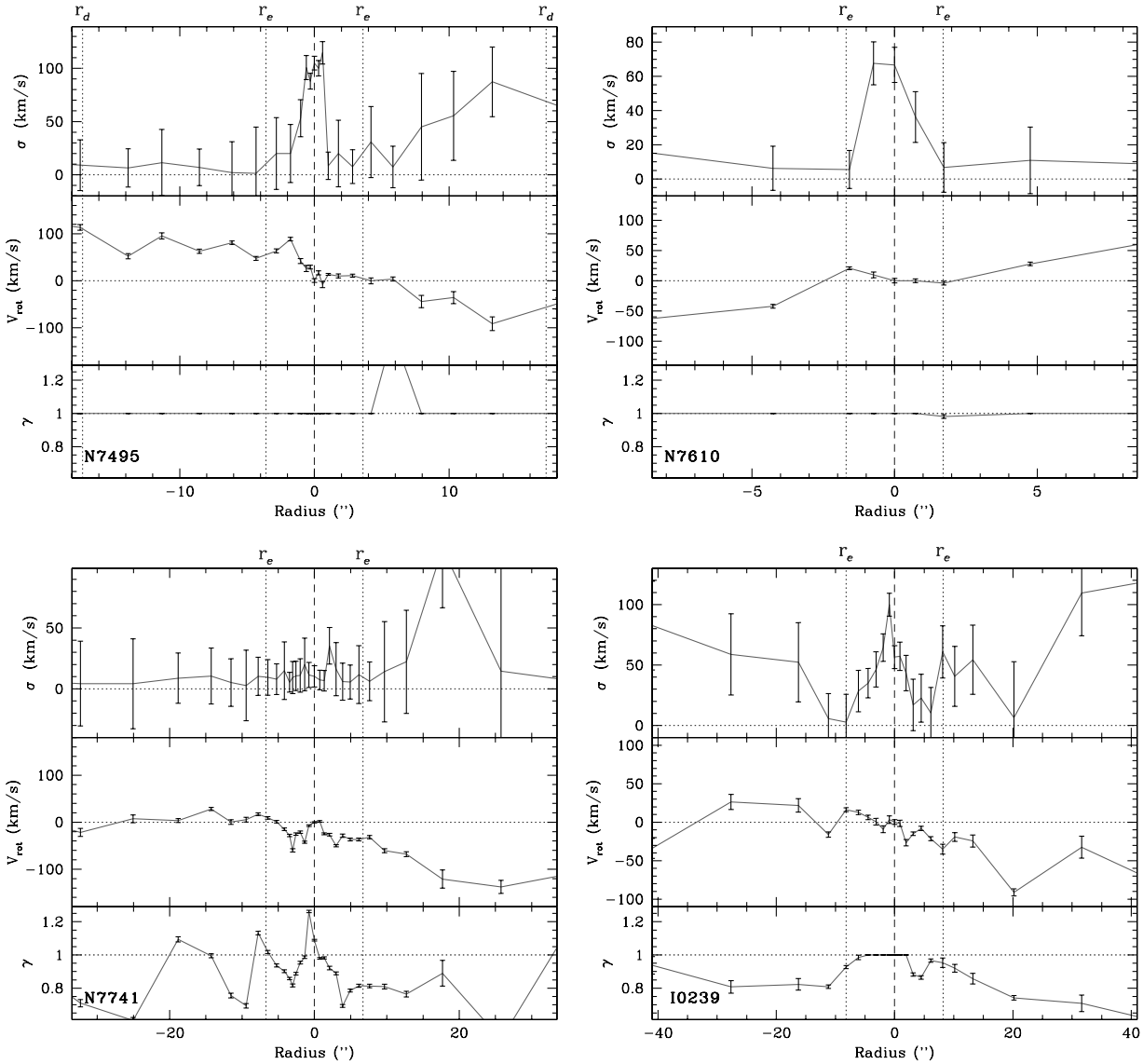

Figure 9 – *continued*

this limitation can be largely overcome with a careful subtraction of the emission-line contamination to the indices, as was done in the work of Ganda07 based on SAURON data. The method used is described in Sarzi et al. (2006) and was also applied in the study of Morelli et al. (2008). We thus consider the age and Z estimates in the Ganda07 and Morelli et al. (2008) samples to be appropriate for direct comparison with the Lick index-based estimates for early-type galaxies in the sample of Thomas et al. (2005). All of the above studies provide SSP-equivalent values, and we note that these are 'light-weighted' and not strictly 'average' values in the same sense as ours which implicitly measure the fractional contribution of each SSP to the galaxy flux, normalized to the V band. As such, small differences in the fractional light contributions of different SPs can cause large scatter in the derived parameters. This effect is clearly seen in Fig. 12 where we plot the results from this paper along with those from the early-type sample of Thomas et al. (2005) and the bulge samples of Ganda07 and Morelli et al. (2008). See the figure caption for a description of the different data sets.

A direct comparison of absolute ages is difficult due to differences in the models used to derive them. Of particular note are the extreme ends of the age ranges used: the models of Thomas et al. (2003), which are used in all three of our comparison studies, cover SSP of ages 1–15 Gyr, where as the largest age SSP from the BC03 models is 20 Gyr and we include those as well as 16-Gyr SSPs in our modelling (see Fig. 2). Thus, our age predictions will tend to biased to larger ages whenever an SSP of age $\gtrsim$13 Gyr is included. At the young end, we include ages from BC03 down to 1.3 Myr, thus our ages could be biased young whenever SSPs of age < 1 Gyr are indicated. This would have the overall effect of increasing the slope of the age–σ_0 relation derived from our methods. The black dashed line in Fig. 12 is the best-fitting scaling relation for low-density environments derived in Thomas et al. (2005) based on MC simulations (which assume linear correlations of the parameters age, metallicity and α/Fe ratio with $\log\sigma$ and account for observational errors and intrinsic scatter in all three parameters). Indeed, if we compare the slope of the Thomas et al. (2005) fit with our own

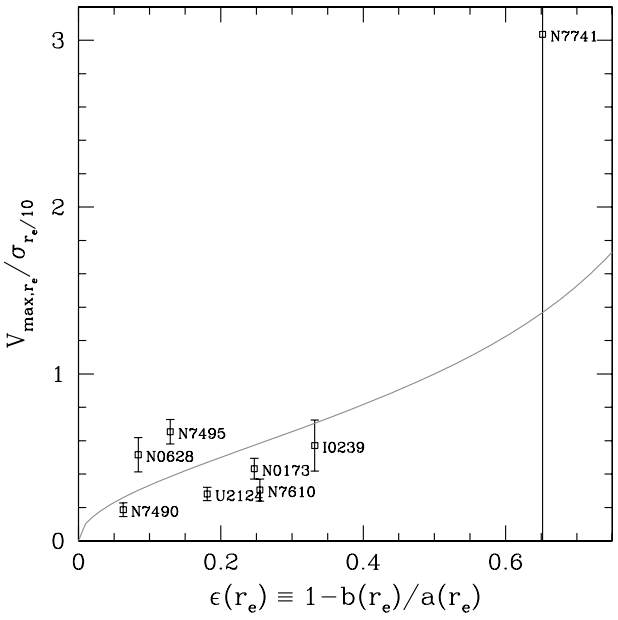

Figure 10. Location of our bulges in the ($V_{\mathrm{max},r_e}/\sigma_0$, ϵ) plane. $\sigma_{re/10}$ is taken from Table 5. V_{max,r_e} and $\epsilon \equiv 1 - b/a$ were measured at the bulge effective radius from the kinematic profiles and isophotal SB fitting, respectively. The solid curve ($V_{\mathrm{max}}/\sigma_0 \simeq [\epsilon/(1-\epsilon)]^{1/2}$, from Kormendy 1982) describes oblate-spheroidal systems with isotropic velocity dispersions flattened only by rotation (Binney & Tremaine 1987).

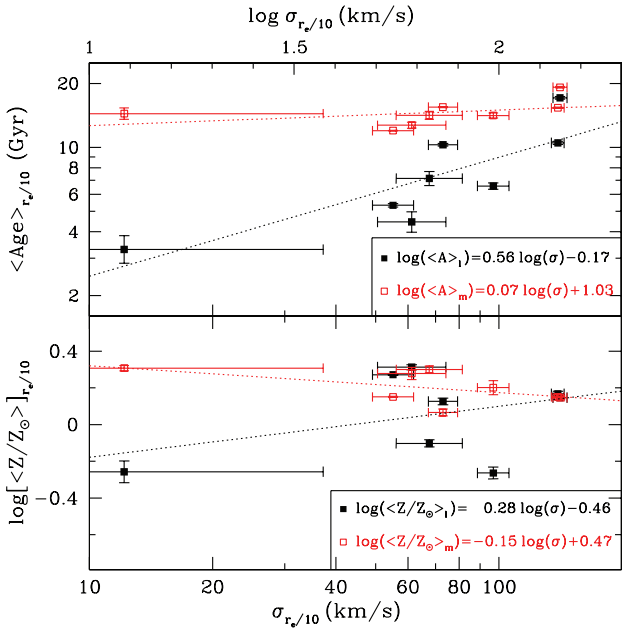

Figure 11. Average age (top) and metallicity (bottom) as a function of the central velocity dispersion. Black solid squares: Our data in a $r_e/10$ aperture (actually $r_e/10 \times 2$ arcsec due to the slit width). These are the light-weighted values from the POPSYNTH fits. Red open squares: Same as black but for mass-weighted values. The black and red dotted lines are simple linear regression fits to the light- and mass-weighted data, respectively, and the fit parameters are indicated in the legends.

Table 5. Average age, Z and σ within $r_e/10$.

Name NGC	$\sigma_{r_{e/10}}$	d$\sigma_{r_{e/10}}$	$\langle A\rangle_l$	$\langle A\rangle_m$	$\langle Z\rangle_l$	$\langle Z\rangle_m$
	(km s^{-1})		(Gyr)	(Gyr)		
(1)	(2)	(3)	(4)	(5)	(6)	(7)
N0173	73.01	5.99	10.28	15.47	0.027	0.023
N0628	55.14	6.39	5.33	11.98	0.037	0.028
U2124	139.24	4.98	10.49	15.34	0.029	0.028
N7490	140.92	5.53	17.11	19.19	0.028	0.028
N7495	96.87	8.61	6.57	14.13	0.011	0.032
N7610	67.60	12.57	7.13	14.15	0.016	0.040
N7741	12.17	13.61	3.30	14.41	0.011	0.041
I0239	61.24	11.80	4.45	12.71	0.041	0.038

Notes: Central galaxy parameters averaged within a radius of $r_e/10 \times 2$ arcsec (the slit width). Column (1): galaxy ID. Column (2): velocity dispersion within $r_e/10$. Column (3): velocity dispersion error within $r_e/10$. Column (4): average V-band light-weighted age within $r_e/10$. Column (5): average V-band mass-weighted age within $r_e/10$. Column (6): average V-band light-weighted metallicity within $r_e/10$. Column (7): average V-band mass-weighted metallicity within $r_e/10$.

derived in Fig. 11 and shown again as the black dotted line in Fig. 12, our slope is significantly steeper (we note, however, that our statistics are very low).

Comparison of the age–σ_0 relation (upper panel in Fig. 12), for each data set reveals a similar general trend of increasing age with σ_0. However, for the early-type sample of Thomas et al. (2005) (red open circles), the scatter in this trend is much larger. This can be easily explained in terms of the above-mentioned difference in our quoted ages; ours are true light-weighted *averages*, whereas those of Thomas et al. (2005) are SSP-equivalent values which are heavily weighted towards the most recent episode of SF and largely insensitive to any underlying old population (even though it may dominate the stellar mass). The same applies for the SSP-equivalent ages of the bulge samples of Morelli et al. (2008) (green open stars) and Ganda07 (light blue open triangles). However, Ganda07 also attempted to model their Lick indices in the context of an exponential SFH and derived the best-fitting e-folding time-scale, τ_{exp}. We converted τ_{exp} into an average age using equation (11) in MacArthur et al. (2004) and the results are shown in Fig. 12 as the solid blue triangles. Not only do these show much smaller scatter than their SSP-equivalent values, but they also follow a very similar trend as our average ages. Thus it seems that, when a reasonable attempt to sample the SFH of a galaxy is made, the trend of smaller ages with smaller σ_0 is much weaker and has significantly less scatter. We speculate that most of the scatter in the Thomas et al. (2005) and Morelli et al. (2008) samples would disappear if they were modelled in the context of a realistic SFH (as has been previously suggest for pure ellipticals in the 'frosting' models of e.g. Serra & Trager 2007).

All data sets again follow the same, and expected, trend of increasing metallicity with σ_0. The scatter is quite small at high velocity dispersion ($\sigma_0 \gtrsim 100\,\mathrm{km\,s^{-1}}$) but, for the SSP-equivalent estimates becomes quite large at smaller σ_0, again likely due to the fact that they are influenced by the stronger recent SF. On the other hand, our average values of Z follow the continuation of the Thomas et al. (2005) slope and our derived slopes are almost identical, despite the small overlap in the σ_0 range of our respective samples.

The magenta square in both panels of Fig. 12 represents our results for N0628 *but* using the $\langle A\rangle_l$ and $\langle Z\rangle_l$ measured at $\sim 1\,r_e$ (where the age peaks in our gradients, see Fig. 8). The purpose here is to compare with the MW 'outlier' in Thomas & Davies (2006; Fig. 4), as described in Section 1. The deviation (from the central value; see the black square at the same σ) is in the

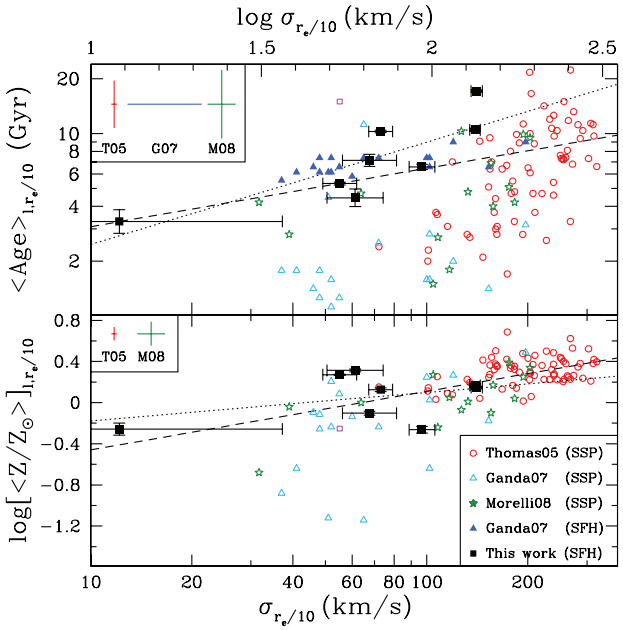

Figure 12. Average light-weighted age (top) and metallicity (bottom) as a function of the central velocity dispersion. Black solid squares: Our data in a $r_e/10$ aperture; these are the light-weighted values from the full population synthesis fits. Red open circles: The low-density environment ellipticals from Thomas et al. (2005) with ages measured from Lick indices and are light-weighted SSP values measured in apertures of $r_e/10$. Light blue open triangles: Ganda07 spirals (Sb–Sd) with ages and Z values in 1.5-arcsec apertures measured from Lick indices and are light-weighted SSP values. Dark blue solid triangles: Ganda07 spirals where here they used the Lick indices and modelled them with an exponential SFH to find the best e-folding time, τ (see their fig. 27), where we converted τ to $\langle A\rangle_l$ using equation (11) in MacArthur et al. 2004 (they do not give the best-fitting Z values for this method). Green open stars: Morelli et al. (2008) cluster S0 and spirals (S0–Sbc) with ages and Z values measured from Lick indices and are light-weighted SSP values. Magenta open square: Our results for N0628 *but* using the $\langle A\rangle_l$ and $\langle Z\rangle_l$ measured at $\sim$1 r_e (where the age peaks in our gradients). This is to compare with the MW 'outlier' in Thomas & Davies (2006), fig. 4. The deviation (from the central value; see square at same σ) is in the right-hand direction in both age and Z, but not quite as strong in Z to consider it a true 'outlier'. The black dashed lines are the best-fitting scaling relations for low-density environments derived in Thomas et al. (2005) based on MC simulations (which assume linear correlations of the parameters age, metallicity and α/Fe ratio with $\log\sigma$ and account for observational errors and intrinsic scatter in all three parameters). The black dotted lines are the same as in Fig. 11 and are least-squares fits to our light-weighted values (black squares). Error bars on all parameters for our data are shown on each point. The legend in the top left-hand corner of each panel shows the average errors on the samples from the literature, when provided (Ganda07 do not list errors on derived ages and Z values).

right-hand direction in age, i.e. if the age was determined at the bulge effective radius rather than at the galaxy centre, this galaxy would similarly stand out as an outlier in the age–σ_0 relation. We also see evidence of supersolar [α/Fe] at these radii in the $\langle$Fe$\rangle$–Mg b Lick index plane. The photometric (Zoccali et al. 2003) and spectroscopic (Rich & Origlia 2005; Zoccali et al. 2006) studies finding old and α-enhanced SPs of the MW bulge indeed sample a larger physical radius, outside of the plane, which is different from the 'central' values measured here for external galaxies. Thus, our observation of a positive age gradient, along with the observations of Peletier et al. (2007) of multicomponent (classical plus pseudo) bulges, the position of the MW can be readily understood and is not a major cause for concern. We further discuss the reliability of this result in Section 5.1.

Finally, also of particular note here is that between all three samples, a very large range in spheroid mass and type is covered; from pure ellipticals, through S0 bulges, 'classical' spiral bulges and to prototypical spiral 'pseudo-bulges'. However, in the context of the SP parameters as a function of the central galaxy potential, when a proper accounting of the spheroid's SFH is considered, there does not seem to be a break in the trends going from pure ellipticals to late-type bulges, nor is there a clear distinction between classical and pseudo-bulges.

5 DISCUSSION

This paper is the first to provide radially resolved spectra well into galaxy discs, enabling a comparison of the bulge and inner disc populations. While the small size of our sample does not allow for a detailed statistical study of galaxy parameters with inferred age and Z, we can still infer plausible SF mechanisms with a detailed look at each galaxy in the context of specific formation scenarios. The currently favoured scenarios for galaxy bulge formation can be summarized as follows.

'Classical' formation For the context of the following discussion, we consider 'classical' formation to imply that the bulges formed on a rapid time-scale, as is thought to be the case for pure ellipticals. There are two classes that fall into this heading as follows.

Monolithic collapse: Galaxies formed early through the gravitational collapse of a single cloud of primordial gas (e.g. Eggen, Lynden-Bell & Sandage 1962; Larson 1974; Carlberg 1984; Thomas et al. 1999). The relevant predictions from this model include:

(i) spheroids are metal-rich in centre and have a negative metallicity gradient;
(ii) spheroids are old and have shallow positive age gradients (centres slightly younger);
(iii) stellar abundance ratios of spheroids are supersolar [α/Fe] with positive gradients;
(iv) light profiles of spheroids have large Sérsic n values (i.e. high concentration);
(v) discs accrete on to an already formed spheroid and are thus younger.

Merging: Galaxies are gradually assembled in a hierarchical process through multiple mergers of smaller subgalactic units. This process begins at early times and continues to the current epoch (e.g. White & Rees 1978; Cole et al. 1994; Thomas et al. 1999; De Lucia et al. 2006).

Predictions for merger scenarios are clearly going to be much more complicated and depend on many different factors including the specific merger history of a given galaxy, the mass and gas content of the infalling clumps at the time of merging, and the specific physics describing the SF as a result of the merger and the overall shape of the merger product. In particular, predictions about SPs of galaxies, particularly those of multiple component (bulge, disc, bar), are still in their infancy and must currently resort to semi-analytical recipes to describe many of the complicated gastrophysical processes that remain poorly understood and too difficult to model explicitly. However, certain global predictions based on cosmologically motivated merger trees are robust and include:

(i) a galaxy mass–metallicity relationship (more massive galaxies have higher Z);

(ii) early mergers will have supersolar [α/Fe], but more recent merging leads to solar [α/Fe] with flat profiles;

(iii) less massive spheroids have more extended SFHs leading to positive correlations of σ_0 with average age, Z and [α/Fe].

In the above two scenarios, the formed spheroid is considered a 'bulge' if it happens to have formed a disc around it and/or if the disc component of a progenitor galaxy survived the merger event. Otherwise, the spheroid is considered a pure elliptical galaxy.

Secular evolution

In the secular scenario, galaxy bulges formed through a secular redistribution of material from the disc (e.g. Kormendy & Kennicutt 2004, and references therein).

The predictions of SP parameters and their gradients in the context of secular evolution are also complicated and remain in their infancy. A major contributor to the uncertainties involves the inclusion of gas in the simulations leading to very different results for dissipational versus dissipationless evolution. Furthermore, processes that fall under the guise of secular evolution can occur over a wide range of time-scales depending on bar presence/strength, spiral arm strength, triaxiality of DM halo, etc.

The more tractable predictions include:

(i) dissipationless evolution rearranges disc stars into a bulge component, thus both components would have the same SP parameters;

(ii) dissipational evolution will result in fresh SF in the centre leading to bulges containing young stars.

5.1 Notes on individual galaxies

In the context of the above bulge formation scenarios and their predictions for bulges properties, we now review each of our eight galaxies individually. In Table 6 we provide a summary of the formation scenarios indicated by all of our observations.

N0173: The SP populations in the bulge region of this Sc galaxy reveal an old and metal-rich centre with gradients to younger ages and smaller Z within 1 r_e, consistent with the 'classical' monolithic picture of bulge formation. The disc is somewhat younger with virtually no gradient in age, but a mild gradient to smaller Z, out to $\sim 2r_d$. The SFH in Fig. 7 reveals roughly equal contributions in light (normalized to the V band) of an old ($\sim$13 Gyr) subsolar ($Z = 0.004$) population plus a young (1-Gyr) metal-rich ($Z = 0.05$) population within $\sim$1 r_e. More recent metal-poor SF (possibly from accretion of unenriched gas) is evident in the outer region around 1 r_e. Throughout, the old population is entirely dominant in mass (right-hand plot in Fig. 7). There is evidence for slightly enhanced [α/Fe] in the centre (Fig. 4), pointing to short SF time-scales. This galaxy lies in the 'ambiguous' region of the ($V_{\max,r_e}/\sigma_0$, ϵ) plane in Fig. 10, but in general seems consistent with a classical *monolithic* bulge formation scenario.

N0628: The prototypical grand-design Sc galaxy. Here the inner bulge is quite young and metal-rich, consistent with recent central SF, possibly due to secular funnelling of gas to the central regions. There is no sign of a bar component in this galaxy, but this does not rule out secular processes from, for example, a pre-existing bar or the strong spiral structure. The strong spiral dust lanes on the concave side of the arms are indicative of shocks from the pile-up of gas when entering the spiral density wave (e.g. Kormendy & Kennicutt 2004). The gas loses energy at the shock front and sinks to the centre resulting in central SF. This process occurs on much longer time-scales than the action of a bar, but if the spiral structure is strong (high pitch angle), such a process will contribute to the building of a central component.

As with N0173, we also see a light-dominant high-Z 1-Gyr component on top of an old SP. Here, the young component has more weight by light and mass in the centre, such that up to $\sim$40 per cent of the mass in the central regions was contributed by the SF episode that occurred 1 Gyr ago. At increasing radii, we see stronger contribution from much younger and metal-poor SSPs. This is indicative of accretion of unenriched material on to the disc. However, the main contributor by mass out to $\sim 1r_d$ is still from an old component. One side of our slit is consistent with a disc age gradient toward younger ages with increasing radius, consistent with inside-out formation. However, there are spikes to old ages and the other side of the slit is more consistently at old ages. This is likely due to arm–interarm crossings, where the older regions coincide with an interarm region where only the underlying oldest SPs are present.

Of particular note is the spike to older ages just beyond $\sim$1 r_e for NGC 628. This is precisely the signature noted in Section 1 required to reconcile the discrepant results for the MW bulge. The fact that we observe this signature on both sides of the galaxy (whose spectra were fitted independently) renders confidence that

Table 6. Summary of 'secular/pseudo' (S) versus 'classical' (C) indicators for each galaxy.

Name (1)	Sérsic n (2)	Bar (3)	Young SP (4)	Old SP (5)	d$\langle A\rangle$/dr (6)	d$\langle Z\rangle$/dr (7)	V/σ_0 (8)	α/Fe (9)	Overall type (10)
N0173	S/C		S	C	C	C	C	C	C
N0628	S		S	C	S/C	S/C	S	S	S
U2124	S/C	S	S	C	S/C	S/C	C	C	C/S
N7490	S/C		S	C	C/S	S/C	S/C	S/C	C/S
N7495	C		S	C	S/C	S/C	S	S	S/C
N7610	S		S	C	C/S	C/S	C	S	S/C
N7741	S	S	S	C	S/C	S/C	S	S	S
I0239	S		S	C	S/C	S/C	S/C	S/C	S/C

Notes: Column (1): galaxy ID. Column (2): the dividing line in at $n \simeq 2$. Column (3): if a bar is clearly present. Column (4): significant presence of recent SF (within the last $\sim$1–2 Gyr). Column (5): significant presence of very old SP ($\gtrsim$13 Gyr). Column (6): indication from SP age gradient. Column (7): indication from SP Z gradient. Column (8): indication from kinematics (support from rotation versus random motions). Column (9): SF time-scale implied by central abundance ratio (as inferred from the results of Fig. 4), whereby enhanced α/Fe implies a short formation time-scale (as the Fe elements produced by type I supernovae have not had time to enrich the gas in Fe before cessation of SF). Column (10): overall impression.

this signature is real. Additionally, using SAURON observations, Ganda07 observed the same trend in age for NGC 628 using a fully independent approach. In fact, this trend was first implied by the UV colour gradients presented in Cornett et al. (1994), from which they inferred that the SFH of this galaxy varies significantly as a function of radius. Ganda et al. (2006) demonstrated that the stellar kinematics are characterized by slow projected rotation, and a mild central dip in the velocity dispersion profile, indicating a cold central region, which could be identified as an inner disc. Our velocity dispersion profile agrees very well with theirs, as shown by the red lines in the top panel of the top right-hand plot in Fig. 9.

As mentioned above, images reveal clear spiral dust lanes throughout the disc of this galaxy. From the bottom panel in the top right-hand plot in Fig. 8 we see that indeed, our fits indicate the presence of modest amounts of dust at various radii.

In all, there seems to be a significant contribution from secular processes to the growth of this bulge.

U2124: This is our earliest type, strongly barred, spiral, SB(r)a; our slit was aligned along the bar. Both the light- and mass-weighted age profiles are very similar; quite flat at old ages and supersolar Z within $1\,r_e$. The flat profiles could be interpreted in the context of redistribution of material due to the bar. However, the small weight of the younger SPs indicates that perhaps the gas supply is feeble such that only a small amount of SF is triggered by the bar action. There is no evidence for dust extinction in the spectra, which is also consistent with no recent SF and little gas content. There is also a clear gradient in Z beyond $1\,r_e$ which would be consistent with a bulge formation scenario similar to ellipticals (i.e. early and short time-scale of SF, also indicated by the supersolar [α/Fe] in Fig. 4). Unfortunately, our data do not extend past the bar radius ($\sim$21 arcsec), so we cannot examine the disc profile.

The SFH indicates a dominant old population that is a mixture of a 13 Gyr $Z = 0.004$ SSP and a $\sim$16 Gyr solar/supersolar SSP. On top of this, within $\sim 1\,r_e$ is a metal-rich 1-Gyr population extending all the way into the centre. This young population contributes $\sim$50 per cent in V-band light-weight, but only of the order of 5 per cent to the total stellar mass.

In all, this bulge shows many classical formation features alongside pseudo-bulge-type structures, thus likely is composed of a mixture of both bulge types.

N7490: This is a normal Sbc galaxy. The spectra are quite red in the centre with weak emission seen in [N II], and a general bluing to larger radii. The age profile reveals a very old $\sim$solar Z centre with a strong gradient to younger ages out to $\sim 1\,r_e$ and a weaker gradient in the disc to young ages out to $\sim 2\,r_d$, but with a flat-to-increasing Z within $1\,r_e$ and decreasing in the disc. These inner SP gradients are somewhat ambiguous in terms of their implication for the formation of the bulge, but the profiles are generally consistent with a merger scenario for the bulge with subsequent inside-out disc formation.

The SFH reveals that the central $\sim 1/2\,r_e$ is entirely dominated (in mass and light) by an old solar metallicity SSP, and this is the only galaxy in our sample that has almost no contribution from a younger SP in the very central region (to $\sim 1/2\,r_e$). It also has the highest σ_0 of the sample. This would also be consistent with formation by mergers at early times and/or the merger of gas-poor subcomponents for the bulge component. This is further indicated by the supersolar abundance ratio in the centre in Fig. 4 as well as the strong features in the fit residuals in Fig. 3 similar to those shown in Fig. 5. Beyond $\sim 1/2\,r_e$, there is a slightly younger ($\sim$10 Gyr) and more metal-poor population which is likely the accretion of a disc after the initial bulge collapse. The SFH also reveals a SF episode 1 Gyr ago in a ring with a radius of about $1\,r_e$, where we also see the ages dip to lower values and Z to slightly higher. Such an episode of recent, enhanced, SF in a ring at $1\,r_e$ is a secular process. We also see from Fig. 8 that there is little to no dust in the central regions, but significant a 'spike' at $\sim 1\,r_d$ associated with the very young SSP contributing significantly to the light in this region.

This bulge is most consistent with having formed 'classically' via mergers at early times with subsequent disc accretion, with a minor, more recent, secular contribution in the form of a ring of SF.

N7495: This SABc galaxy has strong emission throughout, being strongest at the very centre (Fig. A1). The current SF dominates the light, but is entirely insignificant by mass ($\sim$1–2 per cent), leaving an old and metal-rich population dominant by mass out to $\sim 1\,r_d$. There is a significant amount of dust out to $\sim 1\,r_e$, again associated with the current SF.

The age profile in the bulge is a bit erratic, jumping from old to young and back to old within $1\,r_e$, while Z shows a consistent rise in this region. The disc profiles are both very flat and have significant contributions to the light of a very young and metal-poor SP. Significant amounts of dust throughout are evident, again in conjunction with the fresh SF. In mass-weight, however, the disc is consistently very old and metal-rich. This is difficult to interpret in terms of an inside-out scenario, but given the current level of SF throughout, this disc is still in formation.

There is some evidence of recurrent episodes of SF in the very central regions; one contributing $\sim$30 per cent by mass 10 Gyr ago and a less massive event ($\sim$1 per cent) at 0.4 Gyr; given the stochastic sampling of our SFHs, this could be interpreted as a more extended SFH.

The kinematics reveal a sharp decline in the velocity dispersion from $\sim 100\,\mathrm{km\,s^{-1}}$ at the centre, to $\lesssim 20\,\mathrm{km\,s^{-1}}$ by $1\,r_e$. Its position in the V/σ_0 diagram (Fig. 10) reveals a significant amount of support against collapse from rotation, implying a discy origin, whereas the bulge profile shape has our highest value of the Sérsic n shape parameter, pointing to a more classical bulge.

Again, there seems to be contributions from both classical and secular components to the formation history of the bulge of this galaxy.

N7610: This galaxy is our latest type class, Scd. There is significant SF in the centre of this galaxy. The bulge light profile is characterized by a Sérsic $n = 0.8$, highly suggestive of a discy origin. The SP profiles are flat within the bulge region with a mild trend to younger and more metal-rich inward (which is consistent with rapid *E-like* formation). Again, the old population represents the bulk of the mass, but there is significant recent subsolar SF (ages 0.001–1 Gyr). Our data do not extend far enough to asses the disc profile, but they appear relatively flat out to several bulge radii. Small levels of dust are seen coincident with the regions of strong current SF.

The kinematics reveal a sharp decline in the velocity dispersion from $\sim 70\,\mathrm{km\,s^{-1}}$ at the centre, to $\lesssim 10\,\mathrm{km\,s^{-1}}$ by $1\,r_e$. Its position in the V/σ_0 diagram in Fig. 10 is below the oblate line, but not far enough to place it unambiguously as occupying the E-type location of the plot.

There is evidence for contributions from both classical and secular components to the formation history of the bulge of this galaxy.

N7741: This is our only other strongly barred galaxy and our latest type, SB(s)cd. The light-weighted bulge is very young with subsolar metallicity, but in mass-weight is old and metal-rich. The recent central SF indicated by the light-weighted values could be a result of in-funnelling of fresh gas due to the bar. Our slit is aligned perpendicular to the bar, thus no flattening of gradients would necessarily be expected. The disc profile is generally young and solar Z with close to flat profiles.

While there are clear secular processes contributing to the central growth of this galaxy, the overwhelming dominance by mass is that of a very old and metal-rich whose gradients are consistent with a classical picture.

I0239: An SAB(rs)cd galaxy that also shows a significant population of 1-Gyr metal-rich stars on top of an old metal-rich population. In this case both contribute significantly to the stellar mass. The age gradient in the bulge region is relatively flat out to $\sim 1\, r_{\rm d}$, while the Z profile is decreasing. Disc gradients are generally flat to mildly decreasing. There is an indication of slightly supersolar [α/Fe] (Fig. 4), indicative of rapid formation, while the Sérsic $n = 0.9$ light profile suggests a discy origin.

Once again, this bulge displays a mix of classical and secular evolutionary processes.

6 SUMMARY

Using radially resolved long-slit spectra of eight star-forming spiral galaxies, we have performed a detailed analysis of their SP and kinematic profiles and provide interpretations based on currently favoured formation scenarios. Central correlations in ages and metallicities with velocity dispersion are compared to other studies of bulges and pure elliptical galaxies.

The most pertinent observations are as follows.

Fitting techniques

(i) With moderate spectral resolution, good λ coverage, and high S/N/Å ($\geq$50), measurement of light-weighted average ages and metallicities for star-forming galaxies is feasible.

(ii) Details are critical: calibration (λ and relative flux), resolution, velocity dispersion and rotation must be treated self-consistently between the data and models.

(iii) Different fitting techniques weigh age, metallicity and abundance ratios differently: Balmer emission limits age fitting from indices; age information is recovered (in the presence of emission) from full spectrum and continuum SED fitting (but compounds the caveats about dust extinction and fluxing that are less important for indices).

(iv) SSPs are not a good match to late-type galaxies. The degeneracies between age, metallicity, dust, etc., are extreme leading to unstable fits.

(v) Full population synthesis is the only method to provide reliable and consistent results, and is thus the method of choice for the establishment of light and/or mass-weighted average ages and metallicities of late-type galaxies.

Stellar populations of bulges and inner discs

(i) In a mass-weighted context, all bulges are predominantly composed of old and metal-rich SPs ($\gtrsim$ 80 per cent by mass).

(ii) Some contribution to bulge growth by secular evolution is clearly evident in most late-type bulges, with SPs of 0.001–1 Gyr contributing as much as 70 per cent to the optical light. The corresponding contribution to the bulge mass, however, is generally small ($\sim$20 per cent by mass or less).

(iii) Spiral bulges display a wide variety of age and metallicity gradients (from negative to positive) in the bulge region, allowing for a range in formation mechanisms.

(iv) The observation of positive age gradients within the effective radius of some late-type bulges helps reconcile the long-standing discrepancy of the secular-like kinematics and light profile shape (including the presence of a bar) with 'classical'-like old and α-element enhanced SPs observed in the MW bulge as being due to SP sampling at different physical locations in the bulges.

(v) Spiral discs show mildly decreasing to flat profiles in both age and metallicity, generally consistent with inside-out formation.

(vi) Bulges follow the correlations of increasing light-weighted age and Z with central velocity dispersion as for elliptical galaxies and early-type bulges found in other studies, but when an SFH more complex and realistic than an SSP-equivalent is taken into account, the trend is shallower and its scatter is much reduced.

The implication seems to be that bulge formation has been dominated by processes that are common to all spheroids, whether or not they currently reside in discs. Monolithic collapse cannot be ruled out in all cases, but merging must be invoked for most of our spiral bulges. The process of formation occurs on shorter time-scales for spheroids with the highest central velocity dispersions, and the relative contribution to the stellar mass budget in bulges via secular processes or 'rejuvenated' star formation is small, but generally increases in weight with decreasing σ_0.

Ultimately, we desire a large enough sample to solidify the conclusions inferred in this analysis and to assess any trends with galaxy parameters, but already these results provide important clues for bulge formation scenarios and restrictions for future implementations of galaxy formation models.

ACKNOWLEDGMENTS

We wish to thank Roberto Cid Fernandes, Stéphane Charlot, Claudia Maraston, Richard Ellis and Tommaso Treu for stimulating discussions. Thanks also to the anonymous referee for useful comments that led to valuable improvements to the paper. We also owe a huge debt of gratitude to the Gemini staff, Stéphanie Côté, Inger Jørgensen and Jean-René Roy in particular, for their instrumental contribution to the preparation and execution of our queue-mode observations. LAM acknowledges financial support from the National Science and Engineering Council of Canada (NSERC). SC acknowledges financial support through a Discover Grant from the NSERC. This research has made use of the NED which is operated by the Jet Propulsion Laboratory, California Institute of Technology, under contract with the National Aeronautics and Space Administration. Based on observations obtained at the Gemini Observatory, which is operated by the Association of Universities for Research in Astronomy, Inc., under a cooperative agreement with the NSF on behalf of the Gemini partnership: the National Science Foundation (United States), the Science and Technology Facilities Council (United Kingdom), the National Research Council (Canada), CONICYT (Chile), the Australian Research Council (Australia), Ministério da Ciência e Tecnologia (Brazil) and Ministerio de Ciencia, Tecnología e Innovación Productiva (Argentina).

REFERENCES

Bartholomew-Biggs M. C., 1989, OPTIMA Manual. Numerical Optimisation Center, Univ. Hertfordshire

Bell E. F., Baugh C. M., Cole S., Frenk C. S., Lacey C. G., 2003, MNRAS, 343, 367

Binney J., Tremaine S., 1987, Galactic Dynamics. Princeton Univ. Press, Princeton, NJ, p. 747

Bruzual A. G., Charlot S., 2003, MNRAS, 344, 1000 (BC03)

Byrd R. H., Lu P., Nocedat J., Zhu C., 1995, SIAM J. Sci. Comput., 16, 1190

Caldwell N., Rose J. A., Concannon K. D., 2003, AJ, 125, 2891

Cardiel N., Gorjas J., Cenaro J., González J. J., 1998, A&AS, 127, 597

Carlberg R. G., 1984, ApJ, 286, 403
Chabrier G., 2003, PASP, 115, 763
Charlot S., Fall S. M., 2000, ApJ, 539, 718 (CF00)
Cid Fernandes R., 2006, Bol. Asoc. Argentina Astron., 49, 228
Coelho P., Barbuy B., Meléndez J., Schiavon R. P., Castilho B. V., 2005, A&A, 443, 735
Coelho P., Bruzual G., Charlot S., Weiss A., Barbuy B., Ferguson J. W., 2007, MNRAS, 382, 498
Cohen J. G., Blakeslee J. P., Ryzhov A., 1998, ApJ, 496, 808
Cole S., Aragon-Salamanca A., Frenk C. S., Navarro J. F., Zepf S. E., 1994, MNRAS, 271, 781
Conn A. R., Gould N. I. M., Toint Ph. L., 1992, LANCELOT; a FORTRAN Package for Large-Scale Nonlinear Optimization. Springer Series in Computational Mathematics, Vol. 17. Springer-Verlag, Heidelberg
Cornett R. H. et al., 1994, ApJ, 426, 553
Courteau S., de Jong R. S., Broeils A. H., 1996, ApJ, 457, L73
de Jong R. S., 1996, A&A, 313, 45
De Lucia G., Springel V., White S. D. M., Croton D., Kauffmann G., 2006, MNRAS, 366, 499
de Zeeuw P. T. et al., 2002, MNRAS, 329, 513
Driver S. P., Popescu C. C., Tuffs R. J., Liske J., Graham A. W., Allen P. D., de Propris R., 2007, MNRAS, 379, 1022
Dutton A. A., van den Bosch F. C., Dekel A., Courteau S., 2007, ApJ, 654, 27
Eggen O. J., Lynden-Bell D., Sandage A. R., 1962, ApJ, 136, 748
Fisher D. B., Drory N., 2008, AJ, 136, 773
Ganda K., Falcón-Barroso J., Peletier R. F., Cappellari M., Emsellem E., McDermid R. M., de Zeeuw P. T., Carollo C. M., 2006, MNRAS, 367, 46
Ganda K. et al., 2007, MNRAS, 380, 506 (Ganda07)
González J. J., 1993, PhD thesis, Univ. California, Santa Cruz
Gorgas J., Faber S. M., Burstein D., Gonzalez J. J., Courteau S., Prosser C., 1993, ApJS, 86, 153
Goudfrooij P., Gorgas J., Jablonka P., 1999, Ap&SS, 269, 109
Graham A., 2001, AJ, 121, 820
Hao L. et al., 2005, AJ, 129, 1783
Heavens A. F., Jimenez R., Lahav O., 2000, MNRAS, 317, 965
Henry R. B. C., Worthey G., 1999, PASP, 111, 919
Hernandez X., Valls-Gabaud D., 2008, MNRAS, 383, 1603
Hook I. M., Jørgensen I., Allington-Smith J. R., Davies R. L., Metcalfe N., Murowinski R. G., Crampton D., 2004, PASP, 116, 425
Jablonka P., Gorgas J., Goudfrooij P., 2007, A&A, 474, 763
Jacoby G. H., Hunter D. A., Christian C. A., 1984, ApJS, 56, 257
James P. A., Prescott M., Baldry I. K., 2008, A&A, 484, 703
Kaufmann T., Mayer L., Wadsley J., Stadel J., Moore B., 2007, MNRAS, 375, 53
Kennicutt R. C., Jr, 1983, ApJ, 272, 54
Koleva M., Prugniel P., Ocvirk P., Le Borgne D., Soubiran C., 2008, MNRAS, 385, 1998
Kormendy J., 1982, in Martinet L., Mayor M., eds, Morphology and Dynamics of Galaxies, Twelfth Advanced Course of the Swiss Society of Astronomy and Astrophysics. Geneva Observatory, Sauverny, Switzerland, p. 113
Kormendy J., Kennicutt R. C., Jr, 2004, ARA&A, 42, 603
Larson R. B., 1974, MNRAS, 166, 585
Le Borgne D., Rocca-Volmerange B., Prugniel P., Lançon A., Fioc M., Soubiran C., 2004, A&A, 425, 881
Le Borgne J.-F. et al., 2003, A&A, 402, 433
López-Corredoira M., Cabrera-Lavers A., Mahoney T. J., Hammersley P. L., Garzón F., González-Fernández C., 2007, AJ, 133, 154
MacArthur L. A., 2005, ApJ, 623, 795
MacArthur L. A., Courteau S., Holtzman J. A., 2003, ApJ, 582, 689 (Mac03)
MacArthur L. A., Courteau S., Bell E., Holtzman J. A., 2004, ApJS, 152, 175
MacArthur L. A., Ellis R. S., Treu T. U. V., Bundy K., Moran S., 2008, ApJ, 680, 70
Maraston C., 2005, MNRAS, 362, 799
Moore B., Ghigna S., Governato F., Lake G., Quinn T., Stadel J., Tozzi P., 1999, ApJ, 524, L19
Moorthy B. K., Holtzman J. A., 2006, MNRAS, 371, 583
Morelli L. et al., 2008, MNRAS, 389, 341
Moultaka J., Ilovaisky S. A., Prugniel P., Soubiran C., 2004, PASP, 116, 693
Navarro J. F., Steinmetz M., 2000, ApJ, 528, 607
Nilson P., 1973, Uppsala General Catalogue of Galaxies. Nova Acta Regiae Soc. Sci. Upsaliensis Astronomiska Observatorium, Uppsala
Osterbrock D. E., 1989, Astrophysics of Gaseous Nebulae and Active Galactic Nuclei. Univ. Science Books, Mill Valley, CA
Osterbrock D. E., Ferland G. J., 2006, in Osterbrock D. E., Ferland G. J., eds, Astrophysics of Gaseous Nebulae and Active Galactic Nuclei, 2nd edn. University Science Books, Sausalito, CA
Panter B., Jimenez R., Heavens A. F., Charlot S., 2007, MNRAS, 378, 1550
Peletier R. F. et al., 2007, MNRAS, 379, 445
Pickles A. J., 1985, ApJ, 296, 340
Primack J. R., 2007, Nucl. Phys. B, 173, 1
Proctor R. N., Sansom A. E., 2002, MNRAS, 333, 517 (PS02)
Puzia T. H., Kissler-Patig M., Thomas D., Maraston C., Saglia R. P., Bender R., Goudfrooij P., Hempel M., 2005, A&A, 439, 997
Rich R. M., Origlia L., 2005, ApJ, 634, 1293
Sarzi M. et al., 2006, MNRAS, 366, 1151
Schiavon R. P., 2007, ApJS, 171, 146
Schlegel D. J., Finkbeiner D. P., Davis M., 1998, ApJ, 500, 525
Serra P., Trager S. C., 2007, MNRAS, 374, 769
Thomas D., Davies R. L., 2006, MNRAS, 366, 510
Thomas D., Greggio L., Bender R., 1999, MNRAS, 302, 537
Thomas D., Maraston C., Bender R., 2003, MNRAS, 339, 897
Thomas D., Maraston C., Korn A., 2004, MNRAS, 351, L19
Thomas D., Maraston C., Bender R., Mendes de Oliveira C., 2005, ApJ, 621, 673
Tojeiro R., Heavens A. F., Jimenez R., Panter B., 2007, MNRAS, 381, 1252
Trager S. C., Worthey G., Faber S. M., Burstein D., González J. J., 1998, ApJS, 116, 1
Trager S. C., Dalcanton J. J., Weiner B. J., 1999, The Formation of Galactic Bulges. Cambridge Univ. Press, Cambridge, p. 42
Trager S. C., Faber S. M., Worthey G., González J. J., 2000, AJ, 120, 165
Trager S. C., Faber S. M., Dressler A., 2008, MNRAS, 386, 715
Vazdekis A., 1999, ApJ, 513, 224
Wallace L., Hinkle K., Livingston W., 1998, An Atlas of the Spectrum of the Solar Photosphere from 13,500 to 28,000 cm^{-1} (3570 to 7405 Å). National Optical Astronomy Observatories, Tucson, AZ
White S. D. M., Rees M. J., 1978, MNRAS, 183, 341
Worthey G., 1994, ApJS, 95, 107
Worthey G., Ottaviani D. L., 1997, ApJS, 111, 377
Worthey G., Faber S. M., González J. J., Burstein D., 1994, ApJS, 94, 687
Zhu C., Byrd R. H., Lu P., Nocedal J., 1994, L-BFGS-B: FORTRAN Subroutines for Large Scale Bound Constrained Optimization, Technical Report, NAM-11. EECS Department, Northwestern University
Zhu C., Byrd R. H., Nocedal J., 1997, L-BFGS-B: Algorithm 778: L-BFGS-B, FORTRAN Routines for Large Scale Bound Constrained Optimization, ACM Transactions on Mathematical Software, 23, p. 550
Zoccali M. et al., 2003, A&A, 399, 931
Zoccali M. et al., 2006, A&A, 457, L1

APPENDIX A: 1D SPECTRA

In Fig. A1 we present the fully calibrated and velocity (redshift + rotation) subtracted spectra at a number of radii for each galaxy. The spectra are plotted on a logarithmic scale and adjusted with an arbitrary constant to offset the spectra from each other. Only one side of the slit is shown, and not all radial bins are plotted for the well-sampled galaxies, but the $r = 0$ and last two bins are always plotted. The spectra were co-added (radially) to a minimum S/N/Å ≥ 50 measured in the 5050–5450 Å wavelength interval (selected to avoid prominent emission lines such as [O III] λλ5007, 4959,

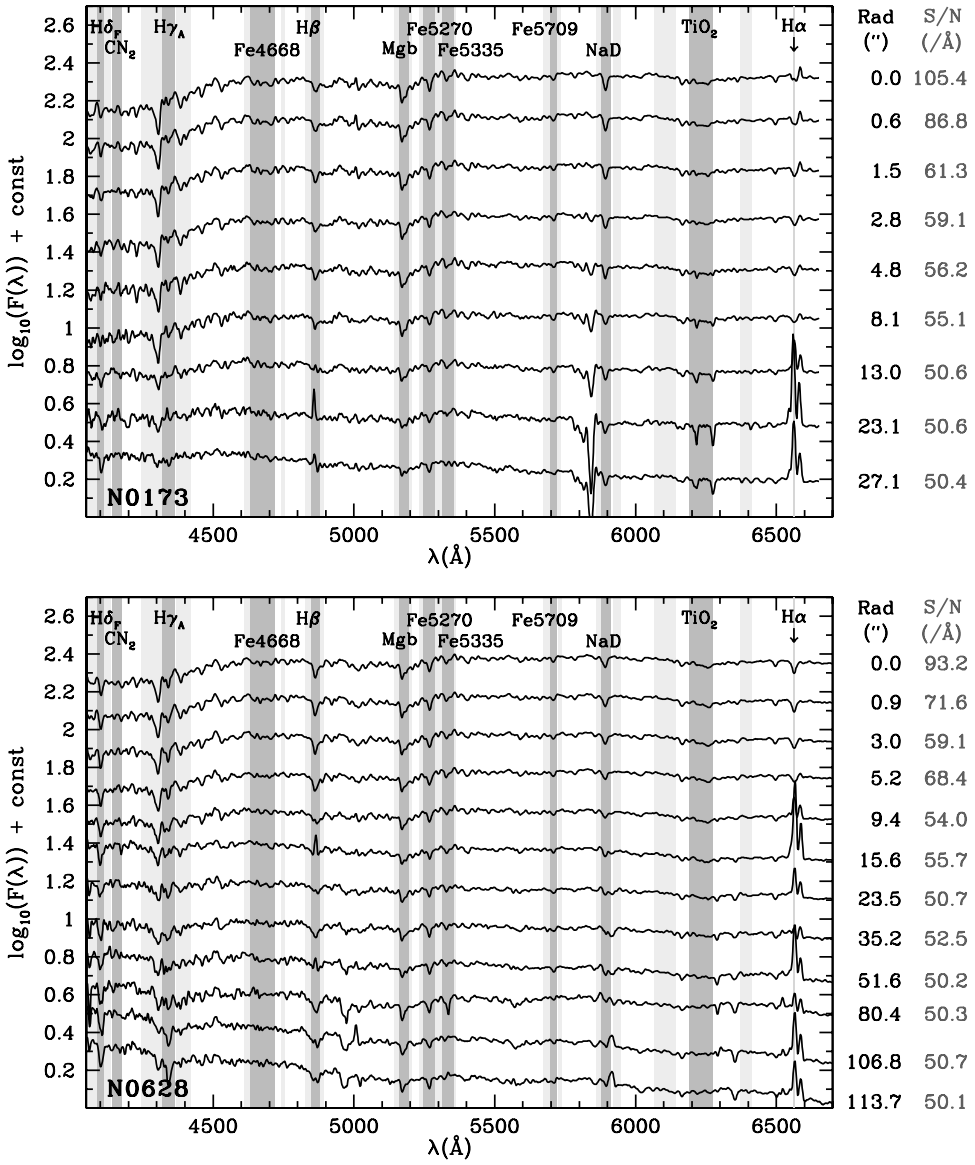

Figure A1. Spectra as a function of radius for all galaxies. The spectra were co-added (radially) to a minimum S/N/Å of 50. Not all radial bins are shown, but the first bin and last two bins are always plotted. The light-weighted radius and the spectrum's corresponding S/N are labelled at the edge of the plot. Many of the Lick indices are marked as vertical shading – darker shading delineates the central passband and lighter shading the pseudo-continua. The location of Hα, often seen in emission, is also indicated.

Hα λ6563, [N II] $\lambda\lambda$6583, 6548 and the [O I] sky line at λ5577). The minimum S/N/Å of 50 was selected as a compromise between accurate age and metallicity determinations, and sufficient radial extent for gradient measurements. The light-weighted radius and the spectrum's corresponding S/N/Å are labelled at the right-hand edge of each panel (note that the $r = 0$ arcsec bin is in reality closer to $r = 0.04$ arcsec due to our binning of 0.2 arcsec pixel^{-1} and assuming a Gaussian light profile in the galaxy centre). Many of the Lick indices (see Section B2) are marked as vertical shaded lines – dark grey delineates the central passband and light grey the pseudo-continua.

A number of pertinent observations can be made from a visual examination of the spectra.

(i) Improper subtraction of prominent sky emission lines (falling in and around the NaD and TiO indices) is evident at the largest radial bins for all galaxies.

(ii) There is a significant overall bluing of the SED with radius for most galaxies. The two notable exceptions are N7741 and I0239. The former shows significant emission in Hα, Hβ and Hγ_A (the latter two appearing as fill-in to the underlying absorption line), and at [N II] $\lambda\lambda$6583, 6548 and [O III] λ5007 in the central spectrum, which could mask an underlying redder stellar SED. N7495 and N7610 also show significant central emission and bluer SEDs compared to those galaxies with less obvious central emission (e.g. N0628 and U2124), but a significant (further) radial bluing is still evident.

(iii) For some galaxies with significant emission in the Hα + [N II] region, an emission spike superimposed on an underlying absorption can be seen in the other Balmer lines (most noticeably in Hβ, but a spike can be seen even in Hγ and Hδ in extreme cases, e.g. N7495 and N7741). Given that the Balmer lines are the most sensitive age indicators in the Lick index system, it is likely that index-based age estimates of the underlying SP will be difficult to constrain in these galaxies. In the full spectrum fits, these emission

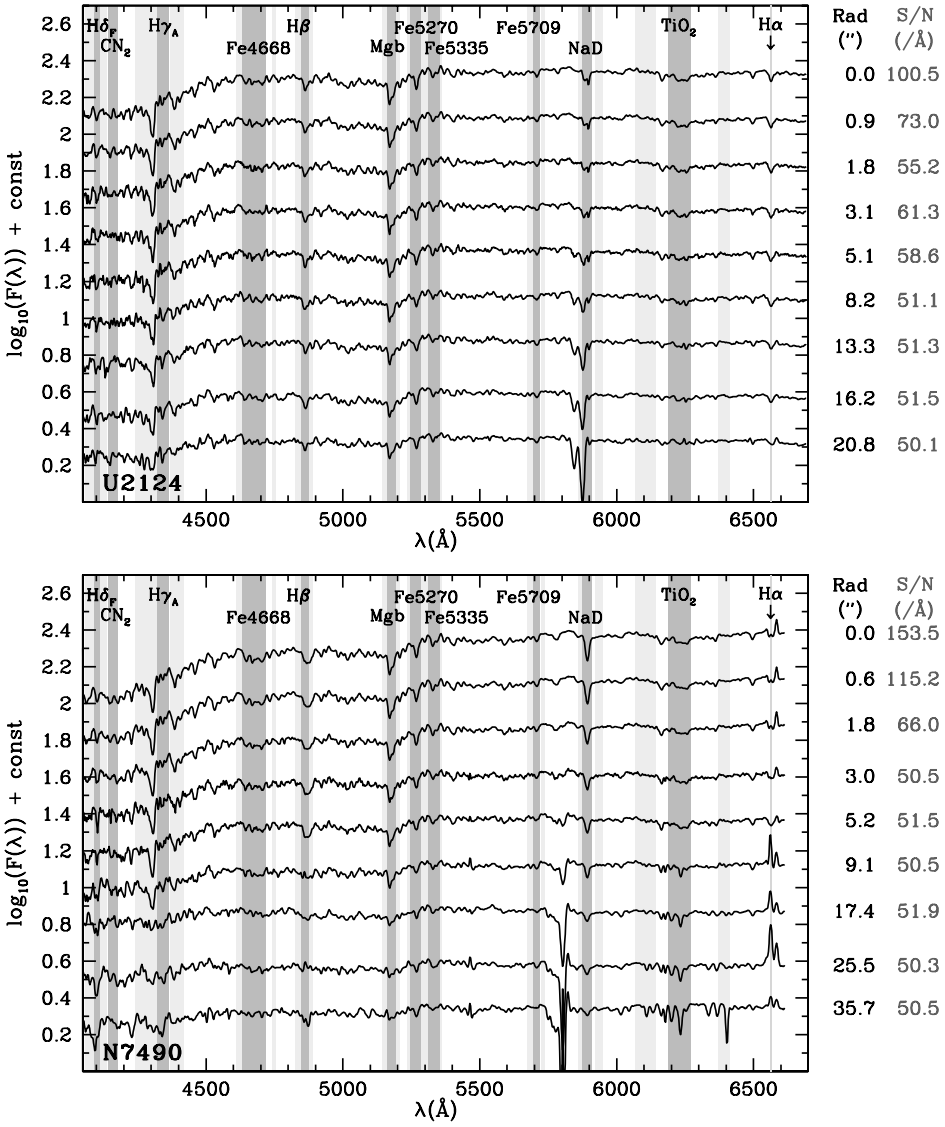

Figure A1 – *continued*

lines will need to be masked out as emission lines are not included in the BC03 models.

The most likely source of the emission is due to normal, but intense, current star formation. We can rule out significant contributions from AGN as the source of emission based on the low [N II] λ6583/Hα and [O III] λ5007/Hβ emission line ratios (see e.g. Hao et al. 2005), but small contributions in our most severe cases, N7495, N7610 and especially N7741, cannot be entirely ruled out (but these would be restricted to Seyfert 2 or LINER AGN as the broad lines characteristic of Seyfert 1 spectra are not seen).

(iv) Clear radial variations in many Balmer and metal-line absorption-line strengths can be seen in many of our galaxies. The interpretation of these gradients in terms of age and metallicity require an implementation of one of the fitting techniques described below in Appendix B.

APPENDIX B: AGE AND METALLICITY FITS

Several methods exist to assign an age and metallicity to an observed integrated galaxy spectrum. Each technique has its own advantages and drawbacks depending on the application. One of the fundamental challenges any successful method must overcome is the inherent degeneracy in SPs between old age, high metallicity and dust content, all leading to redder SEDs. Further difficulties can come from non-stellar sources that are not included in the SP models, such as emission lines from H II regions, and contributions from a central AGN. Below we consider three methods for deriving the SP parameters from our long-slit spectra of star-forming spiral galaxies: (i) the Lick/IDS index system; (ii) SSP fits to the entire spectrum and (iii) full synthesis fits to the entire spectrum. The latter two also include a prescription for dust extinction. In the following, after discussing the importance of understanding the resolution of both the data and models when making comparisons, we describe the first two methods individually and then compare their results with each other and with those obtained from the full population synthesis fits in Section 3.

B1 Resolution and velocity dispersion effects

In order to compare the data to the models, potential resolution effects must be accounted for. In the case where the models have higher resolution than the data, this can be accomplished by

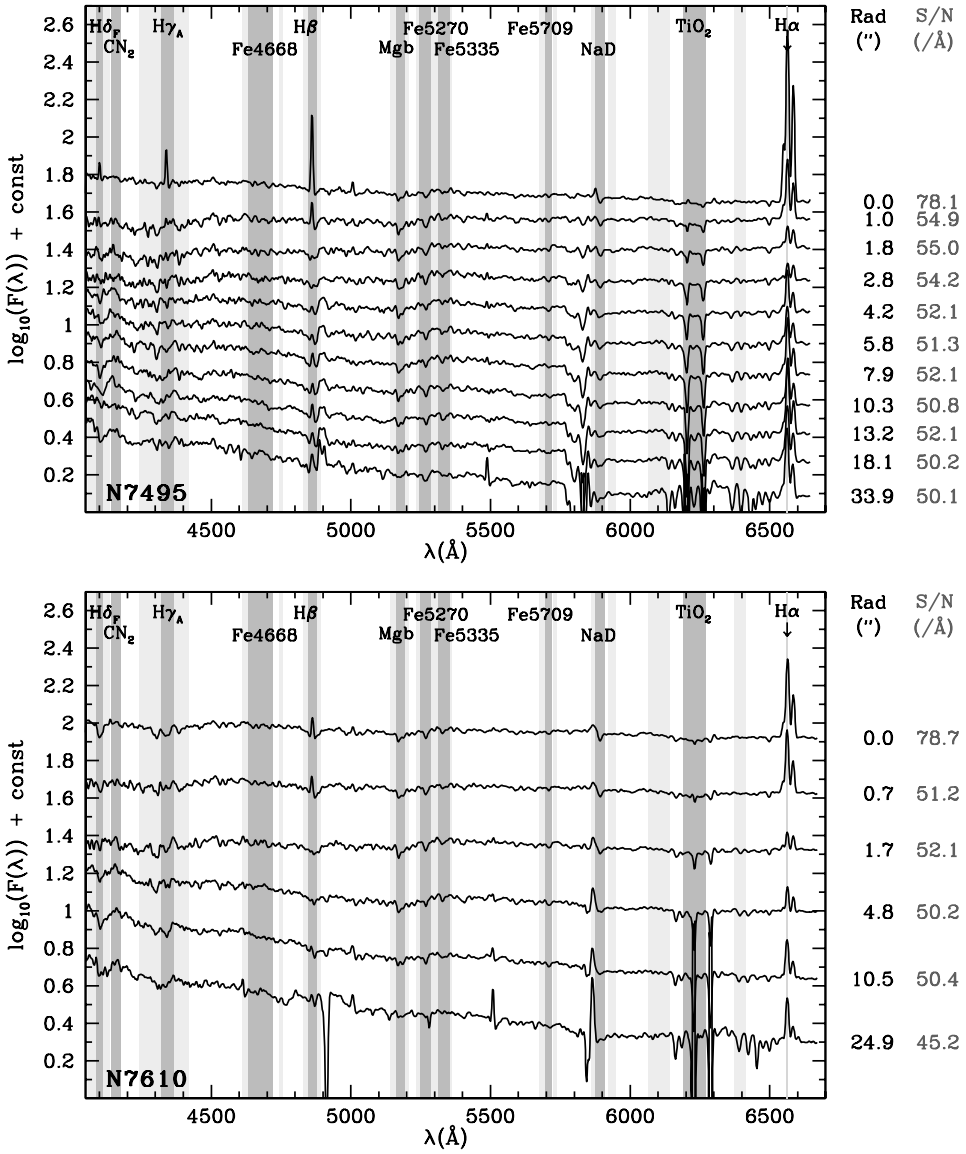

Figure A1 – *continued*

degrading the models to the resolution of the observations. Alternatively, when measuring absorption-line pseudo-EWs, the indices could be corrected for resolution effects using a calibration based on a systematic broadening of templates of similar spectral type as the data (e.g. PS02). The BC03 models used for this analysis have a reported resolution $\mathrm{FWHM_{Gauss}} = 3$ Å that is constant with λ. However, as mentioned above in Section 3.4, due to an error in accounting for the relative velocities of the stars before combining them into SSPs, the effective resolution is not only a bit higher, but is best characterized by a constant FWHM with λ term plus a velocity (constant with $\Delta\lambda/\lambda$) term. The precise characterization will also be slightly different for each model SSP, depending on the relative velocity shifts and weights of the stars entering each SSP. On average, we find that the FWHM is closer to 4 Å, so it is still much smaller than the 10.8-Å resolution of our data, which is dominated by the slit width. Thus, to account for resolution effects due to the slit, we convolve all SSP models with a boxcar of width 10.8 Å.

Another broadening effect, independent of the instrumental set-up, which must be considered prior to any direct model/data comparison, is the galaxy velocity dispersion, $\sigma_{\rm vd}$, along the line of sight. Galaxy discs are dynamically cold systems, flattened and supported by rotation, and thus have small velocity dispersions (of the order of $\sim$10–20 km s^{-1}), whereas the spheroidal bulges of spiral galaxies can have significant support from random motions. PS02 measured velocity dispersions for late-type spiral bulges in the range 50–200 km s^{-1} for Hubble types Sa–Sbc. Because our galaxies are mostly of later type (Sbc–Scd, with one Sa bulge), we can expect bulge velocity dispersions closer to the small end of this range.

We have measured the velocity dispersion at each radial bin (see Section 4.4) for our sample and, in principle, a unique set of models could be created for direct comparison for each radial bin of each galaxy. However, given that we are analysing thousands of individual spectra, constructing a model for each one becomes too onerous. As an alternative solution, we have opted to degrade the

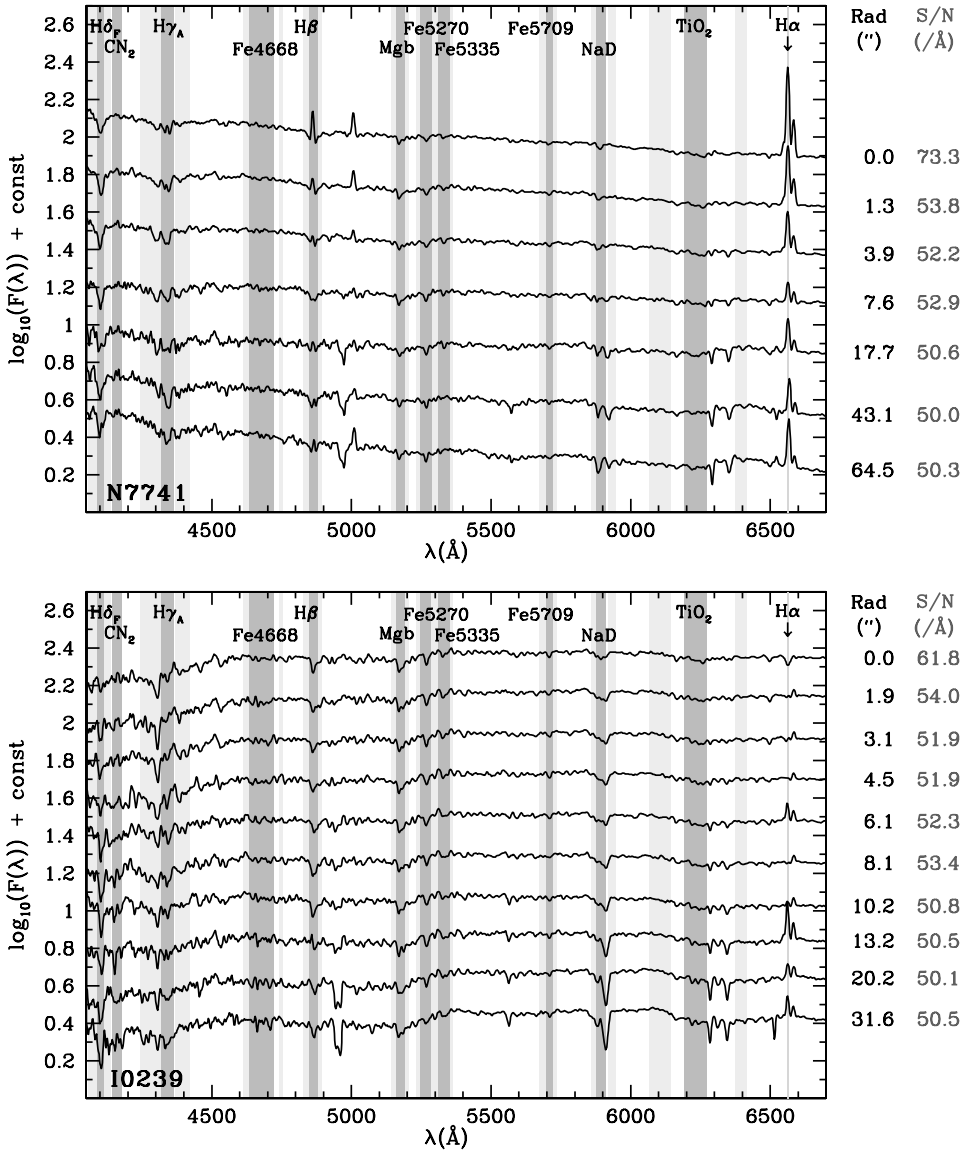

Figure A1 – *continued*

resolution of all galaxy spectra to that with the highest dispersion, so one set of models, properly convolved to this same velocity, can be used for direct comparison with the data. We thus account for resolution by putting both the data and models on the same scale by convolving all observed spectra to $\sigma = 168\,\mathrm{km\,s^{-1}}$, and all models with a boxcar of width 10.8 Å (corresponding to the slit width) and to $\sigma = 168\,\mathrm{km\,s^{-1}}$.

B2 Age and metallicity fits from Lick indices

The Lick/IDS system of spectral line indices was designed to calibrate the strength of fundamental spectral features in stars and composite systems (e.g. Gorgas et al. 1993). The indices measure the strength of a particular spectral feature (either atomic and defined as an EW in Å, or molecular and measured in magnitudes) relative to a pseudo-continuum on each side of the feature. The most reliable indices have been calibrated as a function of stellar colour (effective temperature), surface gravity and metallicity (Gorgas et al. 1993; Worthey et al. 1994) allowing for the construction of semi-empirical population models (e.g. Worthey 1994). Each Lick index is sensitive to the metallicity and age of SPs to varying degrees. When compared with population models, diagnostic plots of age versus metallicity-sensitive indices, such as Hβ versus Mg b or Fe, help break the age–metallicity degeneracy. However, measurements of many of the Lick indices are quite sensitive to spectral resolution and, thus, to the velocity dispersion of the system (González 1993; Trager et al. 1998; PS02), and their use requires relatively high-S/N data (S/N/Å $\geq$ 50; see Cardiel et al. 1998). As mentioned above, we account for the former by convolving all data and model spectra to the same resolution before measuring the indices, and the latter by co-adding the radial spectral bins to S/N/Å $\geq$ 50. In addition, certain indices, Hβ in particular, can suffer from nebular emission contamination, even in early-type galaxies (González 1993; de Zeeuw et al. 2002; Caldwell, Rose & Concannon 2003).

To help overcome the problem of nebular emission fill-in of the Hβ feature, Worthey & Ottaviani (1997) introduced two pairs of indices that measure the higher order Balmer lines Hγ and Hδ. While their age sensitivity is not as strong as for Hβ, the higher

order Balmer lines are much less affected by emission from ionized gases (e.g. Osterbrock 1989; Osterbrock & Ferland 2006). Thus, when combined with a metallicity-sensitive index, the Worthey & Ottaviani (1997) indices provide a more reliable age estimate for star-forming galaxies.

Finally, another more subtle issue is the sensitivity of many of the indices to non-solar (neighbourhood) abundance ratios (e.g. TMB03). The BC03 models used here do not account for variations in [α/Fe] which are expected for SFHs with different time-scales. Higher [α/Fe] is associated with very short SF time-scales as there is not enough time for the Fe produced in type Ia supernovae to enrich the star-forming gas that is heavy with α elements produced in the short-lived massive stars that end their lives as type II supernovae. On the other hand, for more extended SF, there is plenty of time for Fe to enrich the gas to solar levels of [α/Fe]. We attempt to address all of these issues in the context of our spiral galaxy spectra in the following.

In all, there are currently 25 Lick/IDS indices defined and calibrated. [7] Our spectra cover 24 of the indices (missing only the bluest high-order Balmer $H\delta_A$ index). We measure all 24 and use various combinations thereof in an attempt to assign reliable light-weighted age and metallicities to each spectrum.

The obvious advantage of using the Lick/IDS-index system is that the narrow wavelength span of each index measurement renders them less sensitive to low-frequency effects such as overall flux calibration errors and dust reddening (see MacArthur 2005). One major drawback when considering galaxies with current or recent SF is that the system was inherently designed to study the old SPs associated with elliptical galaxies and globular clusters.

The age and metallicity fits based on Lick indices use same maximum likelihood approach as in MacArthur (2005), but here the method has been extended to include more than just two indices. So, in the figure of merit (equation A5 in MacArthur 2005), N is now an arbitrary number of indices (at least two and up to the 24 we measure here).

While the errors on the measured indices are independent, the model tracks are not orthogonal. This produces non-orthogonal errors in age and metallicity, which can lead to spurious correlations if not understood. Additionally, the degree of non-orthogonality of the age and metallicity tracks changes with position on the grid. For this reason we have used MC methods to model the 'effective ranges' of the fitted ages and metallicities, taking into account a normal distribution about the measured errors (see MacArthur et al. 2004 for a more detailed description of this approach).

We have seen in Appendix A that many of our galaxies have significant amounts of emission, most likely coming from star-forming H II regions. Many authors attempt to correct for emission by fitting emission-free templates to their galaxy spectra. The templates can either be from linear combinations of stellar templates (e.g. González 1993), or from models (such as the BC03 models used here). Neither method is ideal. The former requires a library of stellar templates, ideally taken in the same observing run with identical conditions, which match the galaxian spectra extremely well. The latter imposes a model dependence since, if a model with a given age is used to make the correction, the same model age will be returned (you get out what you put in). Additionally, a significant amount of dust in the galaxy would cause a reddening of the spectrum that must be included as another model-dependent free parameter in the template fits (for both the empirical and model methods).

In a study of 40 elliptical galaxies, González (1993) created individual templates from stellar spectra obtained with the same observational set-up for each galaxy spectrum (at each radius) for the purpose of measuring accurate velocity dispersions. These templates fit the observed spectra to within $\sim$1 per cent. Division of the galaxy spectrum by the best-fitting template enabled detection of faint levels of emission (seen predominantly in [O III] and Hβ) in over 60 per cent of his sample. From the galaxy/template spectrum, he computed pseudo-EWs for the [O III] λ 5007 and 4959 Å and Hβ emission and found them to be strongly correlated as EW(Hβ) = 0.7 EW([O III]). As such, the Hβ index in absorption could be corrected for emission line fill-in by adding the correction 0.7 EW([O III]) to the measured index. He also made a correction to the Fe5015 index as the [O III] λ5007 line lies within the limits of the central bandpass. González (1993) strongly emphasized the importance of having suitable templates for reliable measurements of both velocity dispersion and emission corrections.

The tight correlation between [O III] and Hβ emission was tested for later type bulges (S0–Sb bulges) by PS02 using a method similar to that of González (1993). While they found the same [O III]–Hβ relation for their earliest type bulges, the six late-type bulges did not follow the González (1993) correlation for ellipticals, with some bulges showing a stronger Hβ/[O III] ratio, while others showed clear [O III] emission, but none in Hβ. This is likely due in part to the stronger absorption in the younger SPs, but could also be due to template mismatch, or true physical differences in the emission line regions for these galaxies. Thus, no straightforward correction seems to apply to spiral bulges and, by extension, their discs as well.

The higher order Balmer lines are much less affected by emission line fill-in. For a broad range of physical conditions expected in galactic emission-line regions, the line-strength ratios of Hδ and Hγ relative to Hβ are 0.25 and 0.5, respectively (Osterbrock 1989), providing some relief from emission line fill-in. Indeed, in many of our galaxies, the Hβ index lies far off of the model grids (from which ages $\gg$20 Gyr would be inferred), whereas the higher order indices imply much younger ages ($\sim$5 Gyr). However, it is still possible that the higher order Balmer lines may suffer significant fill-in in strongly star-forming regions (and indeed we see this in a few of our spectra; see e.g. the central spectrum of N7495 in Fig. A1).

Given the above-mentioned issues about emission-line corrections to the measured Balmer line indices, we have instead opted for scheme whereby the emission line affected indices are systematically eliminated from the fit, and the age determinations are compared. We prefer this method as it is less model-dependent and takes full advantage of the narrow baselines of the indices, while still using information from the entire observed SED.

We also attempt to address the issue of abundance ratio variations. While predictions for the effects of enhanced [α/Fe] exist for Lick indices (e.g. Trager et al. 2000; TMB03; Thomas, Maraston & Korn 2004; Schiavon 2007), these do not yet provide high-resolution SSP spectra, thus we cannot properly account for resolution by matching the models to the data, nor can we do full spectrum fits for comparison. To date, the only models that provide high-resolution spectra for stars with non-solar abundance ratios are those of Coelho et al. (2007). Comparing the results obtained here with these new models will be the focus of an upcoming paper, but for now, we consider only the BC03 solar scaled models for all fits.

[7] For up-to-date definitions of all 25 Lick/IDS indices, see Guy Worthey's web page at http://astro.wsu.edu/worthey/html/index.table.html.

Our fitting scheme for deriving light-weighted SSP ages and metallicities from Lick indices considers five different cases as follows.

Case A: fit all well-measured indices

By 'well measured' we mean that the index (all three bands) is not severely affected by systematic problems such as the wavelength gaps between the three GMOS CCDs or strong sky lines (which are extremely difficult to subtract accurately). The indices that were systematically eliminated from all fits are highlighted in grey in the leftmost column in the deviation plots (left-hand panels in Figs B1 and B2, see below for plot description). Note that we never include the NaD index in any of the fits as this index is affected by sky lines as well as poorly understood absorption from the interstellar medium of the galaxy. The TiO indices were also excluded from all fits except for N0628 due to sky line subtraction issues.

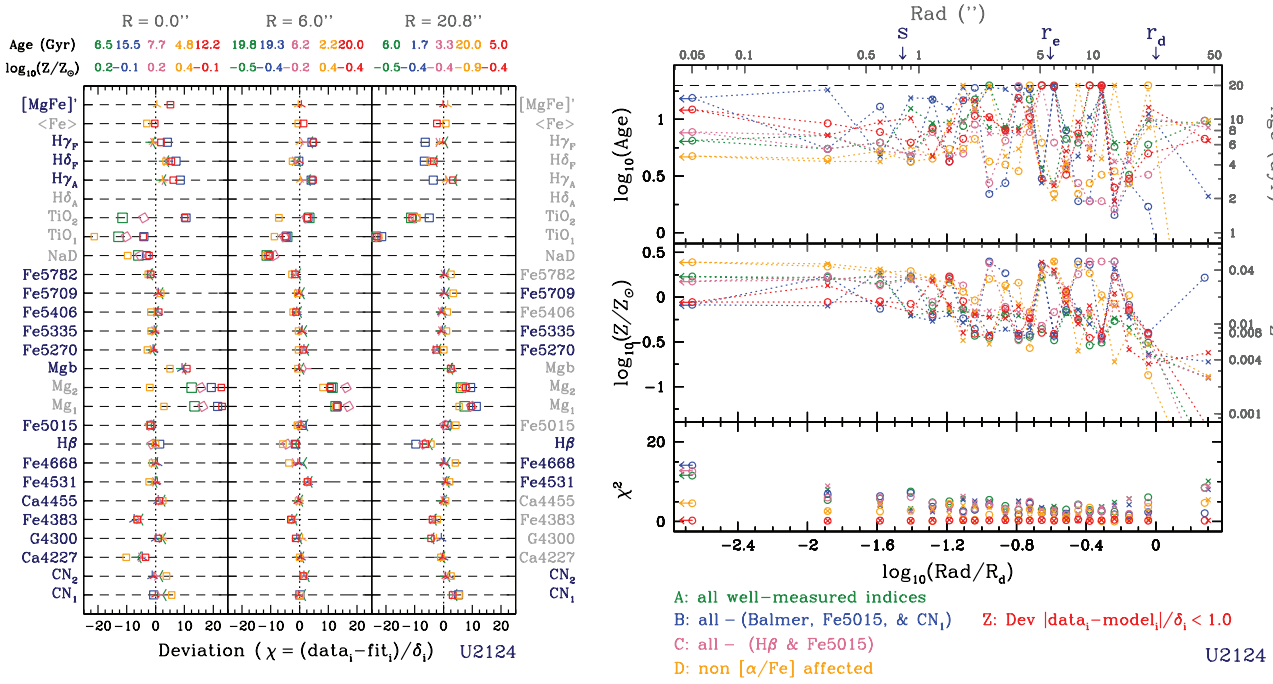

Figure B1. Results for age and metallicity fits from Lick indices for U2124. See text for plot description.

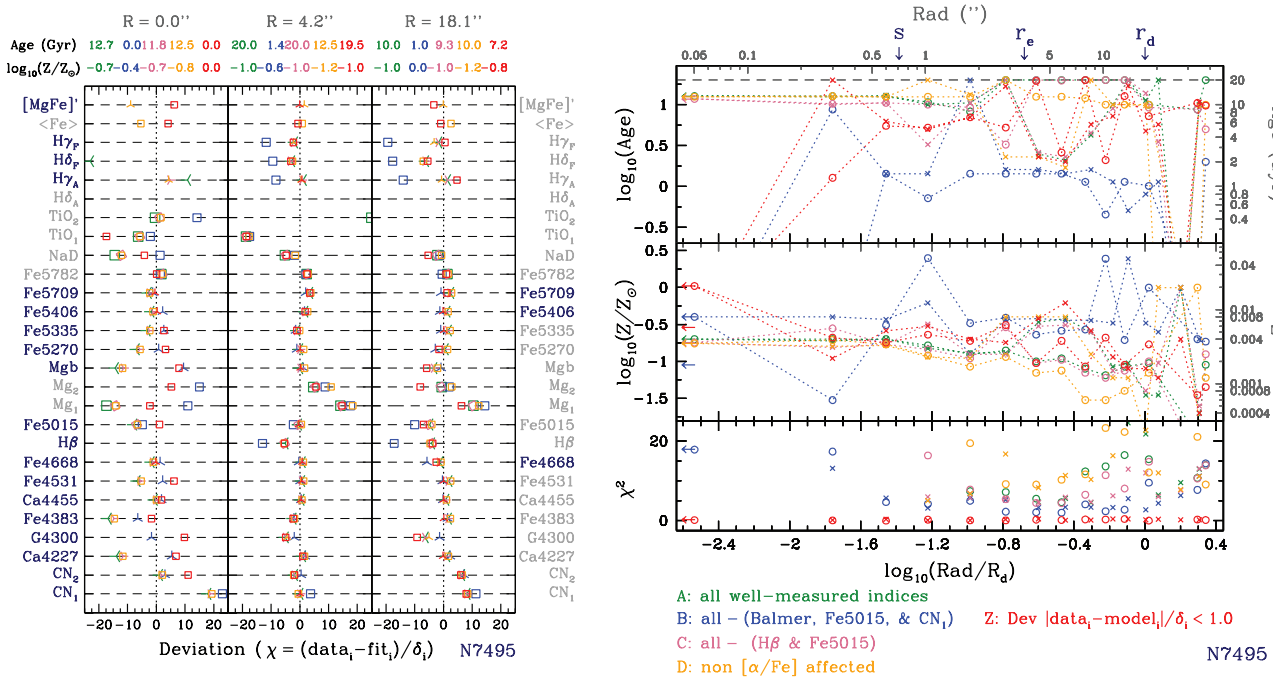

Figure B2. Same as Fig. B1 except for N7495.

Case B: Case A − (all Balmer line indices, Fe5015 and CN_1)

Here we attempt to measure ages and metallicities by eliminating all indices severely affected by emission. This is feasible because of the significant age dependence of G4300 and the weak age dependence of the metal-line indices. It is clear that all Balmer lines could suffer from emission line fill-in. The Fe5015 index has the [O III] λ5007 line in its central bandpass thus could also suffer fill-in. While seldom mentioned in the literature, we note that the CN_1 index could also be compromised by a strong source of emission since it contains the Hδ line in its blue continuum (which forces the index to larger values). This is clearly the case for at least two of our galaxies, N7495 and N7741, where Hδ is seen in emission (see their respective spectra in Fig. A1). As an example of the strong influence that emission can have on CN_1, including CN_1 in the fits, having removed all Balmer line indices and Fe5015, the age is forced to the maximum model age of 20 Gyr to accommodate the large CN_1. When CN_1 is removed, the best-fitting age drops to 1–2 Gyr. We also remark that, because of our resolution, if there is a strong emission spike in Hγ, its tails can bleed into the red passband of the G4300 index, but G4300 was not eliminated from the fits.

Case C: Case A − (Hβ and Fe5015)

Eliminate only the indices most severely affected by emission. This case should be appropriate for galaxies with only small amounts of emission, which could be undetectable in the spectra, because the higher order Balmer lines will be only weakly affected. If the age estimates here are younger than those in Case A, emission is likely present, whether or not it is clear from the spectra.

Case D: fit only $H\gamma_A$ $H\gamma_F$, [MgFe]′ and G4300

These indices are the least affected by abundance ratios (TMB03; Thomas et al. 2004). While only a few of our galaxies showed evidence for significant [α/Fe] enhancement (N0173, U2124 and N7490; see Fig. 4), many showed CN_2 values far beyond of the model grids (N0628, N7490, I0239), which this combination of indices also avoids. Such CN enhancements have been observed in globular clusters and elliptical galaxies (Henry & Worthey 1999), and are likely due to an enhancement in nitrogen (rather than carbon). However, the interpretation of carbon enhancement is challenging due to the many, and poorly understood, production sites for carbon.

Case Z: σ-clipping of high deviators

Here we initiate the fit using all 'well-measured' indices. We then follow an iterative procedure removing at each step indices that have large data–fit deviations: $|\chi_i| = |\,\mathrm{data}_i - \mathrm{fit}_i\,|/\delta_i > \chi_{\max}$, where χ_i is the relative data/model fit deviation for index i in units of the error on the measured index, δ_i. The threshold $\chi_{\max}$ is set to 3.5 initially, and reduced by 0.5 with each iteration until a minimum value of 1. Thus, all indices with $\chi_i \geq 1$ get eliminated from the fit, and $\geq$2 indices must remain for a successful fit.

Results from the age and Z fits for all five cases are displayed in Figs B1 and B2 for U2124 and N7495, respectively. In the left-hand panels of each plot, we show the deviation in units of error for each index in all four fits, quantified as $\chi_i = (\mathrm{data}_i - \mathrm{fit}_i)/\delta_i$. Each case is denoted by a different colour: Case A: green, Case B: blue, Case C: pink, Case D: orange and Case Z: red. Three-pronged point types mark the indices included in the fit for each case, while open squares mark indices omitted from the fit. Point sizes and rotations were adjusted for visibility when points are overlapping. Thus, if a given colour is not visible for a given index (except ⟨Fe⟩, which is never explicitly fit, and [MgFe]′ for which we only show Case D results), it is because the χ for that index is off scale. The dotted black vertical line mark zero deviation. The indices are labelled on the y-axis (the dashed horizontal lines are there to guide the eye to the index labels); those marked in grey are the poorly measured indices that are never included in the fits (note they are different for each galaxy). The index labels on the left-hand side indicate those excluded from all fits, while the labels on the right-hand side indicate the indices that ended up included (blue) in the Case Z fit for the $r = 0$ arcsec spectrum. For each galaxy we plot deviations at three different radii (labelled in green above each panel): the central point (left-hand panel), the point closest to the bulge r_e (middle panel), and the point closest to the disc scalelength r_d (right-hand panel). Below the radius label for each panel are the best-fitting ages and metallicities for each case in their associated colours.

The right-hand panels in Figs B1 and B2 show the age gradients in log (top panel), metallicity gradients in log (middle panel) and the χ^2 figure of merit (bottom panel), as a function of the logarithmic radius scaled to the disc scalelength (with labels in arcsec on the top panel) for all five fit cases (the colour scheme is the same as in the deviation plots and is labelled at the bottom of each plot). The data points for each fit are connected by dotted lines to guide the eye. Labels on the right-hand axes show the linear values. For each galaxy, the seeing FWHMs, the bulge r_e and the disc r_d are indicated with arrows at the top. The dashed lines in the age and metallicity plots denote the model limits, so fits with these values should be treated with caution (recall that we do not extrapolate beyond the model grids).

Examining the fits for the different cases in Figs B1 and B2 we see that the different cases can yield very different best-fitting parameters. The reason for this in some cases is clear, for example, when there is significant emission and the fits are different depending on which of the Balmer lines (if any) are included in the fit (see e.g. N7495 fits in Fig. B2). From the deviation plots we also see that, in general, the indices affected by prominent sky lines are poorly fitted; they were excluded from the fits, but the deviation parameter was still computed. For the galaxies with very high central CN indices (e.g. central region of N7490), those indices were poorly fitted in all cases.

While no single case seems to be ideal for all situations, we take the Case Z fits as our best age and metallicity estimates based on Lick indices as, in most cases, these appear to be the most stable and are the most desirable in terms of excluding highly deviant indices from the fits. Still, deriving SP parameters from Lick indices for star-forming galaxies is clearly not a secure method. With our radially resolved spectra, we can look at radial trends and identify the bins that seem most deviant, but if we should consider only one bin per galaxy, we would not be able to make such judgments. Thus, let us now consider SP fits to the full spectrum in hopes of finding a more stable method for the measurement of age and metallicity in star-forming galaxies.

B3 Age and metallicity fits from full spectra single SSP fits

We now examine full spectrum fits, considering here just the best-fitting single model SSP. Again we use the BC03 models with all model and galaxy spectra convolved to the same effective resolution. While fitting the full spectrum makes use of all the information in the spectrum, there are some drawbacks as well. Most notably, the wider wavelength baseline reinforces sensitivity to dust extinction and relative fluxing errors. However, in this case we can attempt to model the dust content by incorporating a prescription for dust in the models. The fits performed here to single SSP templates are done in a very similar manner to the full spectrum fits described in Section 3, and we refer the reader to that section for full details of the dust models and the code. Here, the number of templates in

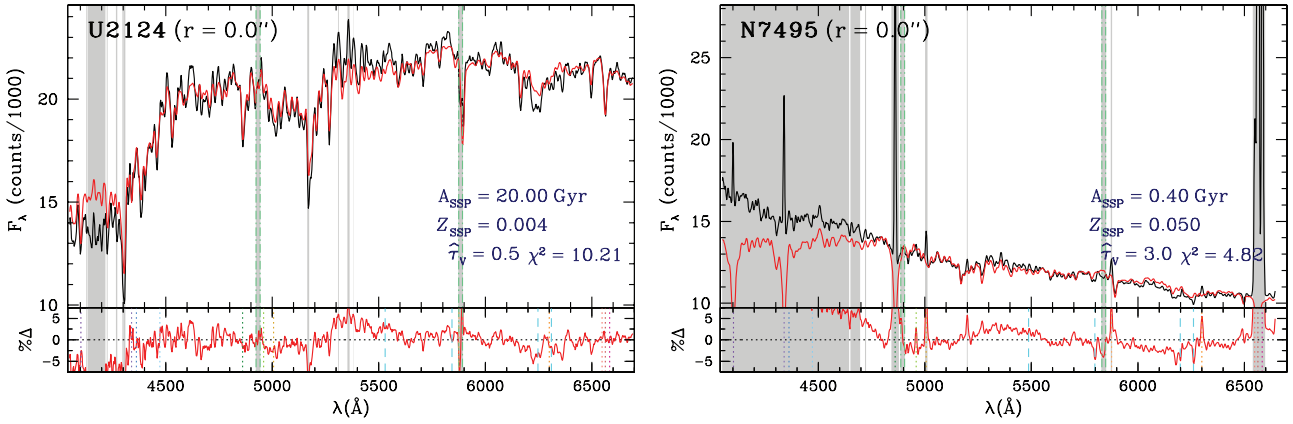

Figure B3. Examples of single SSP fits to central spectra of U2124 (left-hand panel) and the emission-line-dominant N7495 (right-hand panel). Colours, lines, shading, panels and labels are as in Fig. 3, but the ages and metallicities are now SSP-equivalent values. To be compared with full synthesis fits in Fig. 3.

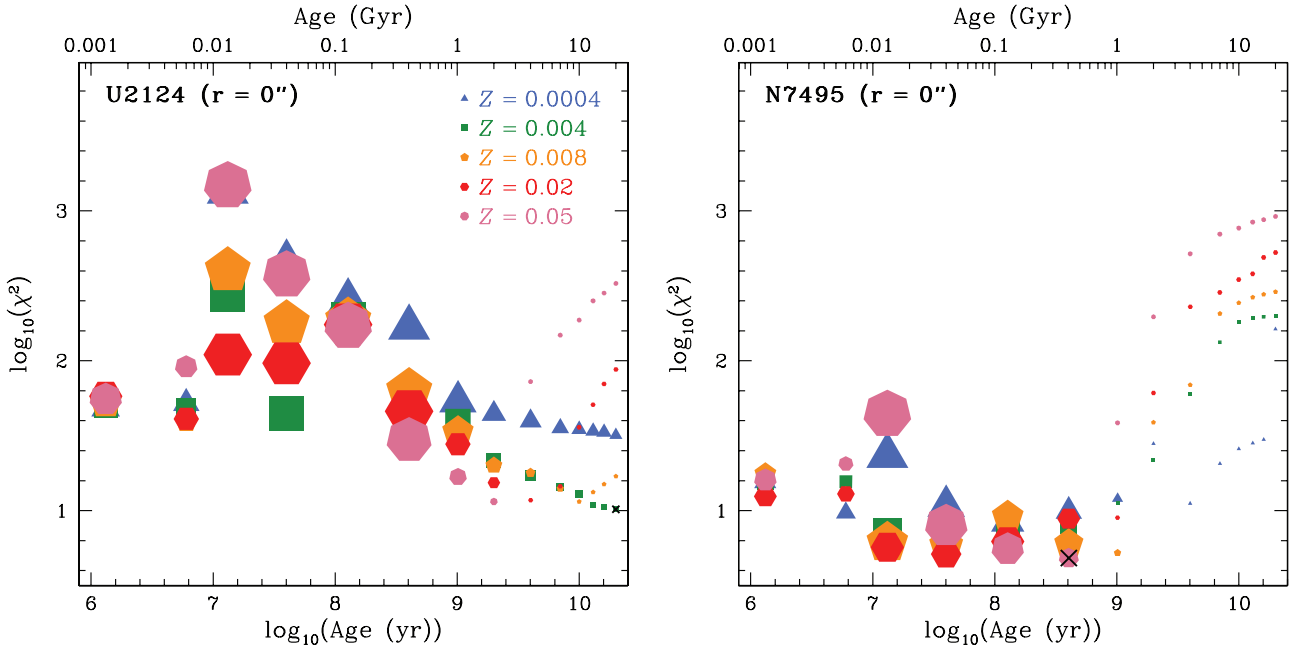

Figure B4. Examples of χ^2 distributions for single SSP fits to the central spectra of U2124 (left-hand panel) and the emission-line dominant N7495 (right-hand panel). Colours and point types indicate metallicity as labelled in the upper right-hand corner of the left-hand panel. Point size is proportional to the preferred $\hat{\tau}_V$ of the fit to a given SSP. The lowest χ^2 SSP is indicated by the black cross.

each fit is $M = 1$, and the best fit is determined by searching the χ^2 space of the fits to each of the 70 individual SSP templates shown in Fig. 2. Additionally, for each SSP template, we first compute the χ^2 of the best-fitting dust-free model. We then consider the same SSP, but with increasing amounts of dust, as described in Section 3.4.1. At each dust level (increasing by increments of $\hat{\tau}_V = 0.5$ at each step), if the χ^2 decreases from the previous fit, the dust content is increased and the SSP refit. This procedure is repeated until we reach a minimum in the χ^2 space and only the lowest χ^2 SSP = dust combination for each template is kept for consideration in the final χ^2 grid search. We imposed a maximum dust content of $\hat{\tau}_V = 8.5$, but this limit was never formally imposed, having always reached a minimum χ^2 at a dust level lower than the limit.

In Fig. B3 we show two examples of our SSP fits to the central spectra of U2124 (left-hand panel) and N7495 (right-hand panel). The central spectrum of U2124 shows no evidence for emission when examined by eye (see Fig. A1), and the SED is generally well represented by a very old (20 Gyr) but low-metallicity ($Z = 0.004$) SSP with a small amount of dust reddening ($\hat{\tau}_V = 0.5$). The spectrum of N7495, on the other hand, shows significant emission, even in the higher order Balmer lines. While these do get masked out by our σ-clipping procedure, this spectrum is clearly not well represented by a single SSP. The entire spectrum blueward of ~4700 Å is masked out in the fit, there being no SSP that can simultaneously match the low- and high-frequency characteristics of the spectrum.

Further insight into the single SSP fits is revealed by examination of the χ^2 distribution. In Fig. B4, we show the corresponding χ^2 distributions to the fits shown in Fig. B3. For U2124 (left-hand panel), the lowest χ^2 is at the 20 Gyr $Z = 0.004$ SSP (indicated by

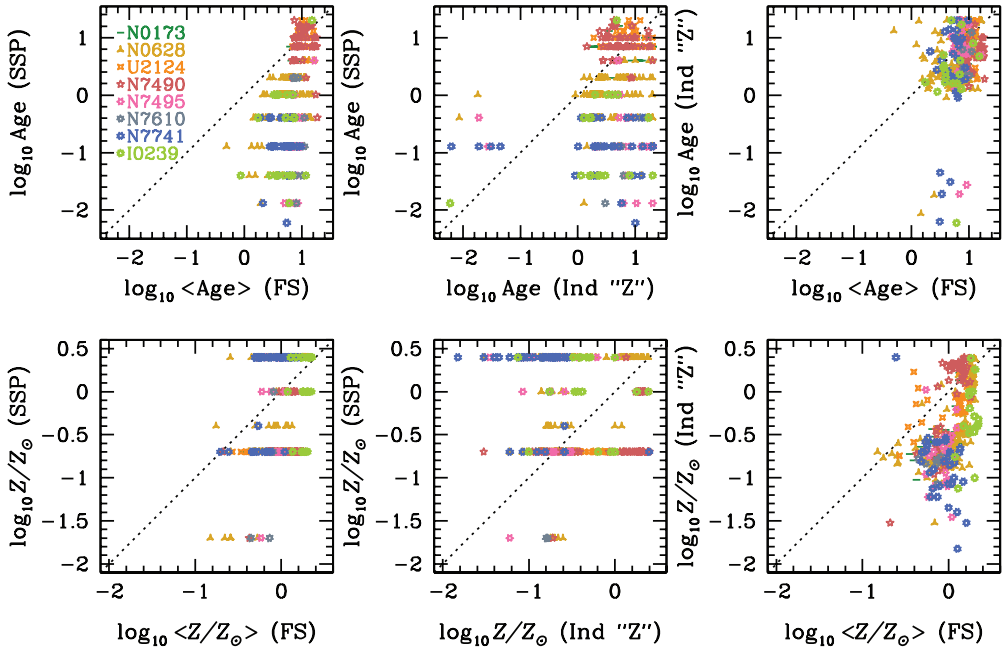

Figure C1. Comparison of light-weighted ages and metallicities derived from the three different fitting techniques: single SSP versus full synthesis (FS) (left-hand panels), single SSP versus Case Z Lick index (Ind 'Z') (middle panels) and Ind 'Z' versus FS (right-hand panels). Point types and colours are coded to a given galaxy, as labelled in the upper left-hand panel. The dotted line in each panel marks the one-to-one relation.

the black cross). However, a clear minimum in the χ^2 distribution has not actually been reached. Since 20 Gyr is the maximum age of the SSP models, we cannot say whether the χ^2 would continue to decrease for even older SSP ages. [8] It is also clear that the χ^2 for the 2 Gyr $Z = 0.05$ SSP is not all that different from the absolute minimum. This is a clear example of the age/metallicity degeneracy in SPs whereby an old/metal-poor SSP is as good a fit as a young/metal-rich SSP. Comparing the results to the full synthesis fits (Fig. 3), we see that they provide much better overall matches to the SEDs. Looking at the corresponding SFH for $r = 0$ arcsec (Fig. 7), we see that there is about an equal contribution in terms of V-band light-weight from an old/metal-poor SSP, old/metal-rich SSP and a young/metal-rich SSP, indicating that this spectrum is not well-represented by a single SSP. On the other hand, the χ^2 distribution for N7495 (Fig. B4, right-hand panel) reached a minimum within the SSP parameter space. However, the minimum is not well defined and a broad range of age/Z/$\hat{\tau}$ combinations are essentially equally well fitted. Again, from the SFH plot (Fig. 7, right-hand panels), we see that the central spectrum of N7495 has significant contributions from both very old and very young SSPs, which cannot be distinguished in a single SSP fit. Of course, there are examples of single SSP fits where a clear and unambiguous minimum in the age/Z/$\hat{\tau}$ χ^2 space exists, but these are the exception for our spectra of star-forming spiral galaxies.

APPENDIX C: COMPARISON OF DIFFERENT FITTING TECHNIQUES

It is already quite clear that the only truly representative fitting technique to derive reliable relative SP ages and metallicities for the integrated optical spectra of star-forming spiral galaxies is the full synthesis technique presented in Section 3.1. However, it is still useful to contrast the results from all three techniques to examine any clear relative trends, thus allowing the results from each method to be interpreted in the context of the other techniques. In Fig. C1 we compare the derived ages (top panels) and metallicities (bottom panels) between the single SSP versus full synthesis (FS) fits (left-hand panels), the single SSP versus Case Z (Ind 'Z') index fits (middle panels), and the Ind 'Z' versus FS fits (right-hand panels). All quantities are light-weighted, and note that we label the FS parameters as average quantities. Note also that the single SSP ages and metallicities are stochastically sampled in that they can only be exactly equal to one of the 70 SSP templates considered, whereas the fits bases on Lick indices are interpolated between the model grid space, and the FS fits are weighted averages of all SSPs contributing to the fit.

There is a reasonable correlation between the SSP and FS ages (upper left-hand panel) but the slope is far from unity (dotted line). This is expected due to the difference between SSP-equivalent ages from those derived from the average of a linear combination of SSPs. The difference and scatter become more severe the younger the age, and the SSP ages reach much younger light-weighted values than those of the FS fits. This is once again due to the fact that the youngest stars are bright and the single SSP fits are sensitive to the stars contributing most dominantly in flux to the integrated spectrum, whereas the FS fits are sensitive to any significant contribution from an underlying old population. On the other hand, there is no correlation between the SSP versus Ind 'Z' fits (top middle panel). While these two fits both provide SSP-equivalent age estimates, their primary source of age discrimination is quite different. In the full spectrum SSP fits, it comes largely from the overall shape of the SED. For the index fits it comes from the age discriminating power of the indices that do not get clipped from the fit, which may be different for each fit, and are entirely insensitive to the overall SED colour. Finally, the Ind 'Z' versus FS comparison (top right-hand

[8] Note that we are not concerned here with model ages that are older than that of the Universe. Model ages are not precisely calibrated and, as such, we are primarily concerned with relative trends.

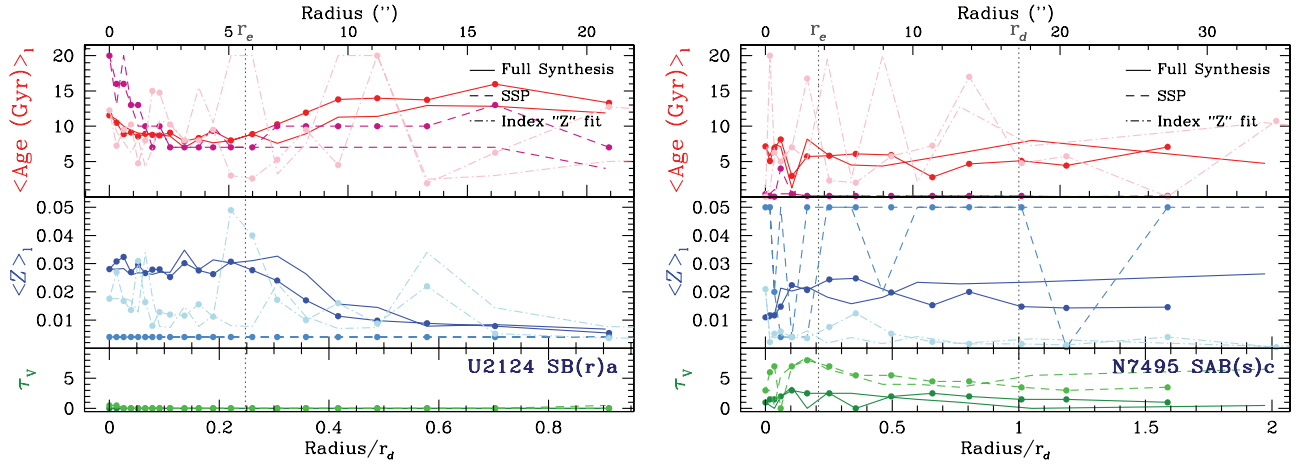

Figure C2. Comparison of the radial gradients from the three different fitting techniques. Panels and symbols are as in Fig. 8. Different line types mark results from the three fitting techniques, as indicated in the top right-hand side of each panel.

panel) shows a weak correlation with large scatter. The spread in the age predictions is similar between these two methods, indicating that neither is overly sensitive to just the most recent episode of SF, but the slope of the correlation is not unity, with the FS fits tending to older ages. As expected, in all comparisons, the best match is found for the oldest ages, corresponding to those spectra for which there is no evidence of emission lines (e.g. U2124 and N7490).

The situation for metallicity is quite similar, with a weak and less than unity correlation between the SSP and FS fits (bottom left-hand panel), essentially no correlation for the SSP and Ind 'Z' fits (bottom middle panel), and a stronger non-linear relation for the Ind 'Z' and FS fits (bottom right-hand panel), with the FS fits tending to higher metallicities.

Given the weak to null correlations between the derived SP parameters between the three methods, it is also important to investigate how the derived gradients would be affected. In Fig. C2 we show the radial variations in age and Z for the three different fits. The dash–dotted lines are for the Ind 'Z' fits and have erratic profiles that can jump drastically from one radial bin to the next. These jumps often land at the SP model extremes, indicating that they are poorly determined. The metallicity profiles seem to be much more stable that the age profiles, and as we saw in Fig. C1, they are biased to much lower values than the FS fits (solid lines). The SSP profiles (dashed lines), on the other hand, are much more stable from one radial bin to the next. For the relatively emission-line free U2124 (left-hand panel), the age profile has a similar overall form to that of the FS fits, but because they are insensitive to SPs providing small relative contributions to the SED flux, the SSP bulge looks much older than is indicated by the average age from the FS fits. Moreover, the metallicity profile is constant at a subsolar $Z = 0.004$, whereas both other fits indicate radial variation in Z, with higher metallicity towards the centre. This is another manifestation of the age/Z degeneracy, particularly in the context of SEDs that are made up of SPs of a range of ages and Z values and are thus poorly represented by a single SSP.

The emission-line-dominated N7495 (right-hand panel) shows a slightly different set of pathologies. The Ind 'Z' age profile is again erratic, jumping from very old to very young values at consecutive radial bins. The single SSP fit profile is flat, but saturated at the lowest SSP age, being only sensitive to the significant amount of current SF and blind to any underlying population. The Ind 'Z' metallicity profile again shows a similar trend as the FS fits, but at systematically lower Z. The single SSP fit profile here is erratic, jumping between high and low-Z extremes.

Finally, the radial profiles in the amount of dust extinction inferred form the FS and SSP methods is shown in the bottom panels. Both are in agreement for U2124 which is consistent with very little or no dust at all radii. The profile shapes for N7495 are similar, but the SSP derived dust levels are much higher. The higher values of $\hat{\tau}$ in the single SSP fits could in part be absorbing the redness of the underlying old SP that the single young SSP does not accommodate.

To summarize, there is no clear correlation between the three fitting techniques for any spectrum with significant contributions to the light from multiple SSPs. The SSP-equivalent parameters derived from either the index-based or single SSP fits reveal erratic behaviours in the radial profiles, which are very sensitive to different sets of characteristics of the spectrum. Only the individual fits and radial profiles from the full spectrum population synthesis fits yield representative and stable results and are suitable for assessing relative trends in age and metallicity. Therefore, the analysis and results presented in the main paper are based solely on the full spectrum synthesis fits.

This paper has been typeset from a TEX/LATEX file prepared by the author.